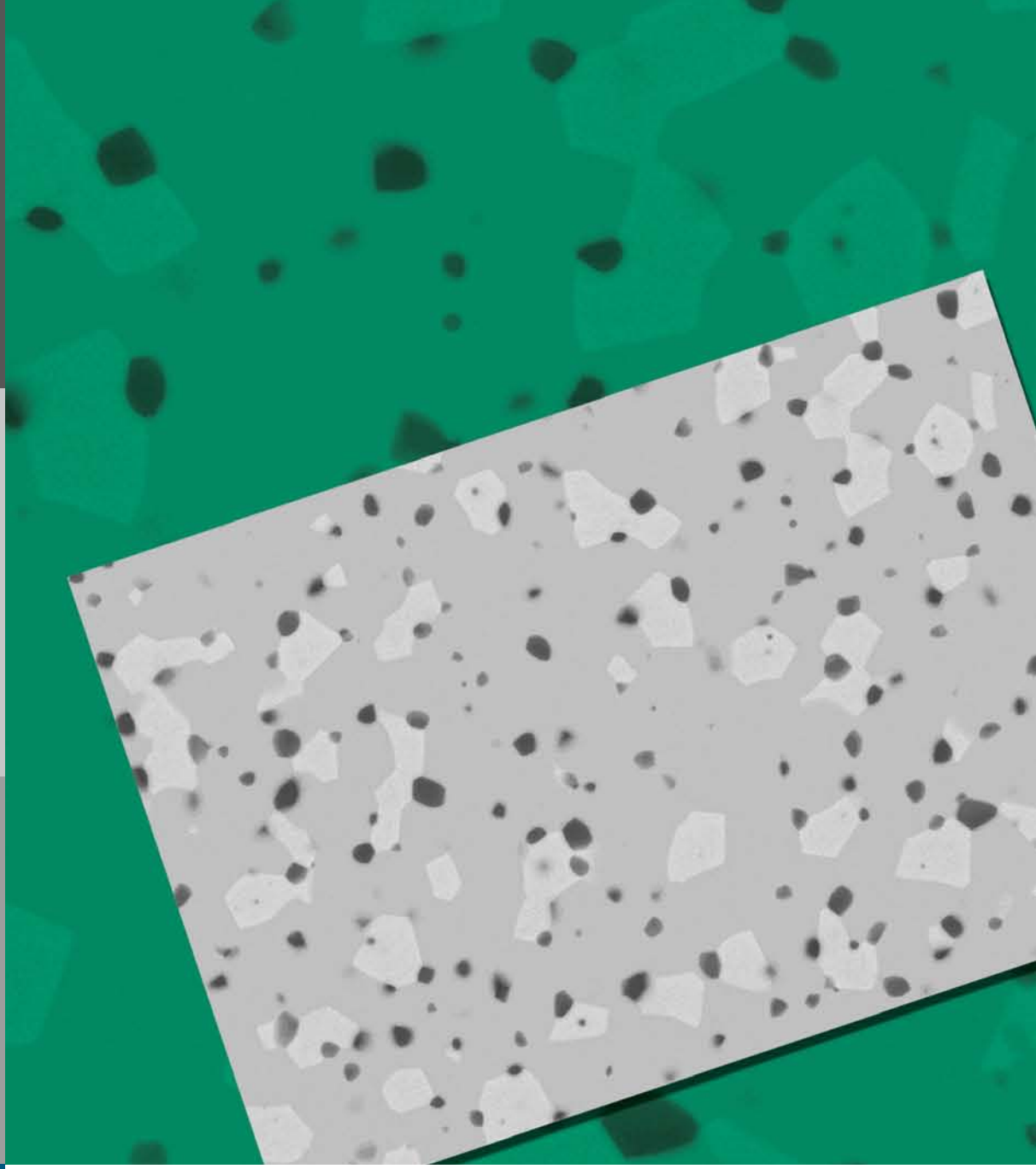

Oxides with polyatomic anions considered as new electrolyte materials for solid oxide fuel cells (SOFCs)

Oskar Hasdinor Bin Hassan

JÜLICH
FORSCHUNGSZENTRUM

Mitglied der Helmholtz-Gemeinschaft

Schriften des Forschungszentrums Jülich
Reihe Energie & Umwelt / Energy & Environment Band / Volume 68

Forschungszentrum Jülich GmbH
Institute of Energy Research (IEF)
Materials Synthesis and Processing (IEF-1)

Oxides with polyatomic anions considered as new electrolyte materials for solid oxide fuel cells (SOFCs)

Oskar Hasdinor Bin Hassan

Schriften des Forschungszentrums Jülich
Reihe Energie & Umwelt / Energy & Environment Band / Volume 68

ISSN 1866-1793 ISBN 978-3-89336-633-0

Bibliographic information published by the Deutsche Nationalbibliothek.
The Deutsche Nationalbibliothek lists this publication in the Deutsche Nationalbibliografie; detailed bibliographic data are available in the Internet at http://dnb.d-nb.de.

Publisher and Distributor:	Forschungszentrum Jülich GmbH Zentralbibliothek 52425 Jülich Phone +49 (0) 24 61 61-53 68 · Fax +49 (0) 24 61 61-61 03 e-mail: zb-publikation@fz-juelich.de Internet: http://www.fz-juelich.de/zb
Cover Design:	Grafische Medien, Forschungszentrum Jülich GmbH
Printer:	Grafische Medien, Forschungszentrum Jülich GmbH
Copyright:	Forschungszentrum Jülich 2010

Schriften des Forschungszentrums Jülich
Reihe Energie & Umwelt / Energy & Environment Band / Volume 68

D 294 (Diss., Bochum, Univ., 2010)

ISSN 1866-1793
ISBN 978-3-89336-633-0

The complete volume ist freely available on the Internet on the Jülicher Open Access Server (JUWEL) at http://www.fz-juelich.de/zb/juwel

Abstract

Materials with Polyatomic anions of $[Al_2O_7]^{-8}$, $[Ti_2O_8]^{-8}$ and $[P_2O_7]^{-4}$ were investigated with respect to their ionic conductivity properties as well as its thermal expansion properties with the aim to use them as SOFCs electrolytes. The polyatomic anion groups selected from the oxy-cuspidine family of $Gd_4Al_2O_9$ and $Gd_4Ti_2O_{10}$ as well as from pyrophosphate SnP_2O_7.

The pure oxy-cuspidine $Gd_4Al_2O_9$, the series of $Gd_4Al_{2-x}Mg_xO_{9-x/2}$ with x=0.10–1.0 and $Gd_{4-x}M_xAl_2O_{9-x/2}$ (M=Ca, Sr) with x = 0.05–0.5 were prepared successfully by the citrate complexation method. All samples showed the crystal structure of monoclinic oxy-cuspidine structure with space group of *P2₁/c* and *Z*=4. No solid solution was observed for $Gd_4Al_{2-x}Mg_xO_{9-x/2}$ where additional phases of Gd_2O_3 and MgO were presence. XRD semi-quantitative analysis together with SEM-EDX analysis revealed that Mg^{2+} was not able to substitute the Al^{3+} ions even at low Mg^{2+} concentration. The solid solution limit of $Gd_{4-x}Ca_xAl_2O_{9-x/2}$ and $Gd_{4-x}Sr_xAl_2O_{9-x/2}$ was determined between 0.05-0.10 and 0.01-0.05 mol for Ca and Sr, respectively. Beyond the substitution limit $Gd_4Al_2O_9$, $GdAlO_3$ and $SrGd_2Al_2O_7$ appeared as additional phases. The highest electrical conductivity obtained at 900 °C yielded $\sigma = 1.49 \times 10^{-4}$ Scm^{-1} for $Gd_{3.95}Ca_{0.05}Al_2O_{8.98}$. In comparison, the conductivity of pure $Gd_4Al_2O_9$ was $\sigma = 1.73 \times 10^{-5}$ Scm^{-1}. The conductivities determined were in a similar range as those of other cuspidine materials investigated previously. The thermal expansion coefficient of $Gd_4Al_2O_9$ at 1000 °C was 7.4×10^{-6} K^{-1}. The earlier reported phase transition between 1100 and 1200 °C changed with increasing substitution of Ca and Sr.

Consequently, the analogue materials of pure oxy-cuspidine $Gd_4Ti_2O_{10}$, the series of $Gd_4Ti_{2-x}Mg_xO_{10-x/2}$ with x=0.05 - 0.50 and the series $Gd_{4-x}M_xTi_2O_{10-x/2}$ (M=Ca, Sr) with x =0.05 - 0.50 were prepared successfully also by the citrate complexation method. All samples show the crystal structure of orthorhombic oxy-cuspidine structure with space group of *Pnma* and *Z*=4. No solid solution was observed for $Gd_4Ti_{2-x}Mg_xO_{10-x/2}$ where additionally phase of monoclinic Gd_2O_3 was present. The solid solution limit of $Gd_{4-x}Ca_xTi_2O_{10-x/2}$ and $Gd_{4-x}Sr_xTi_2O_{10-x/2}$ was determined between 0.20-0.30 and 0.05-0.10 mol for Ca and Sr, respectively. Beyond the substitution limit, $GdTiO_3$ and $SrTiO_3$ appeared as additional phases, respectively. The highest electrical conductivity obtained at 900 °C yielded $\sigma = 2.50 \times 10^{-4}$ Scm^{-1} for $Gd_{3.80}Ca_{0.20}Ti_2O_{9.90}$. In comparison, the conductivity of pure $Gd_4Ti_2O_{10}$ was $\sigma = 3.10 \times 10^{-5}$ Scm^{-1}. Again the conductivities determined were in a similar range as those of other cuspidine materials investigated previously. The thermal

expansion coefficient of $Gd_4Ti_2O_{10}$ at 1000 ℃ was 7.9 x 10^{-6} K^{-1}. No phase transition was observed below 1200 ℃.

The pure pyrophosphate SnP_2O_7 and $Sn_{1-x}Fe_xP_2O_{7-x/2}$ with x=0.05-0.3 were successfully synthesized via solid state reaction. XRD confirmed that main phase of SnP_2O_7 with space group of $Pa\bar{3}$ with *Z*=4 was present for all samples after calcination at 900 ℃. Additional phases of SnO_2 and $Fe(PO_4)_3$ also appeared after calcination. After sintering at 1250 ℃ for 8 h, a [3 x 3 x 3] superstructure of the SnP_2O_7 unit cell was observed as well as SnO_2 and $Fe(PO)_4$. The highest electrical conductivity obtained was 7.96 x10^{-6} Scm^{-1} at 900 ℃ for $Sn_{0.92}Fe_{0.08}P_2O_7$ which was not much different from conductivity of SnP_2O_7 with 3.78 x 10^{-6} Scm^{-1}.

In general, the ionic conductivity of $Gd_4Al_2O_9$ and $Gd_4Ti_2O_{10}$ increased about an order of magnitude due to the oxygen vacancies created by Ca and Sr cations. The electrical conductivity of SnP_2O_7 also increased by a factor of 2 of Fe cations.

Kurzfassung

Materialien mit mehratomigen Anionen $[Al_2O_7]^{8-}$, $[Ti_2O_8]^{8-}$ und $[P_2O_7]^{4-}$ wurden auf ihre ionische Leitfähigkeits- und thermischen Ausdehnungseigenschaften untersucht, um als geeignete Kandidaten für SOFC-Elektrolyte vorgeschlagen werden zu können. Im Mittelpunkt der vorliegenden Arbeit stehen die oxy-Cuspidine von $Gd_4Al_2O_9$, $Gd_4Ti_2O_{10}$ sowie der Pyrophosphat SnP_2O_7.

Die Synthese von einphasigem oxy-Cuspidin der $Gd_4Al_2O_9$, Reihe von $Gd_4Al_{2-x}Mg_xO_{9-x/2}$ mit x = 0,10 - 1,00, und der Reihe von $Gd_{4-x}M_xAl_2O_{9-x/2}$ (M = Ca, Sr) mit x = 0,05 - 0,50, erfolgte über Citrat-Komplexierung. Beide Reihen zeigen die Hauptphase der monoklinen oxy-Cuspidin-Struktur mit der Raumgruppe $P2_1/c$ und der Formeleinheit Z = 4 bzw. vier Formeleinheiten pro Elementarzelle. Keine Einphasigkeit wird bei $Gd_4Al_{2-x}Mg_xO_{9-x/2}$ beobachtet. Als weitere Phasen sind hier Gd_2O_3 und MgO präsent. Röntgenbeugungsanalyse (XRD) sowie quantitative Analyse am Rasterelektronen-mikroskop (SEM – EDX - Analyse) ergaben, dass Mg^{2+} auch bei niedriger Konzentration am Gitterplatz des Al^{3+} nicht substituiert werden kann. Außerdem konnte die Substitutionsgrenze für Ca und Sr in den Systemen $Gd_{4-x}Ca_xAl_2O_{9-x/2}$ und $Gd_{4-x}Sr_xAl_2O_{9-x/2}$ ermittelt werden (0,05-0,1 mol für Ca und 0,01-0,05 mol für Sr). Höherer Substitutionanteil führt zur Mehrphasigkeit, wobei als zusätzliche Phasen $Gd_4Al_2O_9$, $GdAlO_3$ und $SrGd_2Al_2O_7$ beobachtet werden. Die höchste elektrische Leitfähigkeit bei 900 °C ergab einen Wert von $\sigma = 1{,}49 \times 10^{-4}$ Scm^{-1} für $Gd_{3.95}Ca_{0.05}Al_2O_{8.98}$. Im Vergleich dazu liegt die Leitfähigkeit für reines $Gd_4Al_2O_9$ bei einem Wert von $\sigma = 1{,}73 \times 10^{-5}$ Scm^{-1}. Die Leitfähigkeitswerte liegen in einem ähnlichen Bereich wie auch zuvor untersuchte Materialien anderer Cuspidine. Der thermische Ausdehnungskoeffizient von $Gd_4Al_2O_9$ bei 1000 °C beträgt $7{,}4 \times 10^{-6}$ K^{-1}. Der bekannte Phasenübergang im Temperaturbereich von 1100 - 1200 °C verschiebt sich zu höheren Temperaturen mit steigendem Substitutionsanteil von Ca oder Sr.

Das oxy-Cuspidin der $Gd_4Ti_2O_{10}$, Reihe $Gd_4Ti_{2-x}Mg_xO_{10-x/2}$ mit x = 0,05 - 0,50, und die Reihe $Gd_{4-x}M_xTi_2O_{10-x/2}$ (M = Ca, Sr) mit x = 0,05, 0,10, 0,20, 0,30, 0,40 und 0,50 wurden ebenfalls erfolgreich durch die Citrat-Komplexierung synthetisiert. Alle Pulver zeigen als Hauptphase die orthorhombische oxy-Cuspidin-Struktur mit der Raumgruppe *Pnma* und Z = 4. Keine Einphasigkeit konnte bei der $Gd_4Ti_{2-x}Mg_xO_{10-x/2}$, beobachtet werden, eine zusätzliche Phase von monoklinem Gd_2O_3 war stets vorhanden. Die Substitutionsgrenze für Ca und Sr in $Gd_{4-x}Ca_xTi_2O_{10-x/2}$ und $Gd_{4-x}Sr_xTi_2O_{10-x/2}$ Reihe, liegt für Ca zwischen 0.20-0.30 und für Sr zwischen 0.05-0.10. Höherer Substitutionsanteil führt zur Bildung zusätzlicher Phasen ($GdTiO_3$ und $SrTiO_3$). Die höchste elektrische Leitfähigkeit bei 900 °C ergab den Wert $\sigma = 2{,}50 \times 10^{-4}$ Scm^{-1} für $Gd_{3.80}Ca_{0.20}Ti_2O_{9.90}$. Im Vergleich dazu liegt der

Leitfähigkeitswert für einphasiges $Gd_4Ti_2O_{10}$ bei σ = 3,10 x 10^{-5} Scm^{-1}. Auch hier zeigt sich, dass die Leitwerte in einem ähnlichen Bereich liegen, wie die zuvor untersuchten Cuspidin-Materialien. Der thermische Ausdehnungskoeffizient von $Gd_4Ti_2O_{10}$ bei 1000 °C beträgt 7,9 x 10^{-6} K^{-1}. Es konnte kein Phasenübergang unterhalb 1200 °C beobachtet werden.

Einphasiges Pyrophosphat von SnP_2O_7 und $Sn_{1-x}Fe_xP_2O_{7-x/2}$ mit x = 0,05 - 0,30, wurde erfolgreich über Festkörperreaktion synthetisiert. Die Röntgenbeugungsanalyse bestätigt die Hauptphase SnP_2O_7 mit der Raumgruppe $Pa\bar{3}$ und Z = 4 bei allen Proben. Die Nebenphasen SnO_2 und $Fe(PO_4)_3$ zeigen sich zusätzlich nach dem Kalzinieren bei 900 °C. Nach dem Sintern bei 1250 °C für 8 h konnte die Überstruktur von SnP_2O_7 [(3 x 3 x 3 Elementarzellen)] beobachtet werden, sowie SnO_2 und von $Fe(PO)_4$. Für die Verbindung $Sn_{0.92}Fe_{0.08}P_2O_7$ liegt die beobachtete elektrische Leitfähigkeit bei 900 °C bei einem Wert von σ = 7,96 x10^{-6} Scm^{-1}. Diese unterscheidet sich von der Leitfähigkeit von SnP_2O_7 mit σ = 3,78 x 10^{-6} Scm^{-1} nur gering.

Im Allgemeinen stieg die ionische Leitfähigkeit von $Gd_4Al_2O_9$ und $Gd_4Ti_2O_{10}$ um etwa eine Größenordnung. Dies hat seine Ursache in den Sauerstoff-Fehlstellen, die durch Ca und Sr-Kationen erzeugt wurden. Die ionische Leitfähigkeit von SnP_2O_7 stieg ebenfalls um den Faktor 2 bei Anwesenheit von Fe-Kationen.

1 Summary and aim of the work

As we know, electrical energy did not come in a direct way, but it is always a conversion of other energy sources from one type to the other. These energy sources are known as renewable and non renewable sources [1]. Part of the conversion processes was identified as the source for the global warming problem [2-4]. A fossil fuel power plant is one of the examples where CO_2 and other gases are produced which contaminate the environment and create global warming in general [5, 6]. A nuclear power plant that produced electrical power with good efficiency, however results in an end problem of radioactive waste. This non-convertible waste will be a big problem for future generations [7].

The challenge to meet the needs of electrical energy by reducing the use of fossil fuel power plants and nuclear power plants, is paramount. The so-called alternative energy such as wind power, wave power, solar, bio-mass, fuel cells and many more are being optimized to cater the needs of electrical energies [8]. Some of these ways of producing alternative energy are already in operation and some still at the research level. One of it is fuel cells technology. The fuel cells technology is a promising technology since the efficiency of electrical power produced by it is so remarkable in terms of portability (mobile) and stationary. Several types of fuel cells have been introduced and investigated by various groups in the world where everyone has the same challenge which is to save the world for the future [1].

The fuel cells technology is based on electrochemical reactions and the final product is electrical energy. No moving parts is associated in the production of electrical energy. The details of various fuel cells technology is explained in the next section. In this work, the motivations of the research are focused on Solid Oxide Fuel Cells (SOFCs), which are known as an excellent stationary power generator. However, there are so many drawbacks for this technology to be commercialized since the manufacturing cost is still expansive. The key reactions in obtaining the electrical energy is from electrolyte materials. Normally this material is an oxygen ion conductor that can only conduct electricity efficiently at high temperatures such as between 600 to 900 ℃ [1].

The effort on researching new electrolyte materials for these applications is marvelous. From the modifications of available materials (optimizing ionic conductivity) until the suggestion of totally new family of materials, shows incredible dedications involving some

groups of people all over the globe working around the clock to answer this challenge. It is really motivating to join these people in contributing to this filed. In this work several oxides of polyatomic anions such as oxy-cuspidine $Gd_4Al_2O_9$, oxy-cuspidine $Gd_4Ti_2O_{10}$ [9] and pyrophosphate SnP_2O_7 [10] were suggested. These polyatomic anions were modified in such a way to induce oxygen vacancies that will allow the oxygen ions mobility in the parent structure. For the oxy-cuspidines, the divalent cations of Mg, Ca and Sr were used for that purpose. While for the pyrophosphate, Fe^{3+} is the candidate. Series of samples were synthesized via citrate complexation method where the solid solubility limits of substitution cations were determined. The ionic and electrical conductivity were evaluated together with thermal expansion behavior that could match the available electrolyte materials such as 8YSZ materials [1, 11] to be candidates as an electrolyte of SOFCs.

Therefore the specific aims of this work are to obtain an applicable electrical conductivity of $Gd_4Al_2O_9$, $Gd_4Ti_2O_{10}$ and SnP_2O_7 via the modification methods as mentioned above. The expected electrical conductivity of those materials is in the range of 10^{-3} to 10^{-2} Scm^{-1} at 600 or 700 °C. Together with those investigations, the thermal expansion coefficient also aims to be in good match with available electrode materials which should be in the range of 10 to 12 x 10^{-6} K^{-1} also at the same temperature.

2 Introduction

2.1 Fuel cells

Fuel Cells are known as an excellent efficient electrochemical device for direct conversion of chemical energy into electrical power. The idea of fuel cells was coined by the principle of galvanic gas batteries and was originally demonstrated by Sir W. R. Grove [12], who produced electricity by “cold combustion” of hydrogen with oxygen. The ionic conductivity of stabilized zirconia was later discovered by Nernst [13], which enabled the demonstration of the first fuel cell concept based on zirconium oxide by Baur and Preis [14]. Different types of fuel cells were developed that follow the same basic principle and share similar generic components. Fuel cells are composed of an oxygen electrode (cathode), an ionic conducting electrolyte and a fuel gas electrode (anode). Either on the cathode or on the anode side, gas is transported to the electrolyte were it is adsorbed, dissociated and ionized. The driving force for ionic diffusion across the electrolyte is the partial pressure difference between cathodic and anodic atmospheres. On the other side, gases adsorbed on the electrolyte react with conducted ions to form waste gases. A difference of potential between cathode and anode results from electrochemical reactions and an electrical current can be collected in an external circuit. Reactions taking place in the case of Solid Oxide Fuel Cells (SOFCs) will be presented in Chapter 2.1.2.

2.1.1 Type of fuel cells

There are several types of fuel cells which are named according to the electrolyte material e.g. alkaline fuel cell (AFC), polymer electrolyte membrane fuel cell (PEMFC), phosphoric acid fuel cell (PAFC), molten carbonate fuel cell (MCFC) and solid electrolyte fuel cell (SOFC). In the following fuel cells are explained accordingly and the reactions of each fuel cell are shown in Table 1, while Fig. 1 below shows a schematic diagram of the reactants in different cells.

Table 1: Electrode reactions of fuel cells.

	Anode reaction	**Cathode reaction**
AFC	$2H_2 + 4OH^- \rightarrow 4H_2O + 4e^-$	$O_2 + 2H_2O + 4e^- \rightarrow 4OH^-$
PEMFC	$2H_2 \rightarrow 4H^+ + 4e^-$	$O_2 + 4H^+ + 4e^- \rightarrow 2H_2O$
PAFC	$2H_2 \rightarrow 4H^+ + 4e^-$	$O_2 + 4H^+ + 4e^- \rightarrow 2H_2O$
MCFC	$4H_2 + 2CO_3^{2-} \rightarrow 2H_2O + 2CO_2 + 4e^-$	$O_2 + 2CO_2 + 4e^- \rightarrow 2CO_3^{2-}$
SOFC	$2H_2 + 2O^{2-} \rightarrow 2H_2O + 4e^-$	$O_2 + 4e^- \rightarrow 2O^{2-}$

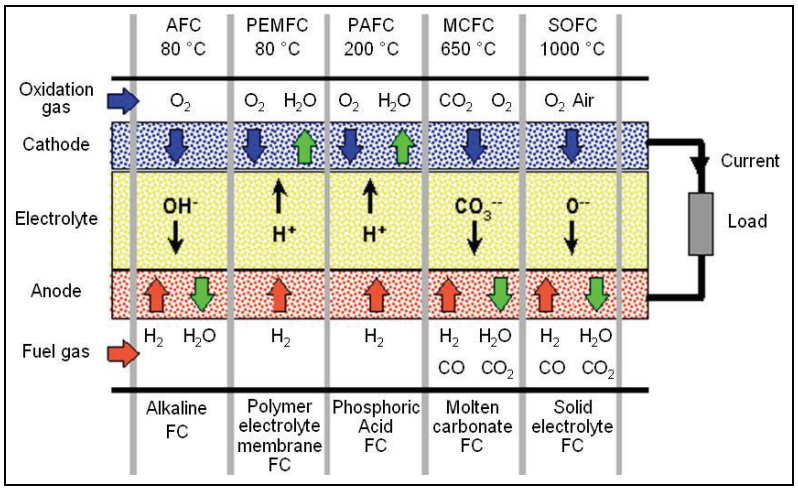

Fig. 1: Types of fuel cells and their reaction paths.

Alkaline fuel cells (AFCs)

Alkaline fuel cells (AFCs) have been used since the middle of 1960 by NASA in the Apollo and Space Shuttle programs. It was known at that time that AFCs were one of the most developed technologies. The fuel cells on board of these spacecrafts provided electrical power for on-board systems, as well as drinking water. The efficiency of the AFCs when generating the electricity is about 70 %, which make it the most efficient among other electric power producers [15]. The electrolyte in an alkaline fuel cells is an aqueous solution of potassium hydroxide (KOH) retained in a porous stabilized matrix. The concentration of KOH can be varied with the fuel cell operating temperature, which ranges from 65 to 220 °C. However, AFCs are not being considered for automobile applications. AFC is sensitive to carbon poisoning, and therefore requires the use of pure or cleaned hydrogen and oxygen that lead to an insurmountable obstacle at the present time. Conversely, AFCs operate at relatively low temperatures and are among the most efficient fuel cells, characteristics that would enable a quick starting power source and high fuel efficiency.

Polymer electrolyte membrane fuel cells (PEMFCs)

Polymer electrolyte membrane fuel cells (PEMFCs) are also known as proton-conducting polymer membrane fuel cells. The main electrolyte material that is commercially available is Nafion® which is the fibre of Polybenzimidazol. As a cell, the membrane is covered with a catalyst layer of platinum or Pt/Ru before being sandwiched with cathode and anode diffusion layers which are made of graphite. These graphite bipolar plates are then

connected with polymer or metal as interconnections to the other cells. As for basic cells operation, the oxygen or air is used as oxidants, and hydrogen or methanol as fuels. The disadvantages of these cells are the water management for the membrane during operation and the poisoning of the catalyst by carbon monoxide (CO). The efficiency of PEMFCs are about 40 to 55 % for systems in a power range of a few watts to 250 kW. PEMFCs were originally intended for aerospace applications, however it was favorable for the automotive industry and have been developed for 15 years [16].

Phosphoric acid fuel cells (PAFCs)

Phosphoric Acid Fuel Cells (PAFCs) have been developed also since the middle of the 1960s and field tested since the 1970s. They have improved significantly in stability, performance, and cost. Such characteristics have made the PAFC a good candidate for early stationary applications. The PAFC uses an electrolyte that is phosphoric acid (H_3PO_4) that can approach 100% concentration. The ionic conductivity of phosphoric acid is low at low temperatures, so PAFCs are operated at the upper end of the range of 150 to 220 °C. The PAFCs operates at more than 40% efficiency in generating electricity. When operating in cogeneration applications, the overall efficiency is approximately 85 % [17].

Molten Carbonate Fuel Cells (MCFCs)

Molten Carbonate Fuel Cells are high-temperature fuel cells that use an electrolyte composed of a molten carbonate salt mixture (Li_2CO_3, K_2CO_3 or Na_2CO_3) suspended in a porous, chemically inert ceramic matrix of beta-alumina (BASE). Cathodes are composed of Ag_2O or lithium-coated NiO, anodes of Ni or Ni with 10 wt. % Cr. Due to high operating temperatures, methane can be internally converted to hydrogen, and cells are relatively insensitive to fuel impurities. The disadvantage is a highly corrosive environment reducing the cell life. The electrical efficiency lies by 55 to 65% and systems of up to 100 MW can be built. Currently being developed for natural gas and coal-based power plants, units of 250 kW have shown overall efficiencies of up to 65%, combined to a steam turbine [18].

Solid oxide fuel cells (SOFCs)

Solid Oxide Fuel Cells rely on a dense, gas-tight oxide ceramic electrolyte, typically yttria stabilized zirconia (YSZ) that shows ionic conductivity by temperatures higher than 700 °C. The electrolyte is sandwiched between two porous, electronically conducting electrodes. The cathode is typically made of a perovskite ceramic, whereas the anode is a cermet of Ni-YSZ. High-temperature fuel cells are insensitive to CO, which make them highly fuel-flexible. Different fuel gases like hydrogen, methane and other hydrocarbons can be utilised. High electrical efficiencies of 55 to 65% are possible for systems of up to

100 MW. Combined heat and power systems (CHP) and hybrid systems with gas turbines can reach efficiencies of 70%. Research is going on towards intermediate temperatures (ITSOFC), around 600°C, in order to decrease the materials costs and increase the life time of metallic interconnectors. Another issue is to reduce the start-up time to implement SOFCs in mobile applications such as Auxiliary Power Units (APU). More detailed information on the different types of fuel cells are available in [19-21].

Operating temperature

In general the available fuel cell technology can be divided into two groups which are operating at low and high temperature. AFCs and PEMFCs are considered as low temperature fuel cells. These low temperature fuel cells are considered ideal for small-scale transport, space and military applications due to their portability and lower temperature output. These fuel cell systems are sensitive to fuel type, fuel quality and are also susceptible to electrode poisoning. Fuel processing is a problem for these fuel cells and reduces the fuel cell efficiency to 30 to 50% [22]. The PAFCs, MCFCs and SOFCs are considered as intermediate and high temperature fuel cells due to their operating temperature at range of 200 to 1000 °C. With this operating temperature, those fuel cells can be optimized for stationary power generation and can produce significant power output. The PAFCs, MCFCs and SOFCs are also commonly described as first, second and third generation of fuel cells respectively based on its research and development [22].

2.1.2 Solid Oxide Fuel Cells (SOFCs)

2.1.2.1 Comparison with conventional energy converters

In conventional thermal power engines like combustion engines and gas turbines, the chemical energy contained in fossil fuels is converted by burning in thermal energy, then in mechanical and finally in electrical energy. The efficiency factor, η, which is the ratio of generated energy to spent energy, is limited by the second principle of thermodynamics. For a system constituted of a cold source at temperature T_c and a hot source at T_h, the maximal efficiency is that of the reversible Carnot process:

$$\eta_{Carnot,rev.} = 1 - \frac{T_c}{T_h} \qquad \text{Eq. 1}$$

For a given cold source (e.g. at room temperature), the higher the combustion temperature, the higher is the reversible efficiency factor. A gas turbine working at T_h =750 °C would have a maximal efficiency of about 71%. The actual efficiency of power engines is significantly lower due to irreversible dissipation losses throughout successive energy conversion stages. Modern gas turbines of 100 MW fabricated by General Electric reached a thermal efficiency of 46%, with the possibility to obtain in a combined cycle with steam turbines overall efficiencies of 58% [23]. In fuel cells, the chemical energy of fuels (i.e. hydrogen, methane) is directly converted into electrical energy. The reversible efficiency of the fuel cell is hence defined as the ratio of the Gibbs free enthalpy $\Delta^r G$ to the reaction enthalpy $\Delta^r H$:

$$\eta_{FC,rev.} = \frac{\Delta^r G}{\Delta^r H} = \frac{(\Delta^r H - T_{FC} \cdot \Delta^r S)}{\Delta^r H} \qquad \text{Eq. 2}$$

where $\Delta^r S$ is the entropy of the reaction, and T_{FC} the operating temperature of the fuel cell. The theoretical electrical efficiency depends on the operating temperature and the fuel utilized. At an operating temperature of 800 °C, with the reaction enthalpy and entropy approximated values at standard conditions (25 °C, 1 bar), a reversible efficiency of 80% is obtained with hydrogen, whereas it reaches 99% with methane [24]. Real systems will have their efficiency reduced by ohmic losses, incomplete fuel gas utilization, gas leakages, and losses of peripherical devices. The limitations in real systems are detailed elsewhere [20, 24]. Despite the losses fuel cell systems still show high efficiencies, even as small power units and under partial load, and they are especially adapted to decentralized energy supply. Real efficiencies of different types of conventional power engines and fuel cell systems of 10 kW to 1 GW power are shown in Fig. 2.

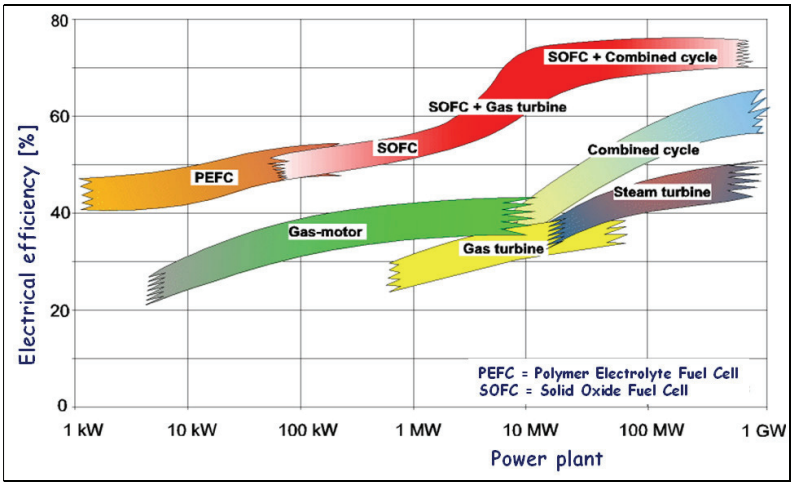

Fig. 2: Electrical efficiency (%) versus power of different power engines (Source: Siemens).

High-temperature fuel cells have a unique potential to increase the efficiency of power systems when used in combined cycles with gas of steam turbines, in large power plants. A higher efficiency by use of fossil fuels implies a lower emission of CO_2, whereas using H_2 implies no carbon dioxide emissions. However dihydrogen is until now produced from hydrocarbon sources and the production processes generate CO_2. Fuel cell systems are not competitive yet, due to high investment costs and insufficient long term stability with low degradation rates. Goal investment prices for SOFC systems are in the range of 250-500 US $/kW [25, 26]. The life time of such systems should reach 50 000 h for stationary and 5000 h for mobile applications [25].

2.1.2.2 The principal operation

Fig. 3 below shows the electrochemical reactions at the electrodes/electrolyte interfaces. At the cathode side of SOFCs three phases of materials i.e. electrolyte, cathode and air (oxygen) are in close contact and termed as three phase boundary (TPB). Similarly at the anode side the TPB consists of electrolyte/anode/fuel gas. At the TPB of electrolyte/cathode/oxygen, the O_2 is reduced to oxygen ions as shown in the reaction below,

$$O_2 + 4e^- \rightarrow 2O^{2-} \qquad \text{Eq. 3}$$

while at the TPB of electrolyte/anode/fuel gas, the fuel gas (H_2) is oxidized:

$$2H_2 + 2O^{2-} \rightarrow 2H_2O + 4e^- \qquad \text{Eq. 4}$$

The produced oxygen ions diffuse through the solid electrolyte from the cathode to the anode side. Concurrently, the electrons produced at the anode side are transported from anode terminal to cathode terminal via an outer circuit as shown in Fig. 3 below. The reduction and oxidation process taking place give an electrical power in terms of voltage and current.

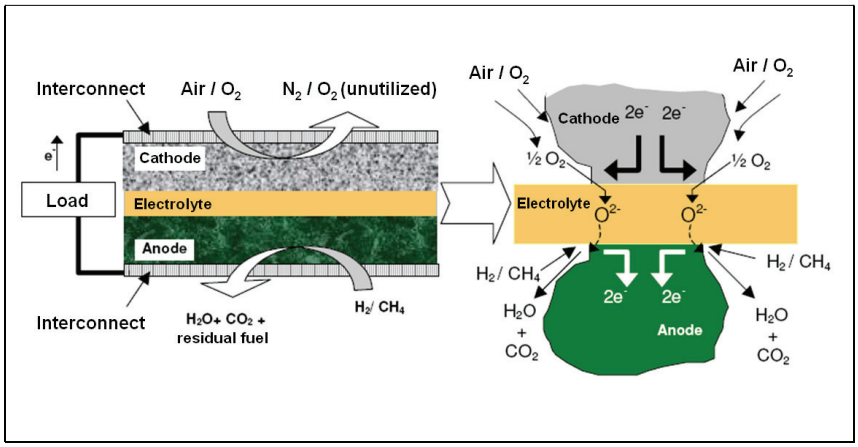

Fig. 3 : The schematic diagram of the ceramic SOFCs with reactants and products.

In a current (*I*) – voltage (*V*) diagram several mechanisms that describe the overall performance of SOFCs can be recognized. Fig. 4 shows a typical I-V diagram characteristic. Initially a significant voltage drop at low current output is observed. This is due to the over-potential which means lack of catalytic activity at both electrodes. As the current increases, a linear decrease of voltage drop is observed which is due to the ohmic losses in the cell. And another complete voltage drop observed at high current indicates an insufficient supply of fuel gas.

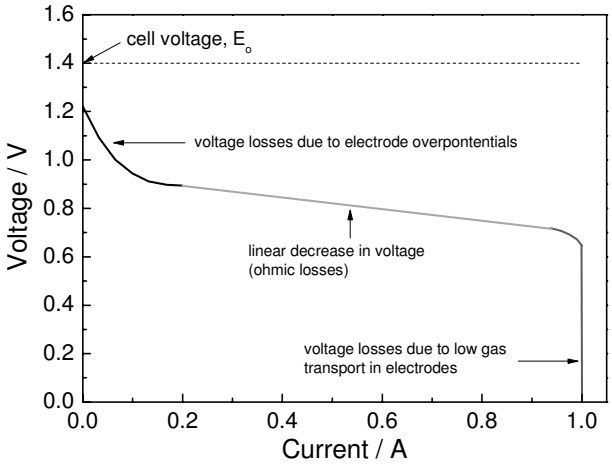

Fig. 4: Typical current (I) – voltage (V) diagram.

The cell performance can be described by the Nernst equation where the open cell voltage (OCV) E_o, can be determined,

$$E_o = \frac{RT}{zF} \ln \frac{pO_{2(cathode)}}{pO_{2(anode)}} \qquad \text{Eq. 5}$$

where R is the universal gas constant (8.314 J mol^{-1} K^{-1}), T is temperature in Kelvin, z is the number of transferred electrons (for oxygen z = 4), F is the Faraday constant, pO_2 is the oxygen partial pressure at cathode and anode. Typical values for the open cell voltage of an SOFC are in the range of 1 V. The so-called bipolar interconnect components together with gas tight electrolyte arranged in series guarantee the gas separation and yield the voltage.

2.1.2.3 Cell and stack designs

In order to obtain high voltage and high power from SOFCs, single cells are stacked together in different ways. Today the dominant stack designs are of two main types: the tubular design presented in Fig. 5, and the planar design in Fig. 7. Tubular designs may be of a large diameter (> 15 mm) or a small diameter (< 5 mm). Large diameter tubular designs were developed in the first place by the company Westinghouse [27]. The main advantage of this concept is that it does not require a high-temperature seal to separate the oxidant from the fuel. This provides a long-term reliability to the system. Drawbacks are the large current and gas path lengths through the cells, which enhance the cells

resistance and limit the power density of the system. Furthermore, the processing technology is expensive and difficult to upscale – the electrolyte layer is formed by Electrochemical Vapor Deposition (EVD). The tubular design is the most advanced technology, power plants of up to 200 kW electrical power were tested for over 20,000 h, with an electrical efficiency of about 53% [28].

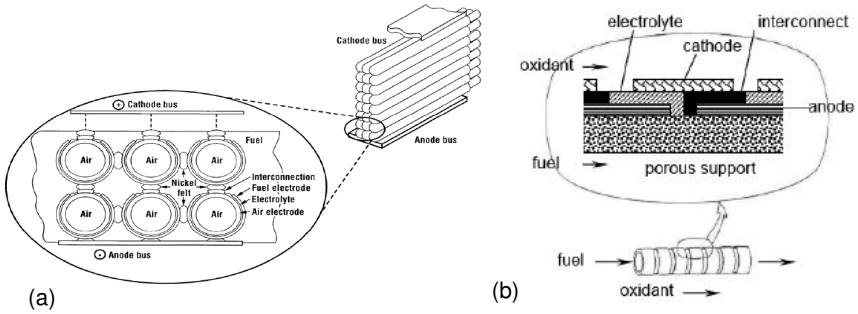

Fig. 5: (a) Tubular concept developed by Siemens Westinghouse [27], (b) Serial tubular concept by Mitsubishi Heavy Industry [29].

A variant of the technology is the “micro-tubular” design which emerged with the possibility of extruding thin-walled YSZ electrolyte tubes (diameter 1-5 mm, wall thickness 100-200 µm, [30]. The concept presents two major benefits compared to the large tubular design: first an increased volumetric power density. Power density actually increases with the reciprocal of the tubes diameter. Secondly, structures show a higher thermal shock resistance, which enable a faster start-up of the fuel cell. However systems are still not commercialized due to high resistance induced by the geometry of the cells and to the complex interconnection and stacking.

The main advantage of planar designs over other concepts is the potential to achieve higher power densities due to the short transport paths across the cell. An additional advantage lies in the more simple fabrication technology, with the possibility to use low cost processes like screen-printing or tape-casting representing a large-scale production potential [26]. The inconvenience of the design is the need of a high-temperature sealing. Furthermore, the ceramic layers show a lower tolerance to thermally induced stresses that will initiate cracking of the cells upon thermal cycling.

Planar SOFC designs can be divided into two categories: self-supported and externally supported configurations. In the self-supported configurations, one of the cell components acts as the structural support (Fig. 6). Electrolyte-supported cells offer a strong support from a dense thick electrolyte (t > 100 µm), but require a high operating temperature of about 900 to 1000 °C to minimize the ohmic losses of the electrolyte. Anode or cathode supported cells with thin electrolytes (5-20 µm) allow operating temperatures lower than 800 °C. High conducting anode cermets have been favored as substrates but have a lower stability due to potential re-oxidation [31]. Externally supported configurations include interconnected supported cells that provide a lower electrical transport limitation than anode-supported cells and stronger metallic support. However a problematic issue is the interconnected oxidation. Porous metallic substrate is an alternative to improve the support properties, given new materials are found with oxidation-resistant properties [32].

The advantages of reduced operation temperature include a wider choice of materials, especially low-cost metallic materials for interconnects, reduced thermal stresses, hence improved reliability and longer cell life, together with reduced cell costs. Main drawbacks are slower electrode reaction kinetics and reduced thermal energy extracted from hot exhaust steams of the fuel cell.

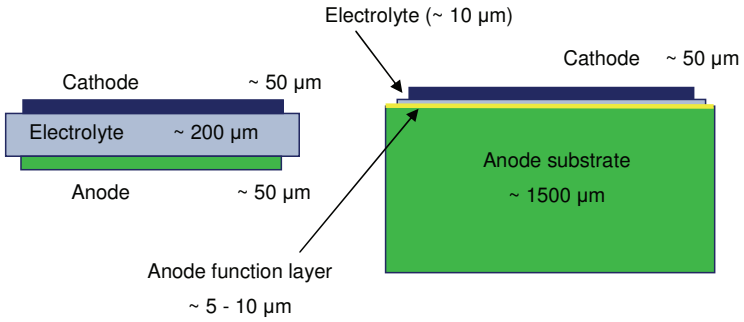

Fig. 6: Self-supported cell concept developed at Forschungszentrum Jülich: anode supported cell (right), compared to electrolyte supported cell concept (left) [33].

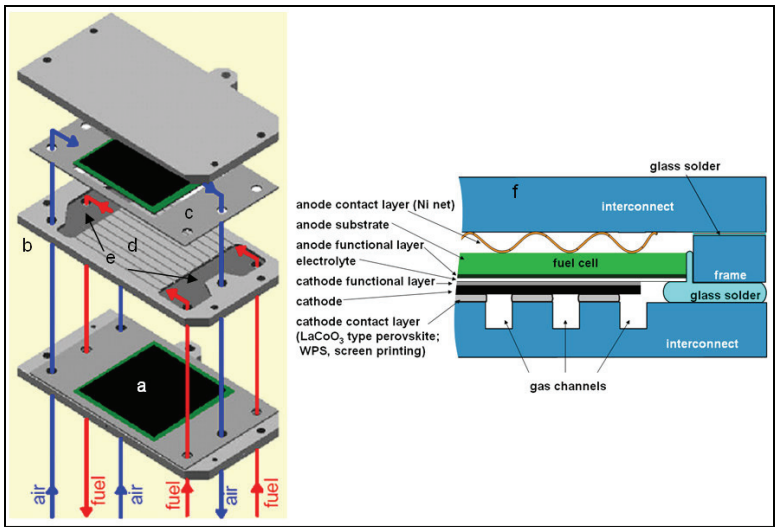

Fig. 7: Planar stack design developed at Forschungszentrum Jülich [34] where a - cell (cathode side), b - interconnect plate, c - metallic frame, d - gas distribution channels, e - internal manifolds, f - is a stack cross-section.

At Forschungszentrum Jülich, a planar anode supported cell concept was developed and integrated in different successive designs. The actual stack design for stationary applications is presented in
Fig. 7 and the cell concept is detailed in Fig. 6. The concept presents the following advantages:

- a thin electrolyte of 5 to 10 µm, which low resistance provides high power densities at low operating temperatures of 750-850 °C.
- a thick anode substrate gives the mechanical stability to the cell, it can be produced to different thicknesses by warm pressing (1.0-1.5 mm) or tape casting (0.3-1.0 mm), with dimensions of up to 250 x 250 mm^2.
- the anode functional layer and electrolyte can be coated successively by different methods including vacuum slip casting and screen-printing, and co-fired.
- low operating temperatures allow the utilization of ferritic steels as interconnected plates instead of expensive high-temperature alloys or ceramics.

2.1.2.4 SOFCs component

Anodes

In typical NiO-YSZ anodes, Ni conducts electrons, YSZ conducts ions, and pores allow gases to vent [35]. The anode reaction occurs near the three phase boundary (TPB). The effective zone around the TPB has been reported with a width smaller than 1µm on the Ni surface [36].

The main functions of the porous anode are to provide electrochemical reaction sites for oxidation of the fuel, to allow the fuel and by-products to be delivered and removed from surface sites, and to provide a path for electrons to be transported from the electrolyte/anode reaction sites to the interconnect [37]. Therefore, metal can be one component of the SOFC anode material and it must be non-oxidized at cell's fuel inlet and cell's fuel outlet. Suitable metals are limited to nickel, cobalt and noble metals, whereby nickel-YSZ cermet is the most commonly used material for SOFC. The electrical conductivity of NiO-YSZ cermet is strongly dependent on its Ni content. The conductivity of the cermet as a function of nickel content shows an S-shaped curve predicted by percolation theory [38, 39]. The conductivity of the cermet is also dependent on its microstructure.

Since Ni has a higher thermal expansion coefficient than YSZ (10.5×10^{-6} K^{-1}) of 30 volume % of Ni, there are concerns about thermal expansion mismatch between the anode and the electrolyte. A significant degree of mismatch between the thermal expansion coefficients of the SOFC components can result in large stresses, causing cracking or delamination during fabrication or operation.

Recently, ruthenium/YSZ cermets have been tested as SOFC anodes [40]. Ruthenium has the advantages of better resistance to sintering and higher reforming activity. In addition, Ru/SDC (Sm doped ceria) exhibits the lowest interfacial resistance at 800 °C compared with other metal catalysts (Pd, Pt, Rh, Pd, Ir, and Ni) in metal/SDC anodes [41]. Ru is also less susceptible to carbon deposition when hydrocarbon fuels are used. However, its high cost prevents it from replacing Ni extensively.

Some oxide materials with good mixed conductivities and catalytic properties have been used as bulk electrodes; such as bulk Ti substituted YSZ anodes [42], or mixed with metals, primarily Ni, to form cermet anodes, such as Ni-ceria [41]. Therefore, the roles of

these oxides are the promotion of anodic reaction due to ease of redox reaction and collection of current due to high electronic conductivity.

Among new anode materials and structures, there are only few reports about low temperature (<800 °C) operation. For most low temperature SOFCs, NiO-YSZ is still the most commonly used anode material. However, the information regarding the NiO-YSZ performance at low temperature is still not well developed. It is possible that NiO-YSZ anodes might limit the cell performance at low temperatures. Reducing NiO-YSZ interfacial resistances is thus important for low temperature SOFCs.

Cathode

Early stage SOFCs used tin-doped indium oxide (In_2O_3) as cathode material. This material gives excellent electrical conductivity [29]. However, In_2O_3 is the most costly and least thermodynamically stable component in the SOFC. Therefore, In_2O_3 has been replaced by other materials.

Noble metals or electronically conducting oxides have been used as cathode materials. Noble metals, such as platinum, palladium, or silver are unsuitable for practical cathode material because of prohibitive cost. Substituted oxides have been investigated [43, 44]. However, the most common disadvantages of these materials are thermal expansion mismatching, incompatibility with the electrolyte, and lack of conductivity. At present, lanthanum manganites, $LaMO_3$ (M = Co, Mn, Fe) is most commonly used.

The thermal expansion coefficient of $LaMnO_3$ is about 11.2 x 10^{-6} K^{-1} [45]. Lanthanum cobaltite ($LaCoO_3$) is another cathode material of research interest [46]. $LaCoO_3$ has higher electrical conductivity than $LaMnO_3$. $LaCoO_3$ phase is much less stable against reduction compared with $LaMnO_3$. The thermal expansion coefficient of $LaCoO_3$ is much higher than that for $LaMnO_3$ [47]. In addition to this, Strontium (Sr) is normally used to substitute La A-site to increase the conductivity. In $La_{1-x}Sr_xMnO_3$ (LSM) systems, the highest conductivity is obtained at $0.3 < x < 0.7$ [48]. However, the thermal expansion coefficient increases with increasing Sr contents. LSM cathodes with $x \approx 0.2$ to 0.3 are typical cathodes because of high electronic conductivity, good catalytic property, and appropriate thermal expansion match with YSZ. Low ionic conductivity and reactivity with YSZ at elevated temperatures are problems with LSM. Due to low ionic conductivity, YSZ is added to the cathode to form more TPB. A reaction between LSM and YSZ can form highly resistive lanthanum zirconate phases and deactivates the effective TPB [49, 50]. To

avoid this reaction, the processing temperature should be <1200 °C, or A-site deficient LSM should be used [51].

$(La,Sr)CO_3$ (LSC) and $(La,Sr)(Co,Fe)O_3$ (LSCF) are electron and oxygen ion mixed conductors. The electrode reactions can occur on the surface of these materials. In addition, these materials have high oxygen surface exchange coefficients, which reduce the over potentials for oxygen reduction [52]. However, they might react with YSZ to form phases with high resistivity ($La_2Zr_2O_7$). More than that, their thermal expansion coefficients ($\alpha_{LSC} > 20 \times 10^{-6}$ K^{-1} and $\alpha_{LSCF} \approx 15 \times 10^{-6}$ K^{-1}) [52] match poorly with YSZ ($\alpha_{YSZ} \approx 10 \times 10^{-6}$ K^{-1}). These cathode materials seem to match better with ceria-based electrolytes ($\alpha_{ceria} \approx 13 \times 10^{-6}$ K^{-1}) and they will not react with ceria. Good performance has been reported for these cathodes on doped-ceria electrolytes at low temperatures [53, 54].

Ag has also been considered as the low temperature cathodes. Ag has a high conductivity and good catalytic property for oxygen reduction. However, Ag tends to sinter even at low temperatures (~600 °C). Mixing Ag with YSZ to form Ag-YSZ cathodes thus stabilizes the Ag and also produces three-phase boundary, which lead to lower interfacial resistance. Similar results have been found with Ag-LSC [53, 55, 56].

2.2 Electrolytes

2.2.1 SOFCs electrolyte requirements

Materials that need to function as an electrolyte for the SOFC applications required a number of specific requirements that must be satisfied. The requirements for solid electrolytes for SOFC applications have been discussed elsewhere [1, 56] and briefly summarized below [57],

- It has to be a pure oxygen ion conductor. Other conduction species such as electrons or holes will reduce the oxygen ions mobility which effects the SOFC efficiency. During SOFCs operation, the low oxygen partial pressure environments (at the anode) can reduce the electrolyte materials to lower oxidation states and consequently introduce electronic conduction via mixed valence states in the electrolyte. This needs to be avoided.
- High ionic conductivity of about 0.1 Scm^{-1} at 800 °C. Minimal ohmic loss across the electrolyte is desired to improve the overall voltage output and efficiency of the cell.

- Thermal expansion compatibility between cell components is crucial for the necessary cell integrity during fabrication and operation. The missmatch of the expansion or contraction of the cell components during heating and cooling cycles leads to cell failure.
- Long-term phase stability in the electrolyte is required during SOFCs operation. This is very important in order to maintain the phase that contributes the oxygen ion thus changes in phases due to the aging process must be avoided.
- The reaction between cell components has to be minimal during SOFC operation. Unwanted side reactions can poison electrodes and electrolytes and reduce the overall performance of the cell.
- A good mechanical property of an electrolyte in term of thickness is required. Thin electrolyte material is suitable for an intermediate-temperature SOFC where ohmic resistance can be minimize, but at the same time must also be sufficiently robust to deal with shrinkage and expansion during thermal cycling. Therefore, compromise is needed in selecting materials that could have low conductivity but with practical strength and toughness, instead of materials with high conductivity but poor mechanical properties.

It is often a balance between the above requirements that determines the solid electrolyte system to be used in an SOFC. Lowering the temperature can significantly improve the thermal expansion incompatibilities, the long-term phase stability within the cell and minimize the inter-diffusion mechanisms responsible for poisoning of the various cell components. However, by lowering the operating temperature of the fuel cell, the ionic conductivity of the electrolyte is significantly decreased. Therefore, in order to compare favorably with the outputs observed at higher temperature, oxygen-ion conductors superior to currently employed compounds are required [57].

2.2.2 The conduction mechanism

The electrical and ionic conductivities for solid oxide materials are always influenced by the presence of defects in a crystal lattice. Diffusion and ionic conductivity mechanisms have been studied over many years in an attempt to understand the variables involved in defect formation and ionic motion. From Kofstad [58] work, he explained that defects occurred in crystal lattices at all temperatures above absolute zero after relating it with the thermodynamics of materials. Additionally, vacancies in the lattice can be created internally within the crystal as a function of temperature, or they can be formed as a consequence of charge compensation when aliovalent cations are substituted for normal

cation lattice sites. Furthermore, the degree of cation aliovalent substitution can influence the concentration of anion vacancies. In SOFC, the ionic conductivity of electrolyte materials is based on this type of vacancies formation. Ionic motion is the action of ion hopping, under the influence of an electric field, through the lattice via defects. The rate of ion conduction is described by [59];

$$\sigma_i = nq\mu_i \qquad \text{Eq. 6}$$

σ_i is the ionic conductivity (Sm^{-1}), n is the number of mobile ions in a given volume of lattice (m^{-3}), q is the magnitude of the electronic charge for the oxygen ion (C) and μ_i is the ions mobility ($m^2s^{-1}V^{-1}$). As described by Einstein relationship, ionic motion in the lattice can be related to the coefficient of ionic self-diffusion [59]. This coefficient can be further expanded into three-dimensions by relating it with random walk motion through the lattice and then the ions mobility can be expressed as [59];

$$\mu_i = \left[\frac{z}{6}\right]\left[\frac{q}{(kT)}\right][1-c]\gamma\lambda^2\upsilon_o \exp\left[-\frac{\Delta G_m}{(kT)}\right] \qquad \text{Eq. 7}$$

where z is the number of equivalent near neighbor sites (dimensionless), γ is a correlation factor (dimensionless), λ is the jump distance (m), υ_o is the attempt jump frequency (s^{-1}) and ΔG_m is the free energy for ion motion (eV). Based on Kilner's work [59], the correlation factor always described as the deviation from randomness of the atomic jumps, and the factor is about 0.65 in a simple cubic lattice. In a given volume of a lattice, the term c is defined as the fraction of occupied equivalent sites and therefore, the term *[1-c]* is a fraction of unoccupied equivalent sites, where N is denoted as the total number of occupied and unoccupied equivalent sites in a given volume of lattice.

When substituting Eq. 7 into Eq. 6 and rearranged n, the number of mobile ions in a given volume of lattice into the products of N and c, the ionic conductivity in a solid as a function of temperature can be expressed in the equation below [59];

$$\sigma_i T = \left[\frac{z}{6}\right]\left[\frac{q^2}{k}\right]c[1-c]N\lambda^2\gamma\upsilon_o \exp\left[\frac{\Delta S_m}{k}\right]\exp\left[-\frac{\Delta H_m}{(kT)}\right] \qquad \text{Eq. 8}$$

where ΔS_m (eVK^{-1}) and ΔH_m (eV) are the entropy and enthalpy terms for ionic motion, respectively.

At this stage, the term *[1-c]* can also be expressed with $[V_o^{\bullet\bullet}]$ which also means a vacancy in the lattice. This was developed by Kröger and Vink [60]). And usually vacancy concentration is represented in terms of molar fraction. With this notation, Eq. 8 can be expressed in the form of the Arrhenius relationship:

$$\sigma_i T = A_i \exp\left[-\frac{\Delta H_m}{(kT)}\right] \qquad \text{Eq. 9}$$

and

$$A_i = \left[\frac{z}{6}\right]\left[\frac{q^2}{k}\right]([V_o^{\bullet\bullet}]_s)(1-[V_o^{\bullet\bullet}]_s)N\lambda^2\gamma\upsilon_o \exp\left[\frac{\Delta S_m}{k}\right] \qquad \text{Eq. 10}$$

From Arrhenius relationship, it is possible to plot ln(σ*T*) vs 1/*T* and obtained straight line with a slope of $-\Delta H_m / (kT)$ by assuming that the term of $([V_o^{\bullet\bullet}]_s)(1-[V_o^{\bullet\bullet}]_s)$ is temperature independent. Then the enthalpy term is normally replaced by E_a which is a general activation energy term. Other parameters such as z, N, λ, γ and υ_o are not really influencing the ionic conductivity of one oxide to another when *q* and *k* being constants while the most influential parameters are $[V_o^{\bullet\bullet}]$ and ΔH_m [59]. However it has been observed that the $([V_o^{\bullet\bullet}])_s(1-[V_o^{\bullet\bullet}])_s$ term is temperature dependent as a consequence of induced-vacancy association [61].

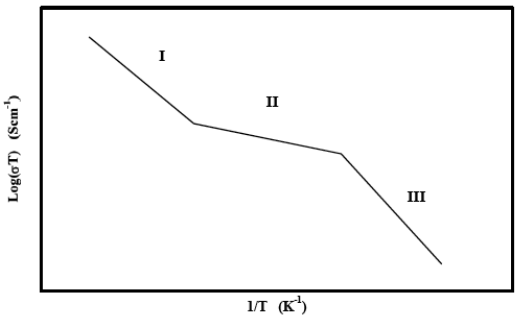

Fig. 8: A schematic representation of the conductivity behavior of an oxide or halide ionic conductors [61].

Examination of Arrhenius data for an oxide ionic conductor over a wide temperature range shows three separate regions as illustrated in Fig. 8. This illustration is base on oxides that undergo no substitution precipitation or phase changes and therefore the three regions described the mechanism of vacancies generated and interact in the ionic conductor. The slope of region I explains the existence of intrinsic vacancies in the lattice that has been generated and usually most common at high temperatures. Slope of region II explained the vacancies generated by the introduction of an aliovalent substitution and are considered extrinsic while slope of region III explains the induced-vacancy interactions that reduce the number of free vacancies at lower temperatures. Due to the already large extrinsic vacancy concentration and the high intrinsic (Schottky or Frenkel) defect formation energy found in substituted fluorite oxides, it is unlikely that region I behavior will be observed clearly in compounds with the fluorite structure [61]. However the formation of significant numbers of intrinsic defects for other structure types cannot be ruled out [57].

Oxides with ceria-based system match Arrhenius slope of region II and region III [62]. As previously mentioned, vacancies residing in region II of the Arrhenius plot are dissociated and the motion of the oxygen ions can be described by the theory linked to Eq. 6-10. However, at low temperature where region III predominates, the assumption that the free vacancy concentration is equivalent to the extrinsic substitution concentration (suggested in Eq. 8) does not hold. Kilner and Steele [63] proposed that electrostatic interaction between the charged substitution cations and oxygen-ion vacancies would make the bound vacancies energetically unfavorable for participation in the conduction process, thus reducing significantly the numbers of free vacancies available in the crystal lattice. Consequently, the concentration of free vacancies becomes dependent upon thermodynamic equilibrium between free and bound vacancies at low temperature [59, 61]. Attempts to account for the occurrence of induced-vacancy couplings have resulted in induced-vacancy association enthalpy (ΔH_a) and entropy (ΔS_a) terms being introduced to the Arrhenius relationship [59, 63]. Where significant induced-vacancy association occurs it has been shown [63] that the activation energy value derived from Arrhenius data is dependent upon migration (ΔH_m) and association (ΔH_a) enthalpy terms.

In dilute systems ($[V_o^{\bullet\bullet}]$ < 1%) it is assumed that vacancies only have one substitution cation in their nearest neighbor position and as a consequence only simple, induced-vacancy interactions are expected to dominate at low temperature [63]. The type of induced-vacancy interaction has been shown to be dependent upon the charge of the substitution [63]. Employing mass action and charge neutrality laws to the defect

association equations below (Eq. 11 and 12), and assuming that vacancies are fully associated at low temperature, Kilner and Steele [63] demonstrated the thermodynamic relationship between free defects and substituted-vacancy associates. For systems with tetravalent cations (Zr^{4+}, Ce^{4+}, Th^{4+}) it has been shown that the addition of divalent cations (Mg^{2+}, Ca^{2+}, Sr^{2+}) result in the formation of neutral substituted-vacancy associates (Eq. 11). For systems where trivalent cations are employed (Y^{3+}, Nd^{3+}, Gd^{3+}, Ho^{3+}, Yb^{3+}, Sc^{3+}, etc.) charged substituted-vacancy associates form (Eq. 12). Eq. 11 and 12 are expressed in the Kröger-Vink [60] notation:

$$Ca''_{Ce} + V_o^{\bullet\bullet} \leftrightarrow [Ca''_{Ce} - V_o^{\bullet\bullet}]^x \qquad \text{Eq. 11}$$

$$Y'_{Ce} + V_o^{\bullet\bullet} \leftrightarrow [Y'_{Ce} - V_o^{\bullet\bullet}]^\bullet \qquad \text{Eq. 12}$$

For the neutral, substituted-vacancy associates formed at low temperature the electrical conductivity, in theory, varies as a function of the square root of the substitution concentration [63]. Furthermore, the activation energy term, E_a, can be equated to the sum of the migration enthalpy (ΔH_m) and one half of the association enthalpy ($\Delta H_a/2$). For the charged associate, the electrical conductivity is theoretically independent of substitution concentration and the total activation energy is the sum of the migration and association enthalpy terms [63]. Analysis of the CeO_2-$YO_{1.5}$ system by Wang et al. [62] revealed that the predicted electrical conductivity versus activation energy and vacancy concentration trends at dilute vacancy concentrations were not experimentally observed and indicated that assumptions made during the development of induced-vacancy association theory were inaccurate [57].

However, during the development of thermodynamic expressions by Kilner and Steele [63] describing the equilibrium between free defects and induced-vacancy associates, an approximation was made where it was assumed that the concentration of induced-vacancy associates was much greater than free vacancies at low temperature. Re-examining the thermodynamic relationship between free defects and induced-vacancy associate formation, Kilner and Waters [61] attempted to explore the validity of this assumption. It was demonstrated that the transition between the induced-vacancy association range and the free vacancy range did not always occur as a sharp inflection as shown in Fig. 8. Rather the transition was often gradual and depended upon the strength of the induced-vacancy binding or association energy. Weak association between the substitution cations and the vacancies resulted in curvature of the Arrhenius data near

the transition temperature. While for strong associates, as found in the ZrO_2-CaO system, the Arrhenius data exhibited a straight line with no inflection up to 1000 °C, suggesting that association persisted to high temperature [63].

The Arrhenius relationship stated in Eq. 8 has highlighted two primary variables that may be exploited to maximize the magnitude of oxygen-ion conductivity in an electrolyte material, namely the vacancy concentration, $[V_o^{\bullet\bullet}]_s$ and the activation energy, E_a. It is apparent that the vacancy concentration and the activation energy must be maximized and minimized, respectively, in order to increase the ionic conductivity in an electrolyte. In most cases, the magnitude of the activation energy in oxygen-ion, conducting oxides is dependent upon on ion-migration enthalpy, ΔH_m at intermediate and high temperatures (where vacancies are expected to be free). The ion-migration enthalpy has been shown to vary with structure type, substituting cation size and concentration [61, 63]. In the absence of induced-vacancy association, the level of substitution controls the vacancy concentration. However in most cases induced-vacancy association cannot be neglected at intermediate temperature. Therefore systems must be chosen that possess minimal induced-vacancy association for the intended, free vacancy concentration to be as high as possible [57].

2.2.3 Investigated electrolyte materials

Fluorite structured materials - zirconia based

The most widespread electrolyte today is stabilized zirconia. It has a fluorite structure and is stabilized with yttria or scandia. Yttria stabilized zirconia shows an ionic conductivity of about 0.16 Scm^{-1} for 8YSZ at 1000 °C while scandia stabilized zirconia is about and 0.32 Scm^{-1} for 8ScSZ at 1000 °C [64]. The Y^{3+} and Sc^{3+} always substitute in the form of $Zr_{1-x}Y_xO_{2-x/2}$ and $Zr_{1-y}Sc_yO_{2-y/2}$ respectively. The best performance for value x(Y^{3+}) is 0.08-0.11 and for value y(Sc^{3+}) is 0.09-0.11 mol per formula unit, respectively. The research on zirconia based materials is still ongoing in terms of new modification with different kinds of substitutions. One of the examples is Yb^{3+} or Nb^{3+} to substitute the Zr^{4+}. However the introduced cation caused an electronic conductivity [65]. In Fig. 9a below, the total conductivity of zirconia based materials as a function of temperature is shown.

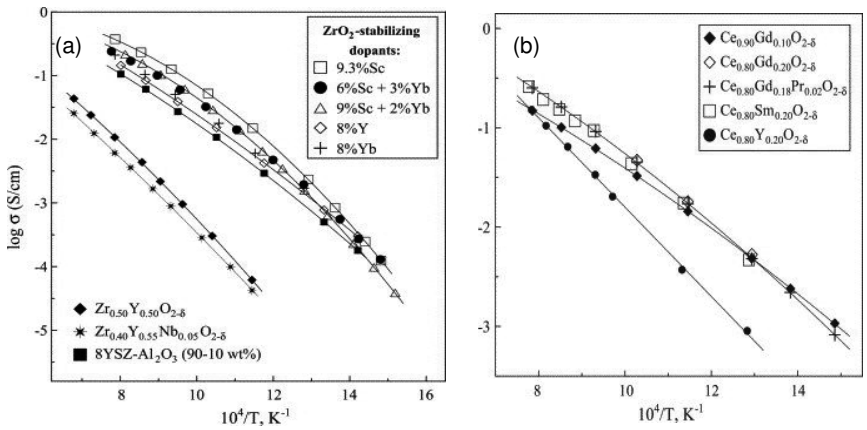

Fig. 9: Total conductivity of fluorite structured materials of (a) ZrO_2 based and (b) CeO_2 based solid electrolytes measured in air.

Fluorite structured materials - ceria based

This electrolyte is always expressed as $Ce_{1-x}M_xO_{2-\delta}$ where M = Gd and Sm. The substitution of Gd^{3+} and Sm^{3+} to ceria sites is in the range between 10 to 20% per formula unit. The often used ceria based electrolytes with Gd substitution are commonly abbreviated as CGO10 and CGO20 that refers to $Ce_{0.9}Gd_{0.10}O_{2-\delta}$ and $Ce_{0.8}Gd_{0.20}O_{2-\delta}$, respectively. The ionic conductivity obtained at 1000 °C for CGO10 and CGO20 is 0.16 and 0.24 Scm^{-1}, respectively [66, 67]. In Fig. 9b, the substitution of 2% Pr^{3+} to CGO20 did not give much change in the ionic conductivity. The substitution of 20% Sm^{3+} to the basic

compound also shows high ionic conductivity which is 0.30 Scm^{-1} at 1000 °C while 20% substitution of Y^{3+} gave lower ionic conductivity of 0.10 Scm^{-1} also at the same temperature [65].

Fluorite structured materials – bismuth oxide based

Among oxygen ion-conducting materials, oxide phases derived from Bi_2O_3 are particularly interesting due to their high ionic conductivity with respect to other solid electrolytes [65]. The fast ionic transport is characteristic of stabilized δ-Bi_2O_3, which has a fluorite-type structure with a highly deficient oxygen sublattice. Substitution with rare earth elements such as Er^{3+}, Nb^{3+} and Dy^{3+} will transform δ-Bi_2O_3 to an excellent ionic conductor. Fig. 10a shows the $Bi_{0.8}Er_{0.2}O_{1.5}$ and $Bi_{0.88}Dy_{0.08}W_{0.04}O_{1.5}$ compounds that share almost the same ionic conductivity of about 0.31 Scm^{-1} at 750 °C [68]. However the substitution or Sr^{3+}, Nb^{3+} and Ga^{3+} to the Bi sites, decreases the ionic conductivity to 0.01 Scm^{-1} also at 750 °C [69]. The other derivatives of bismuth oxide based is the introduction of vanadium to the Bi_2O_3 which lead to $Bi_4V_2O_{11}$ (parent of the so-called BIMEVOX materials), which belongs to the Aurivillius series. A stabilized γ-$Bi_4V_2O_{11}$ modified with Cu metals gave 0.18 Scm^{-1} also at 750 °C [70]. Unfortunately, Bi_2O_3-based materials possess a number of disadvantages, including thermodynamic instability in reducing atmospheres, volatilization of bismuth oxide at moderate temperatures, a high corrosion activity and low mechanical strength. Hence, the applicability of these oxides in electrochemical cells is considerably limited.

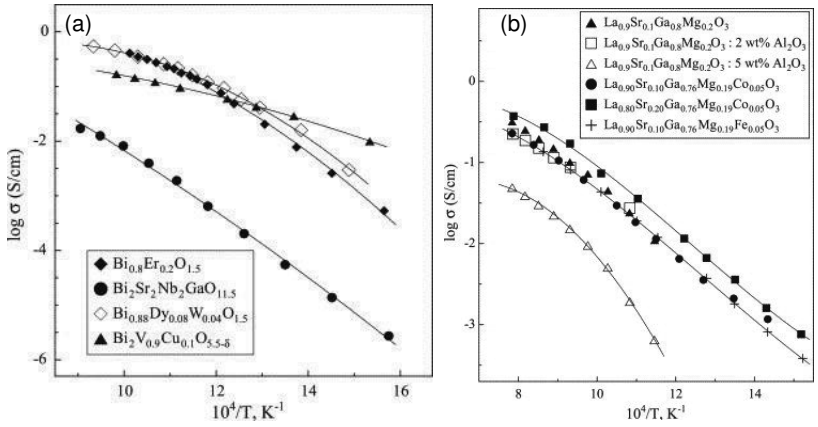

Fig. 10: Total conductivity of (a) bismuth oxide based and (b) $LaGaO_3$ based electrolytes.

$LaGaO_3$ based electrolytes

$LaGaO_3$ is a material with a perovskite structure. This electrolyte has a good ionic conductivity at lower temperature for SOFC operation. It was observed that Sr^{2+} and Mg^{2+} substitution influences the $LaGaO_3$ perovskite structures, also known as LSGM. The obtained ionic conductivity is 0.30 Scm^{-1} at 1000 °C for $La_{0.90}Sr_{0.10}Ga_{0.80}Mg_{0.20}O_3$ (Fig. 10b). When LSGM is substituted with transition metal cations such as Co and Fe, the electronic conductivity occurred. However the presence of electronic conductivity is rather small when the concentrations of the Co and Fe substitutions are limited to below 3-7%. Fig. 10b shows the conductivity value of $La_{0.9}Sr_{0.1}Ga_{0.76}Mg_{0.19}Co_{0.05}O_3$, $La_{0.80}Sr_{0.20}Ga_{0.76}Mg_{0.19}Co_{0.05}O_3$ and $La_{0.90}Sr_{0.10}Ga_{0.76}Mg_{0.19}Fe_{0.05}O_3$ are almost similar of about 0.04 Scm^{-1} at 1000 °C. It is known that the mechanical strength of LSGM based compounds is rather week. Therefore alumina has been introduced to LSGM in order to improve the mechanical strength. An amount of 2% Al_2O_3 gives good ionic conductivity to $La_{0.90}Sr_{0.10}Ga_{0.80}Mg_{0.20}O_3$, but when the amount increased to 5% Al_2O_3 the ionic conductivity dropped to 0.25 to 0.05 Scm^{-1} at 1000 °C, respectively [65].

$La_2Mo_2O_9$ (LAMOX) based electrolyte

$La_2Mo_2O_9$ is a fast oxygen ion conductor which is also known as LAMOX [71-74]. Maximum conductivity for LAMOX is shown in Fig. 11. At 750 °C, the total conductivity of LAMOX is 0.06 Scm^{-1}. The substitutions of Bi^{5+} for La^{3+} decreases the conductivity to 0.01 Scm^{-1} at 750 °C while substituting W^{6+} for Mo^{6+} gave the conductivity of 0.03 Scm^{-1} also at the same temperature. LAMOX based materials such as $La_2Mo_{1.7}W_{0.3}O_{9-\delta}$ exhibit degradation at moderate oxygen pressure (10^{-4} to 0.21 bar). The properties of LAMOX seem rather inappropriate for practical application.

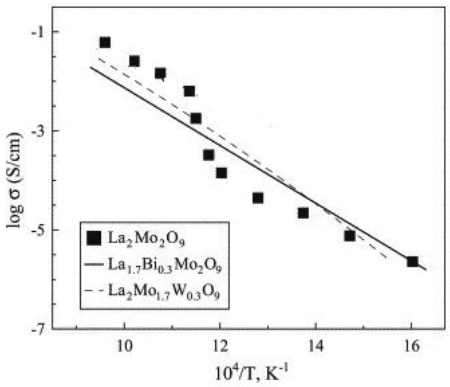

Fig. 11: Total conductivity of $La_2Mo_2O_9$ solid electrolytes in air.

Brownmillerite based electrolytes

One of the well known compounds as solid electrolyte is $Ba_2In_2O_5$ [75]. In Fig. 12, the conductivity of $Ba_2In_2O_5$ is 0.10 Scm^{-1} at 1000 °C. $Ba_2In_2O_5$ is a mixed conductor where oxygen ion transport is more dominant in air atmosphere. A drastic increase in conductivity between 850 °C to 1000 °C is observed when structure changes from brownmillerite to perovskite. Substitution of indium with higher valent cations, such as Zr, Ce, Sn or Hf, makes it possible to stabilize the disordered cubic perovskite structure and thus increase the ionic transport in the intermediate temperature range as shown in Fig. 12 [65].

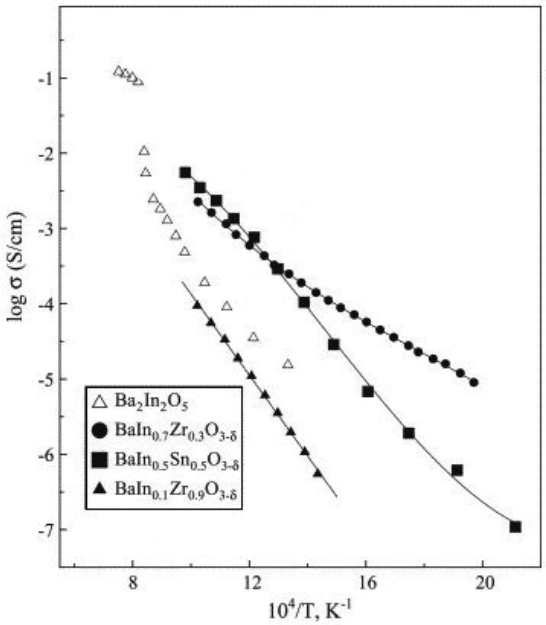

Fig. 12: Total conductivity of $Ba_2In_2O_5$ solid electrolytes in air.

Apatites based electrolyte

Investigation with apatite based materials as solid electrolyte was initiated in the 90's. The formula of apatite is $A_{10-x}(MO_4)_6O_{2\pm\delta}$ where A = rare earth and M = Si and Ge. In the apatite lattice, A-site cations presence in the cavities created by MO_4 tetrahedra with four distinct oxygen positions; additional oxygen sites (O5) form channels through the structure. Apatites with Si and Ge are commonly called germanate apatites and silicate apatites, respectively. Germanate apatites are not practical candidates as solid electrolytes in SOFC applications due to volatilization during high temperature operation,

easy to form glass phase and expensive GeO_2. Due to these shortcomings, silicate apatites are favorable over germanates apatites. Fig. 13 shows that $La_9SrGe_6O_{26.5}$, $La_{9.75}Sr_{0.25}Si_6O_{26.9}$ and $La_{9.83}Si_{4.5}Al_{1.5}O_{26}$ compounds have ionic conductivity of about 6.3 x 10^{-2} Scm^{-1} at 1000 °C, respectively. While the conductivity of $Nd_{10}Si_6O_{27}$ compound is 1.25 x 10^{-2} Scm^{-1}. The drop of this conductivity is due to differences of the ionic radius of rare earth cation as reported in [76, 77]. Fig. 13 [65].

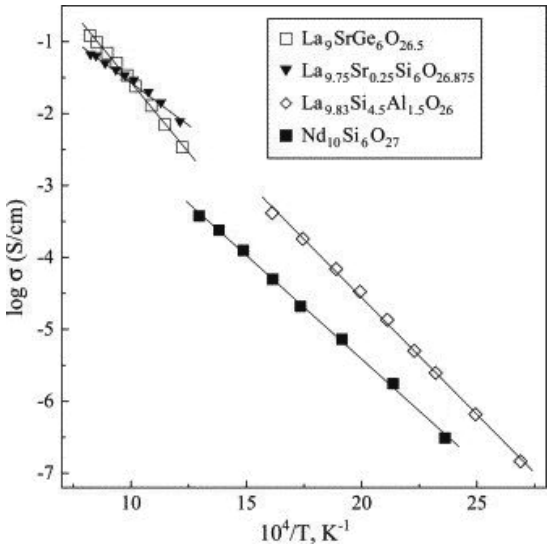

Fig. 13: Total conductivity of Apatite solid electrolytes in air.

Pyrochlores based electrolytes

Oxygen ion-conducting materials with pyrochlore structure have been studied since the 1960s. The lattice of $A_2B_2O_7$ pyrochlore can be considered as an $(A,B)O_2$ fluorite-based structure with one vacant oxygen site per formula unit in which both the cations and anion vacancies are ordered. High ionic conductivity was observed for $Gd_{2-x}Ca_xTi_2O_{7-\delta}$ series. In Fig. 14, the ionic conductivity of $Gd_{1.8}Ca_{0.2}Ti_2O_{7-\delta}$ is 6.3 x 10^{-2} Scm^{-1} at 1000 °C where it increases almost 3 orders of magnitude from pure $Gd_2Ti_2O_7$ [78]. It is also observed that the ionic conductivity of $Gd_{1.94}Ca_{0.06}Sn_2O_{7-\delta}$ increases 1 order of magnitude from pure $Gd_2Sn_2O_7$ [65].

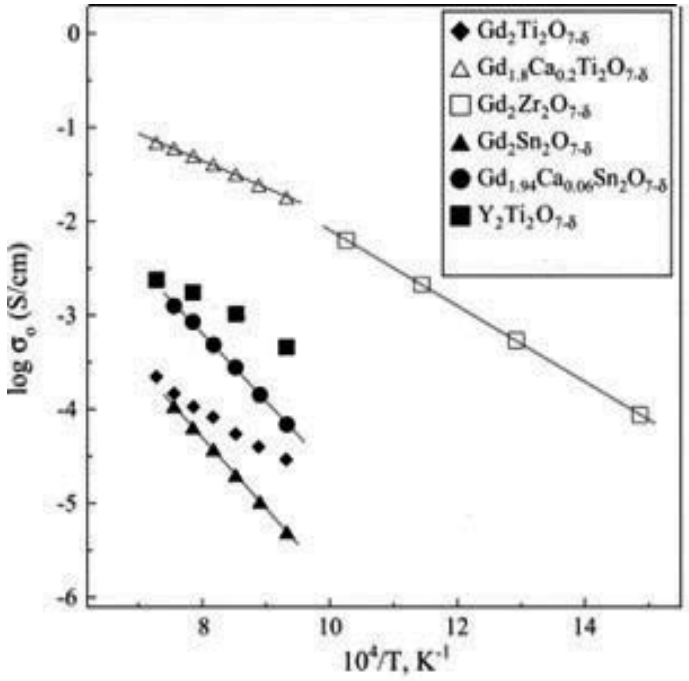

Fig. 14: Total conductivity of pyrochlore solid electrolytes as measured air [65, 78].

Thermal Expansion

Thermal expansion of a material is an important engineering property while dealing with applications involving thermal cycles. In these cycles the volumes of materials will be expanding or shrinking due to the change of lattice at crystallographic level. At crystallographic level, the atoms when exposed to heat will move to certain directions that result in change of lattice volume. These accumulated changes of lattice volume will give a significant change of dimensions in the bulk material. When this material expansion is divided by the change of temperature, then it is called the material's coefficient of thermal expansion. This thermal expansion coefficient of a standard bar, width (w) x length (l) x thickness (t) mm^3 is expressed in the equation below,

$$\alpha = \frac{\Delta l}{l_o \Delta T} \qquad \text{Eq. 13}$$

Where α is thermal expansion coefficient, Δl is the change of the length, l_o is the original length and ΔT is the temperature change.

The thermal expansion of electrolyte materials and electrode materials must be in same range to avoid mechanical stress due to mismatch of expansion. Thermal expansion coefficients (TEC) are use to express the expansion in terms of temperature intervals. TEC values of known electrolyte materials are shown in Table 2. Stabilized zirconias have TECs of about (10 -11) x 10^{-6} K^{-1} with temperatures ranging from 300-1273 K. TEC values for CGO compounds as observed at temperature range of 300-1273 K is 12.4 and 12.5 x10^{-6} K^{-1} for $Ce_{0.9}Gd_{0.1}O_{2-\delta}$ and $Ce_{0.8}Gd_{0.2}O_{2-\delta}$, respectively.

Table 2: Thermal expansion coefficients of selected solid oxide electrolytes.

Electrolyte	Composition	Temperature, *T* (K)	TEC α x 10^{-6}(K^{-1})	References
Zirconia Based	8YSZ	300–1273	10.0	[11, 79]
	10YSZ	30–1073	10.6	
	8ScSZ	300–1273	10.4	
	10ScSZ	300–1273	10.9	
Ceria Gadolinium Oxide (CGO)	$Ce_{0.9}Gd_{0.1}O_{2-\delta}$	300–1100	11.8	[66, 80]
	$Ce_{0.8}Gd_{0.2}O_{2-\delta}$	323–1273	12.5	
LSGM	$La_{0.9}Sr_{0.1}Ga_{0.8}Mg_{0.2}O_{3-\delta}$	300–1073	10.4	[81-83]
	$La_{0.9}Sr_{0.1}Ga_{0.8}Mg_{0.2}O_{3-\delta}$ (2 wt % Al_2O_3)	300-1073	10.6	
	$La_{0.8}Sr_{0.2}Ga_{0.8}Mg_{0.2}O_{3-\delta}$	300–1073	12.4	
	$La_{0.8}Sr_{0.2}Ga_{0.76}Mg_{0.19}Co_{0.05}O_{3-\delta}$	300–1473	12.7	
Bi_2O_3	$Bi_2V_{0.9}Cu_{0.1}O_{5.5-\delta}$	300–730 730–1030	15.3 18.0	[84]
	$(Bi_{0.95}Zr_{0.05})_{0.85}Y_{0.15}O_{1.5+\delta}$	320–710 710–1120	13.8 16.6	
LAMOX	$La_{1.7}Bi_{0.3}Mo_2O_9$	373–1073	16.0	[65]
	$La_2Mo_{1.7}W_{0.3}O_9$	373–623 623–1073	14.4 19.8	
Apatites	$La_{9.83}Si_{4.5}AlFe_{0.5}O_{26-\delta}$	373–1273	8.9	[85, 86]
	$La_7Sr_3Si_6O_{24}$	373–1273	8.9	
Pyrochlores	$Gd_2Ti_2O_{7\pm\delta}$	323–1273	10.8	[87]

2.3 The oxy-cuspidine and phosphate based materials

2.3.1 The oxy-cuspidines

Minerals of the cuspidine group can be described by the formula $M_4(Si_2O_7)(O,OH,F)_2$, where M stands for cations in octahedral (or roughly octahedral) coordination [88]. The structure of the prototype cuspidine $a_4(Si_2O_7)$-$(OH,F)_2$ [89], (space group (SG) $P2_1/a$ with a = 10.906 Å, b = 10.521 Å, c = 7.518 Å and β = 109.3° can be described as built up from ribbons of edge sharing $Ca(O,OH,F)_6$ octahedra running parallel to the c axis, and Si_2O_7 groups (Fig. 15).

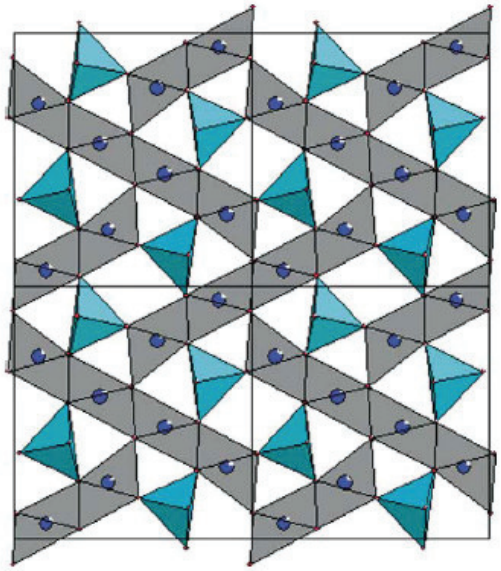

Fig. 15: [100] view of the cuspidine structure ($Ca_4Si_2O_7(OH,F)_2$).

Such ribbons are interconnected by corner sharing to create an “octahedral” framework to which Si_2O_7 groups are linked via vertices. Within the columnar arrangement of Si_2O_7 groups along the c axis, the inter-group Si–Si distance is rather short (4.3 Å), and the empty site in between can be considered as an anion vacancy. Therefore, the cuspidine structure can also be viewed as an M_4X_8 (X = O, OH, F) “octahedral” framework delimiting channels wherein $(Si–O–Si)_n$ infinite chains are running parallel to the c axis [88]. Its formula should better be written $Ca_4(Si_2O_7)(OH,F)_2$. As already indicated by Mamedov et al. [90], the cuspidine framework appears also in a group of natural and synthetic $M_4(B_2O_6)O_2$ borates [91-93], the Si_2O_7 group being replaced by two parallel BO_3 groups, leading to $(B\text{-}B)_n$ infinite chains in the channels mentioned above. Interestingly M_2TiO_5

compound (M = La [94], Y [95], Nd, Eu [96]) also contain the M_4O_8 framework of the cuspidine structure, and a more meaningful formula is therefore $M_4(Ti_2O_8)O_2$.

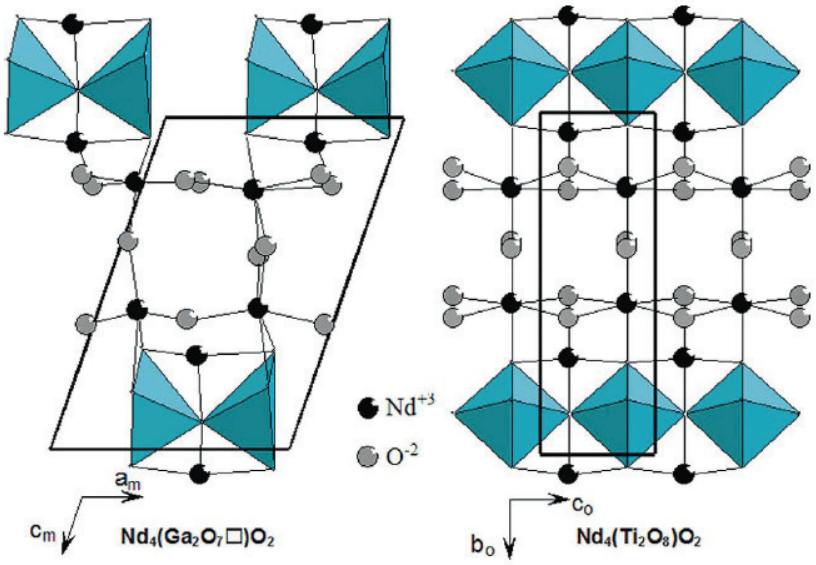

Fig. 16: Projections of the cuspidine-like structures of $Nd_4Ga_2O_9$ along *[010]* and $Nd_4Ti_2O_{10}$ along *[100]*, [97].

In this structure, the columnar arrangement of Si_2O_7 or BO_3 groups is replaced by a single chain of corner sharing TiO_5 trigonal bipyramids, leading to $(Ti–O–Ti–O)_n$ infinite chains (see Fig. 16). Together with cuspidine-like borates and silicates, this family of titanates illustrates the flexibility of the cuspidine.

Recently, $RE_4Al_2O_9$ has been modified as an ionic conductor to be a new candidate for SOFCs electrolyte. Several oxy-cuspidine materials were synthesized such as $La_4Ga_{2-x}Ti_xO_{9+x/2}$ [98], $Nd_4Ga_{2-x}Ti_xO_{9+x/2}$ [97], $La_4Ga_{2-x}Ge_xO_{9+x/2}$ [99, 100], $Nd_4Ga_{2-x}Ge_xO_{9+x/2}$ [97, 99], $(Nd,Gd)_4Al_{2-x}Ge_xO_{9+x/2}$ [9]. The total conductivity of the series is shown in Fig. 17. Pseudo-orthorhombic structures of the mentioned compounds were observed after substitution of 0.2 mol per formula unit of tetravalent cations.

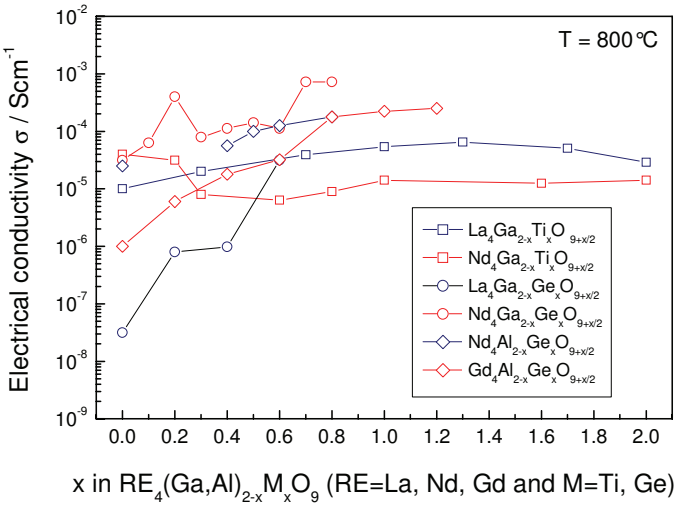

Fig. 17: Electrical conductivity of the investigated oxy-cuspidines $Ln_4(Ga,Al)_{2-x}M_xO_{9+x/2}$ [9, 97-100].

It is interesting to note that $RE_4Ga_2O_9$ is more favorable over $RE_4Al_2O_9$ to be investigated. However, Ga_2O_3 is much more expensive than Al_2O_3. Martín-Sedeño et al [9] opted to prepare $Nd_4Al_2O_9$ and $Gd_4Al_2O_9$. Several attempts to synthesize $Nd_4Al_2O_9$ did not succeed because it always decomposed to Nd_2O_3 and $NdAlO_3$. Finally, a special wet synthesis route described in [9] was able to produced single phase $Nd_4Al_2O_9$. The difficulty of synthesizing the $RE_4Al_2O_9$ in general was explained briefly by Yamane et al. [101]. From their work, $RE_4Al_2O_9$ is easy to synthesize as the ionic radius of the rare earth ions is getting smaller to the end members, which is more compatible to Al^{3+} ionic radius. Modifying $RE_4Al_2O_9$ and $RE_4Ti_2O_{10}$as ion conductor on the A site or the B site with divalent cations never has been reported previously. The closest work was for perovskite structure of $Gd_{1-x}Ca_xAlO_{3-x/2}$ and the pyrochlore structure of $Gd_{2-x}Ca_xTi_2O_{7-x/2}$ as reported in [102] and [78], respectively.

Thermal expansion of oxy-cuspidine $Gd_4Al_2O_9$ was investigated by Shimada et al. [103] and Gervais et al. [104]. They obtained TECs at 1000 °C is 8.1 and 6.5 x 10^{-6} K^{-1} respectively. Both of them also reported a reversible phase transition in the range of 900 to 1155 °C. Recently, $Gd_4Al_2O_9$ and $Gd_4Ti_2O_{10}$ were also investigated as burnable absorption in nuclear applications [105-107]. Thermal expansion was one of the key properties in that application. Chaudury et al [105] and Panneerselavam et al. [106] used

high temperature XRD for $Gd_4Al_2O_9$ and $Gd_4Ti_2O_{10}$, respectively to investigate the thermal expansion properties. The TECs value obtained from the measurements of $Gd_4Al_2O_9$ and $Gd_4Ti_2O_{10}$ is 6.91 and 9.25 x 10^{-6} K^{-1}, respectively.

2.3.2 Phosphate based electrolytes

Recently SnP_2O_7 was investigated as electrolyte materials for SOFC application by Kwon et al. [108] and Nagao et al. [109, 110]. Nagao et al. investigated the In-substitution for Sn where $Sn_{0.9}In_{0.1}P_2O_7$ shows a conductivity of 1.95 x 10^{-1} Scm^{-1} at 250 °C in un-humidified air (see Fig. 18). A power density of 264 mW/cm^2 was achieved at 250 °C when $Sn_{0.9}In_{0.1}P_2O_7$ was used as electrolyte in a fuel cell running on hydrogen. The fuel cell performance was not affected by the presence of 10% CO, even though Pt-based electrodes were used. $Sn_{0.9}In_{0.1}P_2O_7$ and materials with related compositions are thus promising electrolytes for intermediate temperature fuel cells.

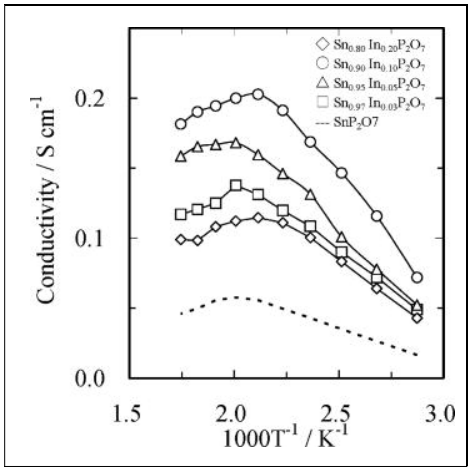

Fig. 18: Electrical conductivity of $Sn_{1-x}In_xP_2O_{7-x/2}$ (x=0-0.20 mol) in the range of 60 – 390 °C in air [109].

However, as reported by Nalini et al [111], the conductivity of similar metal pyrophosphates, such as TiP_2O_7 was 8 x 10^{-6} – 2 x 10^{-4} Scm^{-1} at 500–1000 °C in wet O_2 (pH_2O=0.027 bar) and the conductivity in dry O_2 is about an order of magnitude lower [111, 112]. The reported In-substituted SnP_2O_7 was synthesized through SnO_2, In_2O_3 and H_3PO_4 precursors (acid method) [109]. Obviously, different methods may be used for preparation of pyrophosphates which may affect the property of materials. S. Tao also investigated SnP_2O_7 and In [10], Sc [113] substituted materials as oxygen ion conductor. However the obtained conductivity is rather low for any practical application.

3 Experimental methods

3.1 Synthesis

The materials investigated in this work were synthesized via citrate complexation and solid state reaction. The oxy-cuspidine series of substituted $Gd_4Al_2O_9$ and $Gd_4Ti_2O_{10}$ were synthesized by the citrate complexation method which involved metal nitrate salts, citric acid and ethylene glycol as the starting materials. Solid state reaction was used for the synthesis of pyrophosphates of substituted SnP_2O_7 which involved the use of metal oxides and $NH_4H_2PO_4$ as the starting materials. Both methods are described below in the following section.

3.1.1 Oxy-cuspidine materials

The oxy-cuspidine series of substituted $Gd_4Al_2O_9$ was synthesized by the citrate complexation method [97, 114]. $Gd(NO_3)_3{\cdot}6H_2O$, $Al(NO_3)_3{\cdot}9H_2O$, $Mg(NO_3)_2{\cdot}6H_2O$, $Ca(NO_3)_2{\cdot}4H_2O$ and $Sr(NO_3)_2$ (all 99.99 % purity, Merck) were used as starting materials. The metal ions were complexed by adding citric acid (AR Grade, Merck) amounting to twice the molar concentration of cations used in the composition. Subsequently, ethylene glycol (AR Grade, Merck) was added in a molar ratio of citric acid and ethylene glycol which was 1:2 so that metal complexes with citric acid were interlinked. The gel obtained after dehydration of the solution was slowly dried at 300 °C overnight. The dried gel was pre-calcined at 600 °C for 0.5 h and calcined at 900 °C for 8 h.

A similar procedure was adopted for the synthesis of substituted $Gd_4Ti_2O_{10}$ series. For the Ti cation source, Ti (IV)-isopropoxide (Merck) solution was mixed with water to obtain a white precipitate which was filtered and washed several times. Finally this $TiO{\cdot}(NO_3)_2$ precipitate was dissolved in 65% HNO_3 (AR Grade, Merck) to form a clear solution.

3.1.2 Phosphate based materials

The pyrophosphate series of substituted SnP_2O_7 was synthesized via solid state reaction. The starting materials, i.e. SnO_2, Fe_2O_3 and $NH_4H_2PO_4$ (all 99.99 % purity, Merck), were mixed in stoichiometric amount followed by ball milling with Al_2O_3 balls (99.99 %) in ethanol for 48 h. The mixtures were slowly dried in air and calcined at 300 °C for 2 h. The calcined powders were grinded and milled again for 48 h. After drying, the powders were pressed to bars and sintered at 1000 and 1200 °C for 6 h.

3.2 Characterizations

3.2.1 Chemical analysis

Chemical analysis was carried out to determine the stoichiometry of the cations in the synthesized powders. The method used for this purpose is known as *Inductive Coupled Plasma-Optical Emission Spectroscopy* (ICP-OES). It is used for qualitative and quantitative determination of metals and certain non-metals in solution. The liquid sample is nebulised into a plasma where the temperature is sufficiently high to break the chemical bonds, liberate elements present and transform them into a gaseous atomic state. A number of atoms passes into excited state and emit radiation. The frequency of this radiation is characteristic of the element emitting it and thus can be used for identification purposes [115]. In the present work, the measurement was carried out by dissolving powders in either acid or base. The solution was then nebulised as described above. All the traced elements were reported with relative errors of ±3 and ±10 wt % for elements above 1 and 0.1 wt %, respectively. The measurements and facilities was provided by *Zentralabteilung für Chemische Analysen* (ZCH) of *Forschungszentrum Jülich* (FZJ), Jülich, Germany.

3.2.2 Thermal analysis (DTA/TGA)

Some of the powders were studied using thermal analysis technique such as DTA/TGA. Differential thermal analysis (DTA) provided information about the reactions or processes of the powders within a temperature range. These reactions were recorded in terms of exothermic and endothermic signal which can be interpreted as the formation of a phase, phase transition and phase decomposition. These reactions are sometimes accompanied by change in weight and can be recorded by thermo gravimetric analysis (TGA). In the present work, the powders were heated at the rate of 3 K/min from room temperature to 1400 °C. The powders were subsequently cooled to room temperature, after holding for 0.5 h at 1400 °C. All the measurements were performed in static air. The DTA/TGA measurements were carried on a Netzsch STA 409C.

3.2.3 X-ray diffraction (XRD)

Room temperature XRD

Phase characterization of the synthesized powders was carried out using XRD. Unit cell parameters were determined by Rietveld refinement. From the identified phases and unit cell parameters, the solid solution limit of the substitution cations was determined. The theoretical density, ρ_{TD} of the samples was determined by the equation below;

$$\rho_{TD} = \frac{m \cdot Z}{V \cdot N_A} \qquad \text{Eq. 14}$$

where, m is the molar mass, Z = number of atoms per unit cell, V is the volume of unit cell and N_A is Avogadro's number. With this theoretical density, the relative density of the bulk samples was determined by Archimedes method. The XRD results then were represented in terms of *Cu-*$K_{\alpha,\beta}$ radiation intensity (arbitrary unit) versus the diffraction. In the present work, the scan speed was set at 0.01 or 0.02 ° for 5-10 s. The measurements were performed either by Siemens D5000 or Bruker D4 diffractometer.

High temperature XRD

The experiment of high temperature XRD was performed in order to understand the thermal behavior of $Gd_4Ti_2O_{10}$ sintered at 1400 °C. The experiment was carried out with Siemens D5000 diffractometer. The scanning angle was set at 2Θ=(29-39°). The heating was performed from room temperature, RT to 1000 °C (hold) and cooling down to RT. The data were collected at every 100 °C interval.

3.2.4 Archimedes method

The relative density of sintered bars or pellets was determined by Archimedes method. The dry weight of the sample was determined by balance and denoted as W_{dry}. Later the sample was submerged in distilled water, vacuumed with a pump, weighted again in water and denoted as W_{sub}. Finally the sample was removed from the water and weighted again as W_{wet}. The apparent density of the sample, ρ_{app} was determined according to

$$\rho_{app} = \frac{W_{dry}}{W_{wet} - W_{sub}} \cdot \rho_{H_2O} \qquad \text{Eq. 15}$$

and the relative density, ρ_{rel} was determined by,

$$\rho_{rel} = \frac{\rho_{app}}{\rho_{TD}} \cdot 100\% \qquad \text{Eq. 16}$$

where ρ_{TD} is the theoretical density of the materials obtained from XRD measurements.

3.2.5 Raman spectroscopy

The Raman spectroscopic measurements were recorded with Horiba Jobin Yvon SpexT64000 equipped with two scanning mechanism, one for the foremonochromator and the other one for the spectrograph. SpexT64000 is equipped with 1800 grooves/mm gratings. The 488 nm line of an Ar^+ ion laser (COHERENT Innova® 300C Series) was used for the probe excitation. The spectra were collected in backscattering geometry with a confocal Raman microscope equipped with Olympus MPlan 100x objective. The detection of the Raman signal was carried out with a CCD detector operating at liquid nitrogen temperature. The laser power and the acquisition time used in the measurements are indicated in each figure caption. This measurement and facilities were provided by *Zentralabteilung für Chemische Analysen* (ZCH) of *Forschung Zentrum Jülich* (FZJ), Jülich, Germany.

3.2.6 Scanning electron microscopy (SEM)

The microstructural analysis of the sintered bars was carried out by scanning electron microscopy (SEM, Ultra55, Zeiss). The samples were cut and embedded in resin so that they could be mirror polished. All the samples were sputtered with platinum of about 20 - 30 nm and a copper band was attached in order to make the sample conducting. The measurements began with back scattered electron (BSE) source. From BSE image analysis, the main and additional phases present in the samples could be indentified by observing the difference in gray scale contrast. The densifications of the samples were concluded after the pores in the samples were determined with the aid of secondary electron (SE) source. From SE images analysis, the presence of glowing effect observed around the darker region of the image led to the conclusion of presence of pores. To confirm the phases observed from BSE and SE results, the elementals analysis were performed on the samples by energy dispersive X-ray (EDX) spectroscopy, (Energy355, INCA). From the trace elements, the additional phases were characterized.

3.2.7 Electrical conductivity measurements

4-probes DC measurements

These measurements were carried out with powders that had been sintered to bars with dimensions of 5 x 40 x 2-3 mm^3 at higher temperatures (1400 to 1600 °C) to obtain relative densities of more than 90%. The total electrical conductivity (σ) of the sintered bars were measured by 4-probes DC technique at temperatures between 200 and 900 °C in air using silver wires and silver paste as contacts. Fig. 19 below shows the schematic diagram of the 4-probes DC measurement set up.

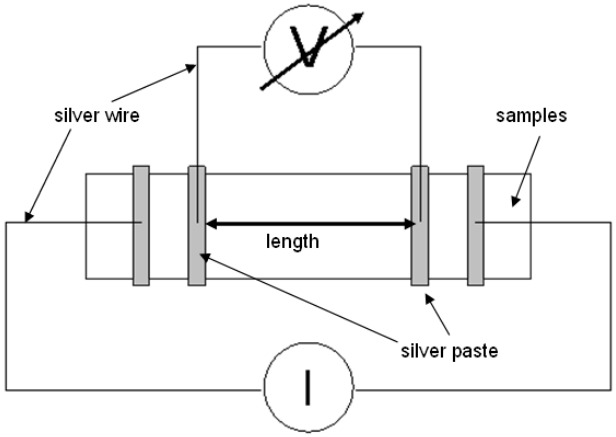

Fig. 19: The schematic diagram of 4-probe DC conductivity measurement set up.

The total electrical conductivity, σ was calculated by the equation below,

$$\sigma = \frac{l \cdot I}{A \cdot U} \qquad \text{Eq. 17}$$

where l is the length in cm, I is the current in ampere, A is area of the cross section in cm^2 and V is the voltage in Volt. The unit of σ is $(\Omega cm)^{-1}$ or Scm^{-1}.

AC impedance spectroscopy

Sintered pellets (diameter: 8 mm, thickness: 1-2 mm) were subjected to AC impedance spectroscopy measurements to determine the bulk and grain boundary conductivity using platinum paste as the contact material. The impedance spectroscopy data were collected using a frequency analyzer (Alpha–A Analyzer, Novocontrol) over the frequency range of 100 mHz – 3 MHz with an applied voltage of V_{rms} = 50 mV. The stray inductance of the empty holder amounts to 18 nH. The measurement was performed in air in the temperature range from 400 to 900 °C. This measurement and facilities were provided by *Lehrstuhl für Physikalische Chemie, Montanuniversität Leoben, Austria*.

3.2.8 Thermal expansion measurements

Powders were uni-axially pressed with a pressure of 100 MPa for 3 minutes into bars with dimensions of 5 x 40 x 2-3 mm^3. The pressed bars were sintered at higher temperatures

(1400-1600 ℃) to achieve a relative density of more than 90%. The sintered bars were cut into 25 mm long specimens to fit into the dilatometer of Netzsch DIL 402C, Germany. The thermal expansion measurements were performed with heating rate of 3K/min in the range of 25 to 1400 ℃.

4 Results and discussion

4.1 Oxy-cuspidine $Gd_4Al_2O_9$, $Gd_4Al_{2-x}Mg_xO_{9-x/2}$ and $Gd_{4-x}(Ca,Sr)_xAl_2O_{9-x/2}$.

In this section, results regarding $Gd_4Al_2O_9$ and substituted oxy cuspidine series i.e. $Gd_4Al_{2-x}Mg_xO_{9-x/2}$ and $Gd_{4-x}(Ca,Sr)_xAl_2O_{9-x/2}$ are reported. In line with the objective of the thesis, chemical analysis was carried out to confirm the precision of the chemical compositions and phase analysis was carried out to confirm phase purity of $Gd_4Al_2O_9$ and detect the solid solubility limits of the divalent cations substituting the Gd or Al site of $Gd_4Al_2O_9$. Based on the similarity of ionic radius, Ca^{2+} and Sr^{2+} were substituted at Gd^{3+} while Mg^{2+} was substituted at the Al^{3+} [116]. Subsequently these materials were investigated for their electrical and thermal properties in order to validate their role as an ionic conductor for SOFCs application.

4.1.1 Synthesis and chemical analysis

The pure compound of $Gd_4Al_2O_9$ and the series $Gd_4Al_{2-x}Mg_xO_{9-x/2}$ and $Gd_{4-x}(Ca,Sr)_xAl_2O_{9-x/2}$ were synthesized by citric complexation method as described in section 3.1.1. Chemical analysis by ICP-OES was carried out for powders calcined at 900 °C, in order to confirm the stoichiometry of the compounds. The results of the chemical analysis are tabulated in Table 3.

Table 3: The nominal and experimental compositions of $Gd_4Al_2O_9$, $Gd_4Al_{2-x}Mg_xO_{9-x/2}$ and $Gd_{4-x}(Ca,Sr)_xAl_2O_{9-x/2}$.

No	Nominal composition	Experimental composition
1.	$Gd_4\,Al_2\,O_9$	$Gd_{3.96}\,Al_{1.95}\,O_9$
2.	$Gd_{4.00}\,Al_{1.90}\,Mg_{0.10}\,O_{8.95}$	$Gd_{3.96}\,Al_{1.95}\,Mg_{0.09}\,O_{9-\delta}$
3.	$Gd_{4.00}\,Al_{1.75}\,Mg_{0.25}\,O_{8.88}$	$Gd_{3.95}\,Al_{1.76}\,Mg_{0.29}\,O_{9-\delta}$
4.	$Gd_{4.00}\,Al_{1.50}\,Mg_{0.50}\,O_{8.75}$	$Gd_{3.90}\,Al_{1.50}\,Mg_{0.60}\,O_{9-\delta}$
5.	$Gd_{4.00}\,Al_{1.25}\,Mg_{0.75}\,O_{8.63}$	$Gd_{3.96}\,Al_{1.27}\,Mg_{0.77}\,O_{9-\delta}$
6.	$Gd_{4.00}\,Al_{1.00}\,Mg_{1.00}\,O_{8.50}$	$Gd_{3.97}\,Al_{1.03}\,Mg_{1.01}\,O_{9-\delta}$
7.	$Gd_{4.00}\,Al_{0.50}\,Mg_{1.50}\,O_{8.25}$	$Gd_{3.97}\,Al_{0.51}\,Mg_{1.52}\,O_{9-\delta}$
8.	$Gd_{3.99}\,Ca_{0.01}\,Al_{2.00}\,O_{8.99}$	$Gd_{4.00}\,Ca_{0.01}\,Al_{1.99}\,O_{9-\delta}$
9.	$Gd_{3.95}\,Ca_{0.05}\,Al_{2.00}\,O_{8.98}$	$Gd_{3.95}\,Ca_{0.05}\,Al_{1.99}\,O_{9-\delta}$
10.	$Gd_{3.90}\,Ca_{0.10}\,Al_{2.00}\,O_{8.95}$	$Gd_{3.91}\,Ca_{0.10}\,Al_{1.98}\,O_{9-\delta}$
11.	$Gd_{3.75}\,Ca_{0.25}\,Al_{2.00}\,O_{8.88}$	$Gd_{3.75}\,Ca_{0.26}\,Al_{1.98}\,O_{9-\delta}$
12.	$Gd_{3.50}\,Ca_{0.50}\,Al_{2.00}\,O_{8.25}$	$Gd_{3.43}\,Ca_{0.54}\,Al_{2.02}\,O_{9-\delta}$
13.	$Gd_{3.99}\,Sr_{0.01}\,Al_{2.00}\,O_{8.99}$	$Gd_{3.98}\,Sr_{0.01}\,Al_{2.01}\,O_{9-\delta}$
14.	$Gd_{3.95}\,Sr_{0.05}\,Al_{2.00}\,O_{8.98}$	$Gd_{3.94}\,Sr_{0.06}\,Al_{2.00}\,O_{9-\delta}$
15.	$Gd_{3.90}\,Sr_{0.10}\,Al_{2.00}\,O_{8.95}$	$Gd_{3.89}\,Sr_{0.10}\,Al_{2.01}\,O_{9-\delta}$
16.	$Gd_{3.75}\,Sr_{0.25}\,Al_{2.00}\,O_{8.88}$	$Gd_{3.76}\,Sr_{0.25}\,Al_{1.99}\,O_{9-\delta}$
17.	$Gd_{3.50}\,Sr_{0.50}\,Al_{2.00}\,O_{8.25}$	$Gd_{3.51}\,Sr_{0.54}\,Al_{1.95}\,O_{9-\delta}$

Taking into consideration of the experimental errors, the stoichiometries of all synthesized powders seem are in good agreement with nominal stoichiometry.

4.1.2 DTA/TGA

The DTA / TGA measurements were performed to observe the phase stability in the temperature range of 25 to 1400 °C. A few of the calcined powders, of $Gd_4Al_2O_9$, $Gd_4Al_{1.50}Mg_{0.50}O_{8.75}$, $Gd_{3.95}Ca_{0.50}Al_2O_{8.75}$ and $Gd_{3.95}Sr_{0.50}Al_2O_{8.75}$, were selected. High concentrations of cation substitution were selected so that the response of DTA to powders in term of cation influence can be observed distinctly. $Gd_4Al_2O_9$ was used as comparison towards the substituted compositions by comparing the DTA/TGA results. Fig. 20 shows the results of DTA and TGA of the respective powders.

In Fig. 20, no significant reaction was observed from DTA results during heating except for $Gd_4Al_{1.50}Mg_{0.50}O_{8.75}$ (Fig. 20b). An exotherm was observed for this powder at 1250 °C

indicating the recrystallization of $Gd_4Al_2O_9$ structure. This result is better discussed together with XRD analysis in the next section. In terms of substitutional influence the DTA curves of $Gd_{3.95}Ca_{0.50}Al_2O_{8.75}$ and $Gd_4Al_2O_9$ have almost the same profile indicating that the Ca^{2+} substitutional did not give much influence thus showing that these materials are more stable upon heating. The DTA curves of $Gd_4Al_{1.50}Mg_{0.50}O_{8.75}$ and $Gd_{3.95}Sr_{0.50}Al_2O_{8.75}$ (Fig. 20d) did not follow the profile of pure $Gd_4Al_2O_9$ thus showing clear influences of Mg^{2+} and Sr^{2+} in both materials.

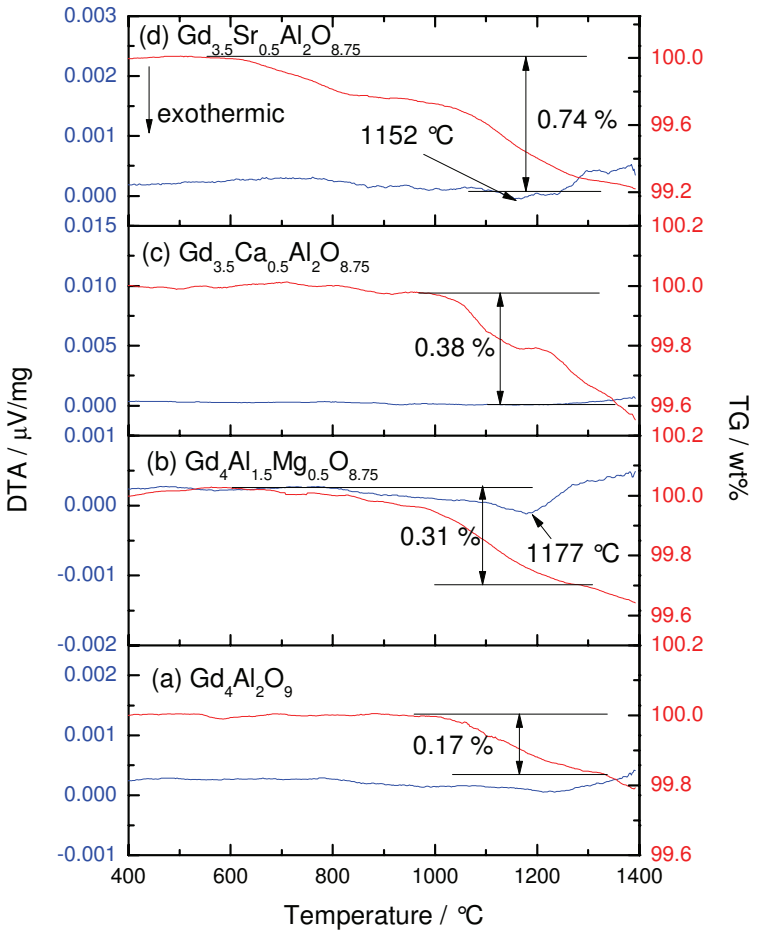

Fig. 20: DTA and TG for (a) $Gd_4Al_2O_9$, (b) $Gd_4Al_{1.50}Mg_{0.50}O_{8.75}$, (c) $Gd_{3.95}Ca_{0.50}Al_2O_{8.75}$ and (d) $Gd_{3.95}Sr_{0.50}Al_2O_{8.75}$.

In Fig. 20, small weight loss of less than 1% was observed for all the compositions. 0.17, 0.31, 0.38 and 0.74 % weight loss was observed in the range of 1000 to 1350 °C for $Gd_4Al_2O_9$, $Gd_4Al_{1.50}Mg_{0.50}O_{8.75}$, $Gd_{3.95}Ca_{0.50}Al_2O_{8.75}$ and $Gd_{3.95}Sr_{0.50}Al_2O_{8.75}$ as shown in Fig. 20a, b, c and d respectively. However it was accompanied by distinct signal in the DTA profile. The plausible reason for the observed weight loss could be minor crystallite changes. Sintering temperature of 1600 °C was concluded for all the samples considering the DTA/TGA results.

4.1.3 XRD analysis

Phase characterization for the calcined and sintered powders was carried out using room temperature XRD. The results of phase confirmation, phase quantification and lattice parameter determination of the un-substituted and substituted $Gd_4Al_2O_9$ are reported accordingly in the following section.

4.1.3.1 XRD results of $Gd_4Al_2O_9$

From the XRD analysis of the $Gd_4Al_2O_9$ sample, a single phase of polycrystalline $Gd_4Al_2O_9$ was obtained for both as-calcined and sintered powders. The room temperature XRD pattern matched with $Gd_4Al_2O_9$ phase [117]. Both samples crystallize in monoclinic symmetry with space group $P2_1/c$. The formula per unit cell, *Z*, is 4. The as-calcined and sintered XRD pattern of $Gd_4Al_2O_9$ is shown in Fig. 21a and b. In terms of crystallinity, the result shows that the sintered samples crystallized better than as-calcined samples.

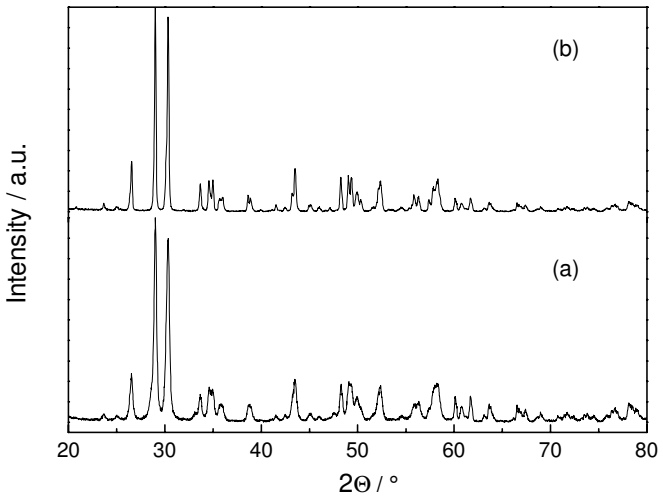

Fig. 21: Room temperature XRD pattern at 20 < 2Θ < 80 °for (a) as-calcined and (b) sintered powders of $Gd_4Al_2O_9$.

These XRD results were further analyzed using reported crystal structure data of $Eu_4Al_2O_9$ [118] and indexed accordingly to determine the lattice parameters using Rietveld refinement. The lattice parameters for as-calcined powder are a = 7.5363 (5) Å, b = 10.6319 (5) Å and c = 11.1939 (5) Å and β = 109.03 (1) ° and for the sintered powder are a = 7.5347 (2) Å, b = 10.6306 (4) Å and c = 11.2010 (4) Å and β = 109.00 (2) °. The obtained lattice parameters are in good agreement with former reports [105]. The crystal structure of oxy-cuspidine $Gd_4Al_2O_9$ obtained from the Reitveld refinement is similar to the structure obtained in [9]. Fig. 22 below shows the refined crystal structure of sintered $Gd_4Al_2O_9$.

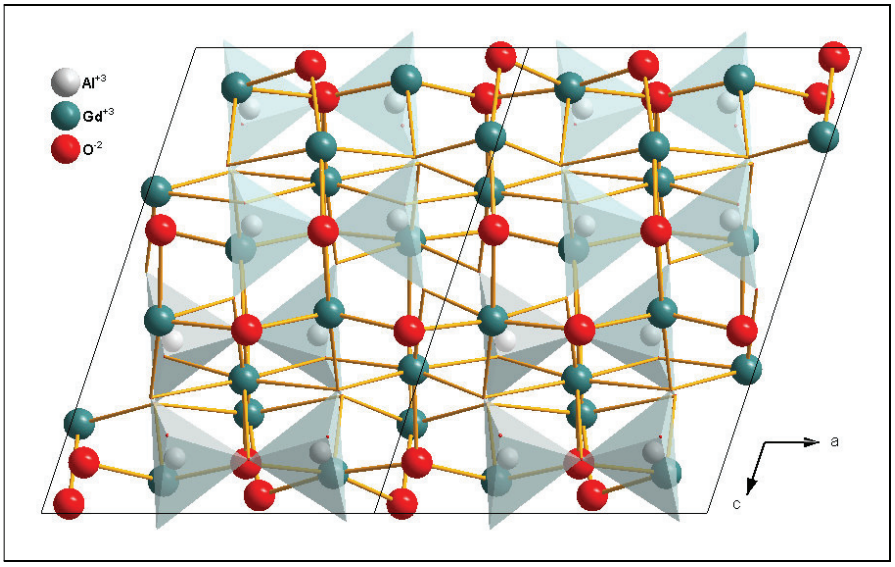

Fig. 22: The refined crystal structure of as-sintered $Gd_4Al_2O_9$ sample.

4.1.3.2 XRD results of $Gd_4Al_{2-x}Mg_xO_{9-x/2}$ series

Only sintered samples of the series $Gd_4Al_{2-x}Mg_xO_{9-x/2}$ with x=0, 0.10, 0.25 and 0.50 mol Mg per unit formula were investigated since the prime objective was to investigate the electrical conductivity and thermal expansion of sintered bulk samples. The XRD pattern of $Gd_4Al_{2-x}Mg_xO_{9-x/2}$ (x =0, 0.10, 0.25 and 0.50) as shown in Fig. 23 corresponds to that of monoclinic $Gd_4Al_2O_9$ with presence of additional Gd_2O_3 [117].

The ionic radius of Al^{3+} and Mg^{2+} with the coordination number 4 is 0.54 and 0.72 Å respectively [116]. Thus, theoretically substitution of Al^{3+} or Ga^{3+} by Mg^{2+} should be feasible due to the smaller ionic radius. Such substitution for $La_{1-x}Sr_xGa_{1-y}Mg_yO_3$ [119] and $La_{1-x}Sr_xAl_{1-y}Mg_yO_3$ [120] has already been reported. However, the additional peaks observed could be easily attributed to Gd_2O_3.

The semi-quantitative analysis from XRD showed that the amount of Gd_2O_3 increased with increasing Mg concentration. The amount in term of mass fraction of Gd_2O_3 was in the range of 3-12% (Table 4). From this observation, it was obvious that the Mg^{2+} was not able to substitute at Al^{3+} site thus inducing the formation of additional Gd_2O_3 phase. Therefore the substitution limit for Mg can be anticipated to be far below 0.10 mol Mg per formula unit.

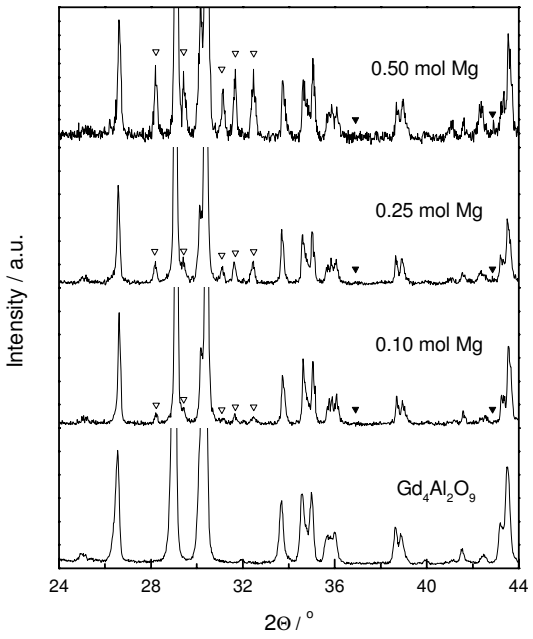

Fig. 23: Room temperature XRD patterns at 24 < 2Θ < 44 °of the series $Gd_4Al_{2-x}Mg_xO_{9-x/2}$ (x = 0, 0.10, 0.25, and 0.50) after sintering at 1600 °C for 6 h. The reflections marked with open and close triangle symbols indicate the appearance of Gd_2O_3 and MgO [117], respectively.

From the XRD results, only Gd_2O_3 was clearly observed as an additional phase resulting from Mg^{2+} substitution. In Fig. 19, the peaks for the MgO were marked to show if MgO could also be present as an additional phase. SEM investigation was performed to get more information about the formation of this additional phase and is discussed subsequently. Table 4 shows the lattice parameters and the semi quantitative analysis of $Gd_4Al_{2-x}Mg_xO_{9-x/2}$ series.

Table 4: Lattice parameter and semi-quantitative analysis of $Gd_4Al_{2-x}Mg_xO_{9-x/2}$ series.

x (mol)	**Lattice parameters**					**XRD (wt %)**	
	a (Å)	*b* (Å)	*c* (Å)	*β* (°)	V (Å^3)	$Gd_4Al_2O_9$	Gd_2O_3
0	7.5347(2)	10.6306(4)	11.2010(4)	109.0	848.3	100	0
0.10	7.5342(4)	10.6336(5)	11.2058(6)	109.0	848.9	97	3
0.25	7.5333(5)	10.6305(9)	11.2033(9)	109.0	848.3	94	6
0.50	7.5330(5)	10.6303(9)	11.2029(9)	109.0	848.2	88	12

The lattice parameters along *b*-axis and ***β*** angle did not change with increasing Mg^{2+} concentration. Along the *a* and *c*-axis, a non linear trend was observed indicating no effect of Mg^{2+} concentration. Overall the unit cell volume did not change significantly with increasing Mg^{2+} concentration.

4.1.3.3 XRD results of $Gd_{4-x}(Ca,Sr)_xAl_2O_{9-x/2}$ series

The XRD results of the sintered powders of the series $Gd_{4-x}(Ca,Sr)_xAl_2O_{9-x/2}$ with x=0, 0.01, 0.05, 0.10 and 0.25 mol per formula unit are reported accordingly. Fig. 24a and b shows the XRD patterns of the $Gd_{4-x}(Ca,Sr)_xAl_2O_{9-x/2}$ series.

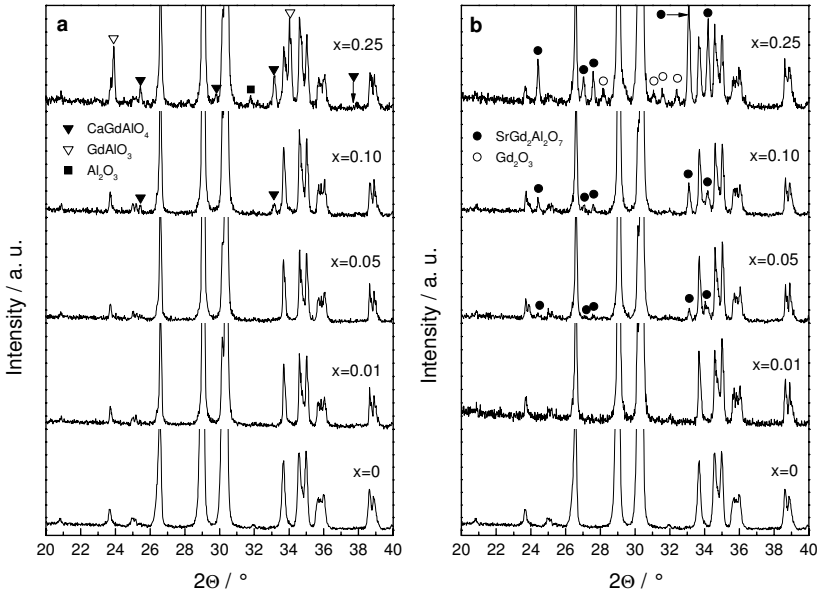

Fig. 24: Room temperature XRD patterns at 20 < 2Θ < 40 °of (a) $Gd_{4-x}Ca_xAl_2O_{9-x/2}$ and (b) $Gd_{4-x}Sr_xAl_2O_{9-x/2}$ at room temperature. The un-indexed peaks belong to the monoclinic $Gd_4Al_2O_9$ phase [117].

The room temperature XRD pattern for the sintered powders revealed that the main phase of $Gd_{4-x}Ca_xAl_2O_{9-x/2}$ and $Gd_{4-x}Sr_xAl_2O_{9-x/2}$ samples was monoclinic $Gd_4Al_2O_9$. According to the observed appearance of additional phases, the substitution limit for Ca and Sr was found between x = 0.05 - 0.10 mol and 0.01 - 0.05 mol, respectively. At higher substitution levels of Ca the phases $GdAlO_3$, $CaGdAlO_4$ and Al_2O_3 were observed in Fig. 24a [117] and for Sr substitution (Fig. 24b), $SrGd_2Al_2O_7$ and Gd_2O_3 phases were detected [117]. The lattice parameters of phase pure samples are shown in Table 5. These results are also in good agreement with the data reported in [9] and [105].

Table 5: The lattice parameters for the $Gd_{4-x}(Ca,Sr)_xAl_2O_{9-x/2}$ series.

Samples	*a* (Å)	*b* (Å)	*c* (Å)	*β* (°)	*V* (Å^3)
$Gd_4Al_2O_9$	7.5347 (2)	10.6306 (4)	11.2010 (4)	109.00 (2)	848.3
$Gd_4Al_2O_9$ [9]	7.5382 (1)	10.6393 (2)	11.2113 (2)	108.9 (1)	850.2
$Gd_4Al_2O_9$ [105]	7.563 (2)	10.679 (6)	11.246 (2)	109.2 (2)	857.9
$Gd_{3.99}Ca_{0.01}Al_2O_{8.99}$	7.539 (1)	10.639 (1)	11.211 (1)	108.99 (1)	850.3
$Gd_{3.95}Ca_{0.05}Al_2O_{8.98}$	7.536 (1)	10.644 (1)	11.212 (1)	108.98 (1)	850.5
$Gd_{3.99}Sr_{0.01}Al_2O_{8.99}$	7.541 (1)	10.643 (2)	11.215 (2)	108.99 (1)	851.1

4.1.4 Raman spectroscopy

4.1.4.1 Raman spectra of $Gd_4Al_2O_9$

The investigation of Raman spectra for $Gd_4Al_2O_9$ or similar structure such as $RE_4Al_2O_9$ (RE = rare earth) has never been reported in literature. Therefore the information regarding vibrations assignment is not available thus making analysis difficult. The main concern in this measurement is to confirm the phase of materials as investigated by XRD. Fig. 25 below shows the Raman spectra of $Gd_4Al_2O_9$.

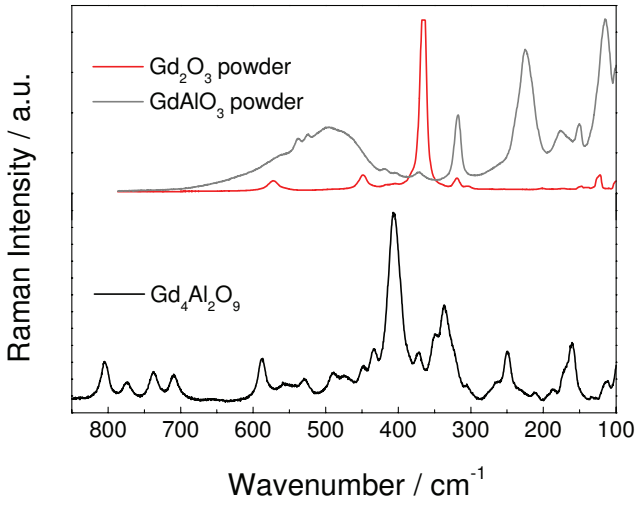

Fig. 25: The Raman spectra of sintered $Gd_4Al_2O_9$ and calcined powders (900 °C) of $GdAlO_3$ and Gd_2O_3. Excitation: 488 nm, 2.6 mW, 50x, 10 cycles/30 seconds.

Since XRD result confirmed the presence of phase pure $Gd_4Al_2O_9$ it can be concluded that the above Raman spectrum is characteristic of monoclinic $Gd_4Al_2O_9$ structure. However, the presence of any additional phase less than 5 wt% could not be detected by XRD. Thus Raman spectra of $GdAlO_3$ and Gd_2O_3 were compared with that obtained for $Gd_4Al_2O_9$ sample. It was observed that none of those are equivalent to that of $Gd_4Al_2O_9$. Therefore all of the bands observed in these spectra uniquely belong to the AlO_4 tetrahedra and GdO_7/GdO_8 octahedra. The bands of $Gd_4Al_2O_9$ are 805, 772, 737, 709, 587, 557, 528, 489, 474, 447, 433, 407, 371, 349, 336, 306, 265, 250, 213, 187, 161, 132 and 112 cm^{-1}. Due to the absence of any vibrations of Gd_2O_3 and $GdAlO_3$ in the Raman spectra (Fig. 25), it can be pre-concluded that the oxy-cuspidine $Gd_4Al_2O_9$ sample is a pure phase.

4.1.4.2 Raman spectra of $Gd_4Al_{2-x}Mg_xO_{9-x/2}$ series

The Raman spectra of the sintered $Gd_4Al_{2-x}Mg_xO_{9-x/2}$ with x=0, 0.10, 0.25 and 0.50 are shown in Fig. 26. All samples show a main phase of monoclinic $Gd_4Al_2O_9$. This is an affirmative confirmation of the room temperature XRD results mentioned previously.

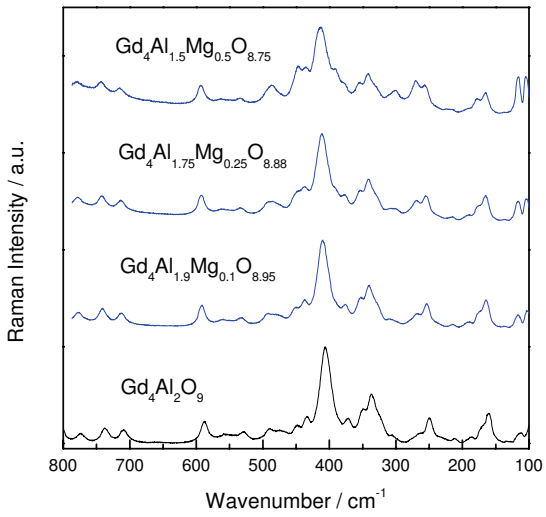

Fig. 26: Raman spectra of (a) $Gd_4Al_2O_9$, (b) $Gd_4Al_{1.90}Mg_{0.10}O_{8.95}$,(c) $Gd_4Al_{1.75}Mg_{0.25}O_{8.88}$ and (d) $Gd_4Al_{1.50}Mg_{0.50}O_{8.75}$ compounds. Excitation: 488 nm, 1.8 mW, 50x, 10 cycles/30 seconds.

Through analyzing the spectra with high Mg content, it was found that it was almost identical to oxy-cuspidine $Gd_4Al_2O_9$ except for the bands at 250 – 300, 460, 480 and 650 cm^{-1}. These additional vibration bands can be attributed to the presence of small amount of Gd_2O_3 phase as detected by room temperature XRD. The spectra of $Gd_4Al_{1.75}Mg_{0.25}O_{8.88}$ and $Gd_4Al_{1.50}Mg_{0.50}O_{8.75}$ clearly showed additional vibrational bands at 300 cm^{-1} which belong to the hexagonal Gd_2O_3 bands [117] and were also detected by room temperature XRD.

4.1.4.3 Raman spectra of $Gd_{4-x}(Ca,Sr)_xAl_2O_{9-x/2}$ series

The Raman spectra of $Gd_{4-x}(Ca,Sr)_xAl_2O_{9-x/2}$ series are shown in Fig. 27. From these results, similar conclusions were derived as for the $Gd_4Al_{2-x}Mg_xO_{9-x/2}$ series. From Fig. 27, all samples have monoclinic $Gd_4Al_2O_9$ as the main phase.

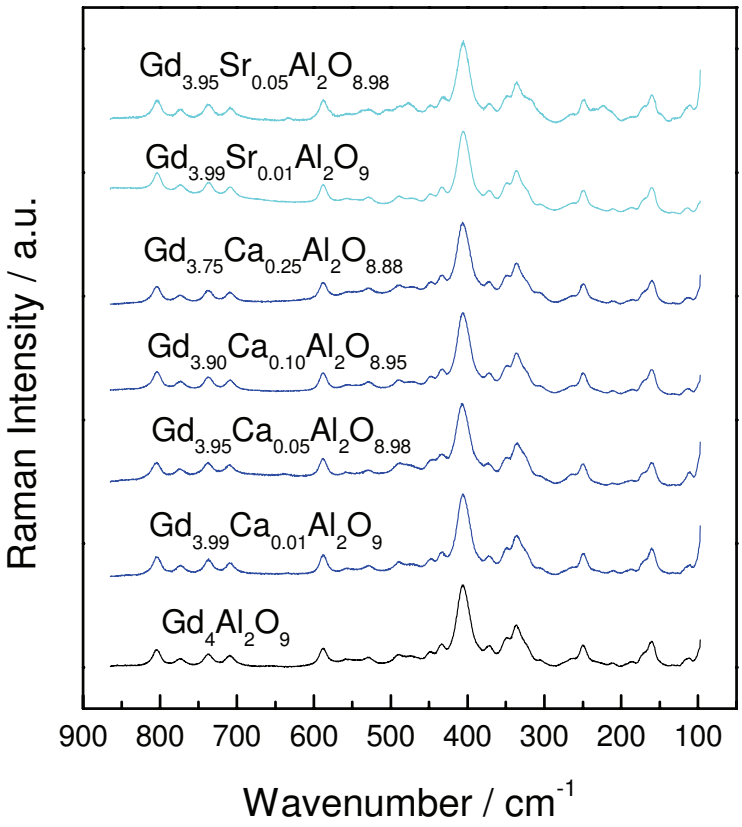

Fig. 27: The Raman spectroscopy of $Gd_{4-x}(Ca, Sr)_xAl_2O_{9-x/2}$. Excitation: 488 nm, 1.8 mW, 50x, 10 cycles/30 seconds.

Looking at the Raman spectra $Gd_{4-x}Ca_xAl_2O_{9-x/2}$ in Fig. 27, all the substituted samples showed almost identical spectra as that of $Gd_4Al_2O_9$. From the XRD results reported previously, the solid solution limit of Ca^{2+} is between 0.05 and 0.10 mol per formula unit. Above the limit, $CaGdAlO_4$, $GdAlO_3$ and Al_2O_3 were present as additional phases. It is expected to observe the significant bands that correspond to these additional phases. However, no distinct bands were observed.

Since Ca^{2+} was introduced to substitute Gd^{3+} in $Gd_4Al_2O_9$, the influences of Ca^{2+} concentration in the series were observed. Fig. 28 shows the shift of the bands either to low or high frequency corresponding to an increasing of Ca^{2+} concentration. Each point in Fig. 28 shows the bands of the series in the range of 200 to 600 cm^{-1}. The shifts of the bands were compared to the strongest band of $Gd_4Al_2O_9$ at 407 cm^{-1}. Looking at this particular band in Fig. 28, no shift was observed for 0.01 and 0.05 mol Ca^{2+}. However small shifts were observed for 0.10 and 0.25 mol Ca^{2+} of about 2 cm^{-1}. Similar shifts were observed for others band except at 489, 433 and 336 cm^{-1} with average shifts about 2 cm^{-1}.

It is rather weak to conclude that there is clear evidence that the increasing of Ca^{2+} concentration do effect the spectra because the difference of 2 cm^{-1} can be easily attributed to measurement or device errors. Nevertheless, if the finding from Raman spectra is analyzed together with the finding from XRD, it can be concluded that the influences of Ca^{2+} to the $Gd_4Al_2O_9$ structure is agreeable.

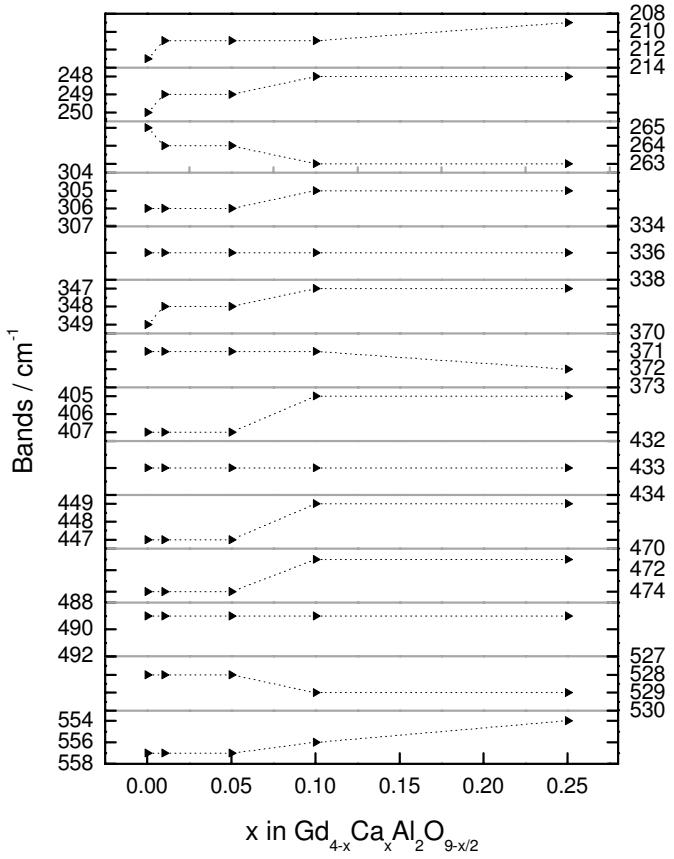

Fig. 28: Deviation in the frequency of different bands with the increasing amounts of Ca^{2+} in $Gd_{4-x}(Ca,Sr)_xAl_2O_{9-x/2}$ series.

For the Raman spectra of $Gd_{4-x}Sr_xAl_2O_{9-x/2}$ as shown in Fig. 27 for $Gd_{3.99}Sr_{0.01}Al_2O_{8.99}$ and $Gd_{3.95}Sr_{0.05}Al_2O_{8.98}$, indicate the presence of oxy-cuspidine $Gd_4Al_2O_9$ phase. However, additional bands at 632, 540, 505, 475, 325, 300 and 225 cm^{-1} were observed for the spectra of $Gd_{3.95}Sr_{0.05}Al_2O_{8.98}$. Comparing with XRD results, the additional bands of that particular spectrum can be attributed to $SrGd_2Al_2O_7$. The influence of Sr^{2+} to $Gd_4Al_2O_9$ structure can be clearly observed in Fig. 29. The shifts of the band at 407 cm^{-1} of pure $Gd_4Al_2O_9$ to higher frequency was observed with increase in Sr^{2+} concentration. As discussed previously with the increases of Ca^{2+} concentration, similar results were obtained with Sr^{2+} concentration. Clear bands that not belong to cuspidines were clearly observed at 225, 320 and 505 cm^{-1}.

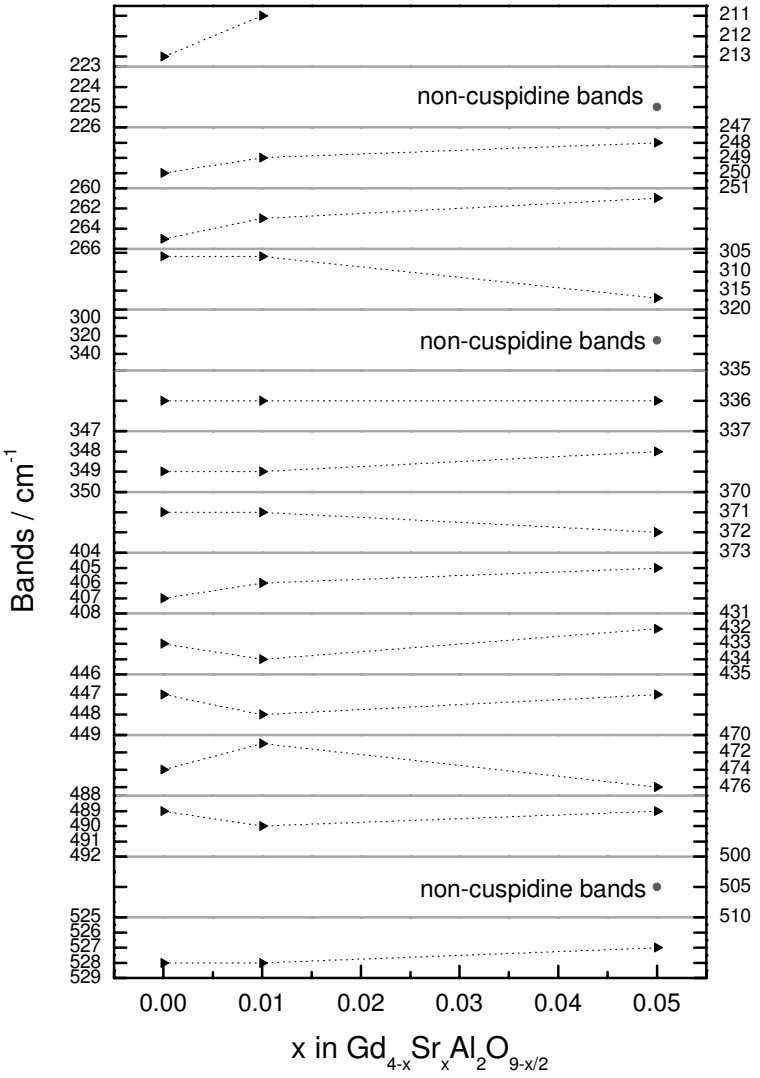

Fig. 29: Deviation in the frequency of different bands with the increasing amounts of Sr^{2+} in $Gd_{4-x}(Ca,Sr)_xAl_2O_{9-x/2}$ series.

4.1.5 Microstructural analysis

The microstructure investigation was performed for the series of $Gd_4Al_{2-x}Mg_xO_{9-x/2}$, $Gd_{4-x}Ca_xAl_2O_{9-x/2}$ and $Gd_{4-x}Sr_xAl_2O_{9-x/2}$. Information about the phases present in the samples can be obtained by analyzing the contrast of the back scattered images. The secondary electron images confirm whether darker regions in the samples are additional phases or pores. Thus final conclusion of the phases present can be confirmed and related to the phases detected from RT-XRD results.

4.1.5.1 Microstructural analysis of $Gd_4Al_{2-x}Mg_xO_{9-x/2}$

Microstructural investigations were carried on $Gd_4Al_{2-x}Mg_xO_{9-x/2}$ with x = 0, 0.10, 0.25 and 0.50 mol Mg. Back-scattered images obtained for the above mentioned samples are shown in Fig. 30. All the samples are rather dense and in good agreement with relative density obtained from Archimedes method. These values are shown in Table 6.

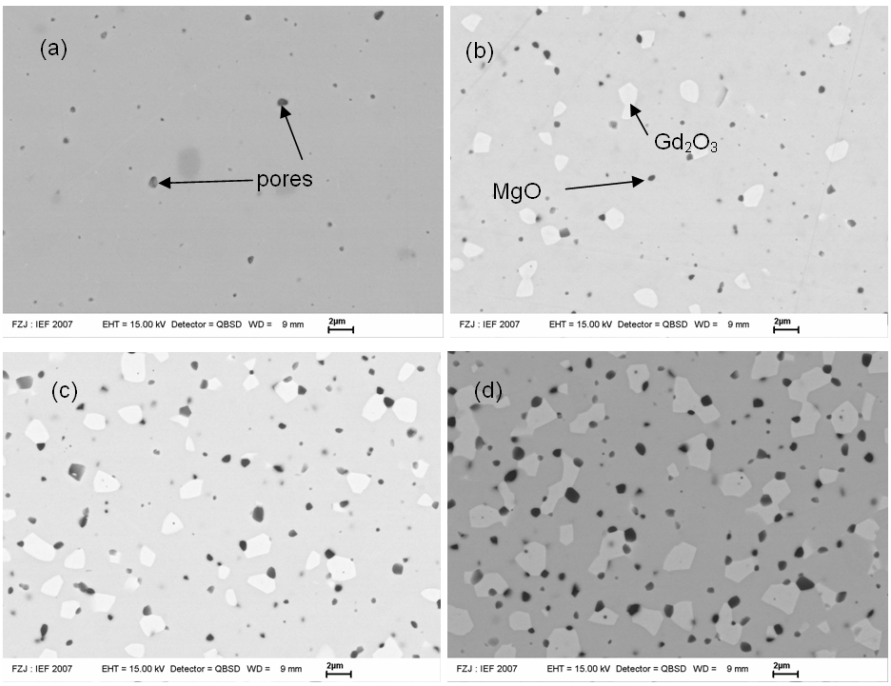

Fig. 30: Back-scattered images of (a) $Gd_4Al_2O_9$, (b) $Gd_4Al_{1.90}Mg_{0.10}O_{8.95}$, (c) $Gd_4Al_{1.75}Mg_{0.25}O_{8.88}$ and (d) $Gd_4Al_{1.50}Mg_{0.50}O_{8.75}$. In Fig. 30 b, c and d the dark spots indicate the presence of MgO while the light grey particles indicate Gd_2O_3.

$Gd_4Al_2O_9$ is pure phase. However, it contains some pores which can be clearly seen in Fig. 30a. The substituted $Gd_4Al_2O_9$ contains Gd_2O_3 and MgO as additional phases which were unambiguously identified by EDX analysis. The quantification of each phase was carried out via image analysis by measuring the area fraction of each phase. The results are shown in Table 6.

The experimental volume fractions were determined by using the area fractions obtained from SEM results. The area fractions were multiplied by the correction factor [121] which is 1.13 and 1.56 for irregular and spherical shapes, respectively.

Table 6: Relative density, Volume fraction of products by XRD and SEM analysis for $Gd_4Al_{2-x}Mg_xO_{9-x/2}$.

x	Relative density (%) (Archimedes)	Volume fractions, V_f of products				
		XRD analysis		SEM image analysis		
		$Gd_4Al_2O_9$	Gd_2O_3	$Gd_4Al_2O_9$	Gd_2O_3	MgO
0	98	1.00	-	1.00	-	-
0.10	98	0.97	0.03	0.91	0.08	0.009
0.25	99	0.95	0.05	0.89	0.10	0.013
0.50	99	0.91	0.09	0.77	0.18	0.047

4.1.5.2 Substitution limit of Mg^{2+} in $Gd_4Al_2O_9$

SEM data revealed the presence of MgO in the substituted $Gd_4Al_{2-x}Mg_xO_{9-x/2}$ along with monoclinic $Gd_4Al_2O_9$ and Gd_2O_3. This MgO phase remained undetected in XRD due to its smaller particle size and presumably highly disordered crystal structure. Furthermore MgO peaks could have been overlapped with complex peaks of $Gd_4Al_2O_9$ phase. The peaks of periclase MgO [117] are shown in Fig. 23 at 2Θ=38 and 43 °. Since the substitution with Mg always produced the additional phases of Gd_2O_3 and MgO, a chemical reaction according to Eq.18 can be concluded.

$$Gd_4Al_{2-x}Mg_xO_{9-x/2} \rightarrow \left(1-\frac{x}{2}\right)Gd_4Al_2O_9 + xGd_2O_3 + xMgO \qquad \text{Eq. 18}$$

When this equation is converted into an expression of volume fractions, the theoretical product formation with increasing Mg^{2+} concentration can be compared with the experimental results as shown in Fig. 31. The theoretical volume fractions of each product were determined simply by dividing the mass of products with theoretical density of the product. The theoretical density of $Gd_4Al_2O_9$, Gd_2O_3 and MgO are 6.41, 8.35 and 3.57 gcm^{-3} respectively, as obtained from the crystallographic data [117]. From the SEM results shown in Fig. 30 Gd_2O_3 and MgO phases were interpreted as irregular and spherical particles, respectively.

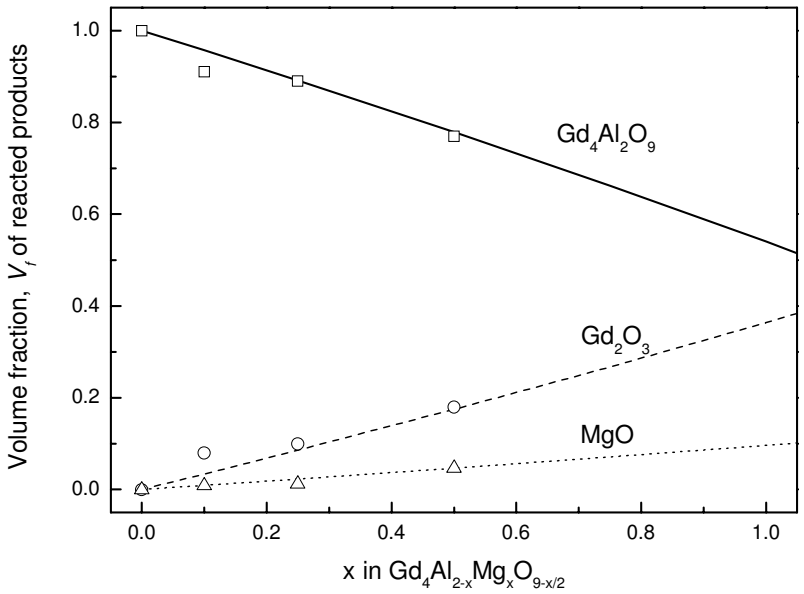

Fig. 31: Plot of the product formation according to equation 1 (lines), while the open symbols are the experimental results.

From Fig. 31 it can be seen that the amount of the experimental phase products follow the theoretical expectations, except for the compound with x = 0.10 mol Mg. Nevertheless, by assuming that all volume fractions fit very well with the theoretical values, no substitution is observed. This is a clear evidence that Mg^{2+} was not able to substitute the Al^{3+} in oxy-cuspidine $Gd_4Al_2O_9$.

4.1.5.3 Microstructural analysis of $Gd_{4-x}(Ca,Sr)_xAl_2O_{9-x/2}$ series.

The results obtained from SEM show that the sintered bars are very dense. The relative density varied between 95 and 98 %. Fig. 32 and Fig. 33 show the back scattered images of $Gd_{4-x}(Ca,Sr)_xAl_2O_{9-x/2}$ series with x=0.05 and 0.10 mol Ca and Sr, respectively, after sintering at 1600 °C.

From Fig. 32a, the dark areas were identified as pores as confirmed by secondary electron images. The light gray contrast was the enrichment of Gd atoms in the matrix of $Gd_4Al_2O_9$. In Fig. 32b the observed additional gray phase indicated presence of Ca element by EDX analysis. Thus the additional phase could be attributed to $CaGdAlO_4$ as observed in the XRD results (Fig. 24a).

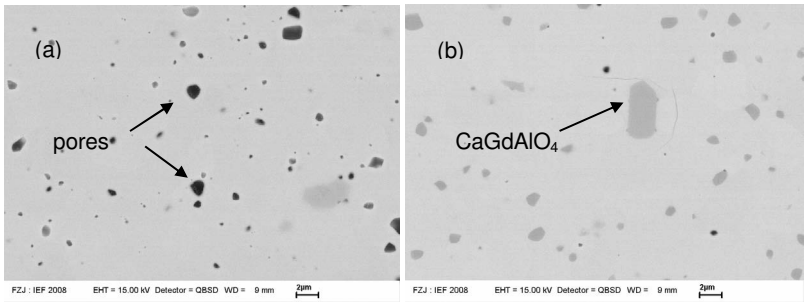

Fig. 32: Back-scattered SEM images of (a) $Gd_{3.9}Ca_{0.05}Al_2O_{8.98}$ and (b) $Gd_{3.9}Ca_{0.10}Al_2O_{8.95}$.

Similarly the gray phase in Fig. 33a and b could be attributed to the $SrGd_2Al_2O_7$ phase. This attribution was supported by EDX analysis where Sr element was clearly detected. In relation to the XRD results (Fig. 24b), the detected Sr elements belong to the phase of $SrGd_2Al_2O_7$. The EDX also confirmed the observed white area in Fig. 33a as Pt due to the sputtering of the samples. The dark areas were pores. Both samples are in good agreement with XRD results as shown in Fig. 24b.

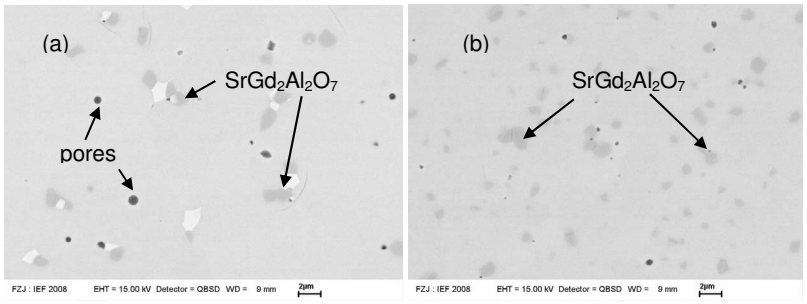

Fig. 33: Back-scattered SEM images of (a) $Gd_{3.9}Sr_{0.05}Al_2O_{8.98}$ and (b) $Gd_{3.9}Sr_{0.10}Al_2O_{8.95}$.

4.1.6 Electrical conductivity

Electrical conductivity was determined for selected samples by 4-probe DC measurement and AC impedance spectroscopy. The 4-probe DC conductivity measurements were performed for $Gd_4Al_{2-x}Mg_xO_{9-x/2}$ and $Gd_{4-x}(Ca,Sr)_xAl_2O_{9-x/2}$. However, AC impedance spectroscopy measurements were carried out only on pure phase $Gd_4Al_2O_9$, $Gd_{3.9}Ca_{0.05}Al_2O_{8.98}$ and $Gd_{3.9}Sr_{0.05}Al_2O_{8.98}$ samples. From the electrical conductivity values, the activation energy, E_a of the samples were calculated from the Arrhenius plot.

4.1.6.1 4-probes DC measurements of $Gd_4Al_{2-x}Mg_xO_{9-x/2}$

The electrical conductivity results for $Gd_4Al_{2-x}Mg_xO_{9-x/2}$ samples are shown in the form of an Arrhenius plot (Fig. 34). All samples showed increase in conductivity with temperature. This is typical semiconducting behavior of solids. The electrical conductivity of $Gd_4Al_2O_9$ at 900 °C was $\sigma = 1.88 \times 10^{-5}$ Scm^{-1}. This value is in good agreement with previous work [9]. From the same work, the electrical conductivity increased by introducing Ge^{4+} cations on the Al sites [9]. The highest electrical conductivity of $\approx 7.9 \times 10^{-4}$ Scm^{-1} was obtained for $Gd_4Al_{0.8}Ge_{1.2}O_{9.6}$ at 900 °C where the activation energy of 1.4 eV was reported [9], which gives clear evidence for a different conduction mechanism via interstitial oxygen ions or rotations of Al-O polyhedra.

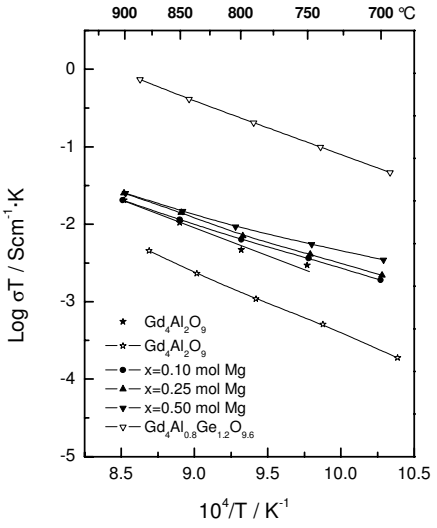

Fig. 34: Arrhenius plot of electrical conductivity for $Gd_4Al_{2-x}Mg_xO_{9-x/2}$ series. The open symbols belong to the series of $Gd_4Al_{2-x}Ge_xO_{9+x/2}$ [9].

The formation of MgO did not increase the electrical conductivity significantly as compared to $Gd_4Al_{2-x}Ge_xO_{9+x/2}$ series [9]. The reason is that Mg^{2+} was not able to substitute the Al^{3+} as explained in section 4.1.5.2. Due to this result, no oxygen vacancies were created, thus showing poor conductivity results. The activation energy (Table 7) did not change much upon the increasing of Mg^{2+} concentration. In-fact the values are close to 1.4 eV. This is another clear evidence that no oxygen vacancies were created instead it was interstitial oxygen conductivity mechanism [9, 99] that gave the samples conductivity values. Table 7 shows the electrical conductivity and activation energies of $Gd_4Al_{2-x}Mg_xO_{9-x/2}$ series.

Table 7: Electrical conductivity and activation energy, E_a of $Gd_4Al_{2-x}Mg_xO_{9-x/2}$ series.

Samples	σ_T (x 10^{-5} Scm^{-1}) at 900 °C	E_a(eV), 650 - 900 °C
$Gd_4Al_2O_9$	1.73	1.37
$Gd_4Al_2O_9$ [9]	0.32	1.40
$Gd_4Al_{1.90}Mg_{0.10}O_{8.95}$	1.74	0.96
$Gd_4Al_{1.75}Mg_{0.25}O_{8.88}$	2.15	0.97
$Gd_4Al_{1.50}Mg_{0.50}O_{8.75}$	2.15	0.76
$Gd_4Al_{0.8}Ge_{1.2}O_{9.6}$ [9]	12.18	1.36

4.1.6.2 4-probes DC measurement of $Gd_{4-x}(Ca,Sr)_xAl_2O_{9-x/2}$

For the materials substituted with Ca and Sr the highest electrical conductivity obtained at 900 °C was σ = 1.49 x 10^{-4} S/cm and σ = 9.43 x 10^{-5} S/cm for $Gd_{3.95}Ca_{0.05}Al_2O_{8.98}$ and $Gd_{3.95}Sr_{0.05}Al_2O_{8.98}$, respectively. Generally speaking for $Gd_{4-x}(Ca,Sr)_xAl_2O_{9-x/2}$, the electrical conductivity increased as the amount of Ca and Sr increased up to x = 0.10 and 0.05, respectively.

Comparing this value with the oxy-cuspidines prepared in this work, neither type of aliovalent substitution led to a significant increase in conductivity that could make these materials interesting for electrochemical devices. The activation energies calculated in the range of 650 to 900 °C from the temperature dependence of the electrical conductivity (Fig. 35) varied from 0.8 to 1.4 eV. The data of activation energies are shown in Table 8. The activation energy obtained for $Gd_4Al_2O_9$ was 1.37 eV, which is higher than the values obtained for the substituted compounds. These results show that the insulating $Gd_4Al_2O_9$ can accommodate oxygen vacancies with typical activation energies for oxygen ion

transport [122], but the number of oxygen vacancies is severely limited due to the low solubility of Ca and Sr in the lattice.

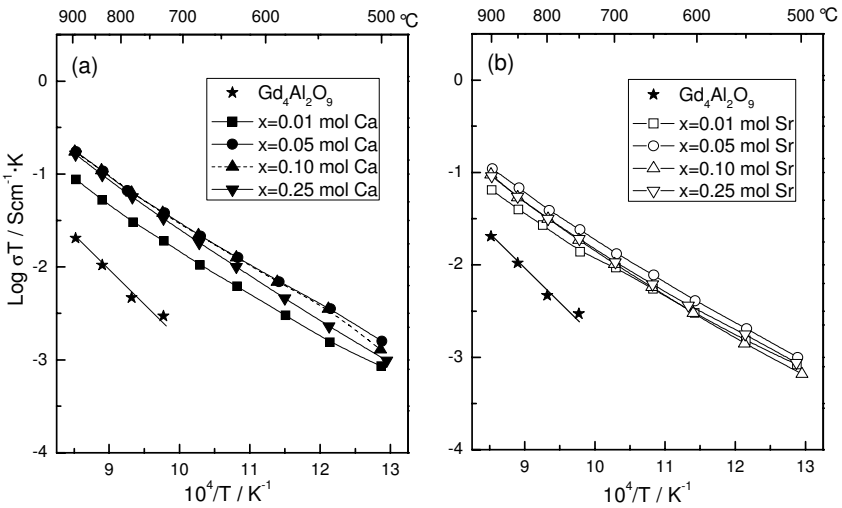

Fig. 35: Arrhenius plot of electrical conductivity of $Gd_{4-x}Ca_xAl_2O_{9-x/2}$ and $Gd_{4-x}Sr_xAl_2O_{9-x/2}$.

Table 8: Electrical conductivity and activation energy, *Ea* of $Gd_{4-x}(Ca, Sr)_xAl_2O_{9-x/2}$ series.

Samples	σ_T (x 10^{-5} Scm^{-1}) at 900 ℃	E_a, eV (650 – 900 ℃)
$Gd_4Al_2O_9$	1.73	1.37
$Gd_{3.99}Ca_{0.01}Al_2O_{8.99}$	7.39	0.84
$Gd_{3.95}Ca_{0.05}Al_2O_{8.98}$	14.9	0.84
$Gd_{3.90}Ca_{0.10}Al_2O_{8.95}$	14.7	0.92
$Gd_{3.75}Ca_{0.25}Al_2O_{8.88}$	13.9	0.94
$Gd_{3.99}Sr_{0.01}Al_2O_{8.99}$	5.49	0.80
$Gd_{3.95}Sr_{0.05}Al_2O_{8.98}$	9.43	0.87
$Gd_{3.90}Sr_{0.10}Al_2O_{8.95}$	10.5	0.90
$Gd_{3.75}Sr_{0.25}Al_2O_{8.88}$	7.88	0.89

4.1.6.3 AC impedance spectroscopy of $Gd_{4-x}(Ca,Sr)_xAl_2O_{9-x/2}$

AC impedance spectroscopy was performed for $Gd_4Al_2O_9$, $Gd_{3.95}Ca_{0.05}Al_2O_{8.98}$ and $Gd_{3.95}Ca_{0.05}Al_2O_{8.98}$. A typical impedance spectra of $Gd_4Al_2O_9$ which consisted of two semicircles in the complex impedance plane (Fig. 36a), were analyzed by fitting two components of resistance (R) and constant phase element (CPE) in a parallel circuit (R|CPE) as shown in Fig. 37.

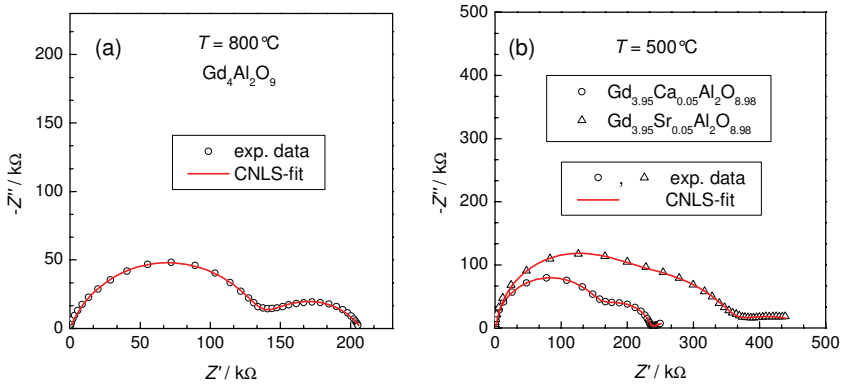

Fig. 36: Impedance spectra for (a) $Gd_4Al_2O_9$, T = 800 °C, and (b) $Gd_{3.95}M_{0.05}Al_2O_9$ (M = Ca, Sr), T = 500 °C. The red lines are complex non-linear (CNLS) fits.

Looking at Fig. 36a, the high frequency semicircle can be attributed to the bulk, whereas the low frequency semicircle seems to correspond to the electrode response which might overlap with the grain boundary contribution. Hence, the grain boundary resistivities could not be extracted from the AC measurements. While the impedance spectra of $Gd_{3.95}Ca_{0.05}Al_2O_{8.98}$ and $Gd_{3.95}Sr_{0.05}Al_2O_{8.98}$ were composed of three semicircles corresponding to the bulk, grain boundary and electrode response, which could be separated by fitting three R|CPE circuits to the experimental data. Examples of impedance spectra are given in Fig. 36b. The resistivities of the grain boundaries have been found to be significantly smaller than those for the bulk (especially at temperatures above 600 °C).

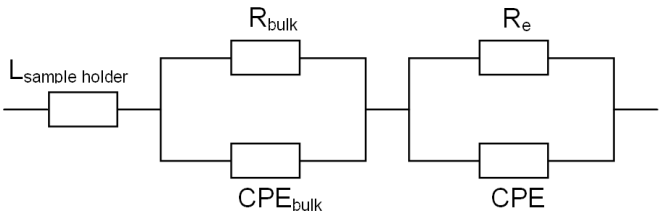

Fig. 37: Typical equivalent circuits of impedance spectra of $Gd_4Al_2O_9$. L is the inductance of sample and R_e is the resistance of electrode.

The pertinent capacitance values of $Gd_4Al_2O_9$ were almost independent of temperature (see Fig. 38) with typical values of 88.3 pF and 0.14 µF for bulk and electrode capacitance, respectively. Similarly, the capacitance values for $Gd_{3.95}Ca_{0.05}Al_2O_{8.98}$ and $Gd_{3.95}Sr_{0.05}Al_2O_{8.98}$ were also almost independent to temperature. The bulk capacitance for both compounds is about of 34 pF while the grain boundary capacitance is typically amounts in the range 0.23 – 0.35 nF.

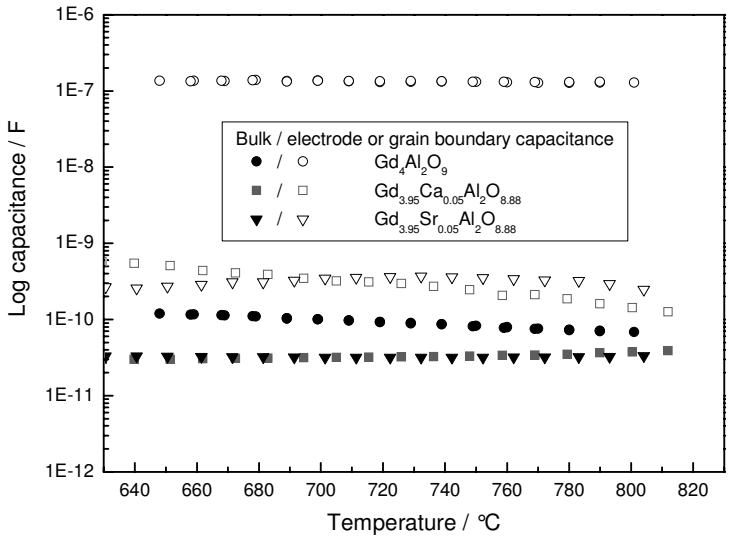

Fig. 38: The capacitance of pure $Gd_4Al_2O_9$ and $Gd_{3.95}M_{0.05}Al_2O_{8.98}$ (M=Ca,Sr).

Comparison of DC and AC conductivity measurements

The DC and AC electrical conductivity values for pure $Gd_4Al_2O_9$ shows a slight difference as indicated in Fig. 39. The DC conductivity value of pure $Gd_4Al_2O_9$ is 4.5 µS cm^{-1} at 800 °C [123] and the value of AC conductivity is 1.9 µS cm^{-1} at the same temperature. Nevertheless, despite the low conductivity both measurements yield similar conductivity values leading to satisfactory agreement. Better agreement of the DC and AC bulk conductivity results was observed for the substituted compounds $Gd_{3.95}(Ca,Sr)_{0.05}Al_2O_{8.98}$ (Fig. 39). Overall, the conductivities of $Gd_{3.95}Ca_{0.05}Al_2O_{8.98}$ and $Gd_{3.95}Sr_{0.05}Al_2O_{8.98}$ increased remarkably in comparison to the unsubstituted $Gd_4Al_2O_9$. A typical value for the AC bulk conductivity of $Gd_{3.95}Ca_{0.05}Al_2O_{8.98}$ is 86 µS cm^{-1} at 800 °C, while for the DC conductivity the value at the same temperature is 58 µS cm^{-1}. The AC data refer to bulk conductivities, which are somewhat higher than the corresponding DC values including both bulk and grain boundaries.

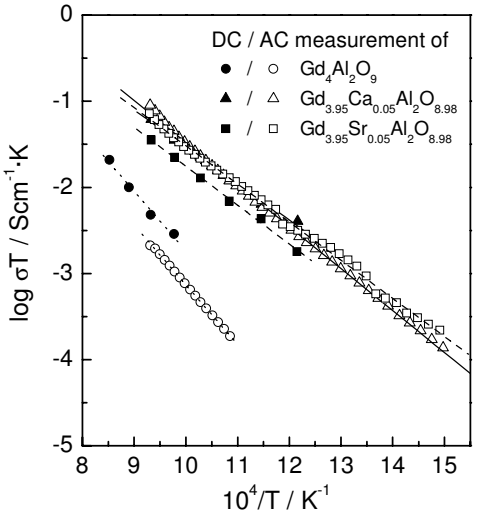

Fig. 39: Electrical conductivity of $Gd_4Al_2O_9$ and $Gd_{3.95}M_{0.05}Al_2O_9$ (M = Ca, Sr)

The activation energy calculated from the Arrhenius curves in Fig. 39 shows good agreement between both measurements (see Table 9). The activation energy for $Gd_4Al_2O_9$ is around 1.4 eV for both AC and DC measurements. For the substituted compounds, the activation energy for $Gd_{3.95}Ca_{0.05}Al_2O_{8.98}$ is 0.97 and 0.84 eV for AC and DC conductivity measurements, respectively. The activation energy of the substituted compounds decreased significantly indicating that the oxygen vacancies created in the

lattice of the substituted compounds permitted the oxygen ions to move faster as compared to the unsubstituted $Gd_4Al_2O_9$. It is interesting to note that tetravalent substitution for Al^{3+} as in $Gd_4Al_{0.8}Ge_{1.2}O_{9.6}$ [9] also results in an activation energy of 1.40 eV as for the unsubstituted $Gd_4Al_2O_9$ thus indicating that a higher energy barrier occurs for the transport of interstitial oxygen ions in the lattice.

Table 9: Electrical conductivity and activation energy, E_a, for both AC and DC measurements.

	Electrical conductivity at 800 °C / µS cm^{-1}		Activation energy, E_a / eV	
	AC	DC	AC	DC
$Gd_4Al_2O_9$	1.9	4.5	1.38	1.37
$Gd_{3.95}Ca_{0.05}Al_2O_{8.98}$	86.0	58.0	0.97	0.84
$Gd_{3.95}Sr_{0.05}Al_2O_{8.98}$	68.5	34.0	0.84	0.87

4.1.7 Thermal expansion

4.1.7.1 Dilatometry of $Gd_4Al_{2-x}Mg_xO_{9-x/2}$

The linear thermal expansion of oxy-cuspidine $Gd_4Al_2O_9$ shown in Fig. 40 was measured between 30 and 1400 °C. Above 1100 °C a shrinkage was observed during heating and an expansion observed at 900-1000 °C during cooling. This shrinkage and expansion indicates that at these temperatures the oxy-cuspidine $Gd_4Al_2O_9$ undergoes a phase transformation. The result is in good agreement with measurements reported in [103, 104]. The length difference at constant temperature in the regime of hysteresis is about 0.2 %. Table 10 shows the onset temperatures of the phase transition during heating and cooling for different compositions.

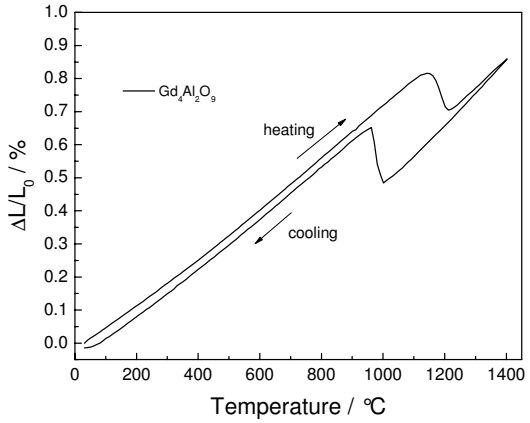

Fig. 40: Thermal expansion of $Gd_4Al_2O_9$.

The TEC values at 1000 °C are also shown in Table 10. $Gd_4Al_2O_9$ has a TEC of 7.4 x 10^{-6} K^{-1} (Fig. 42). The TEC value reported in [105] was determined by high-temperature XRD between 200 and 1400 °C. The lattice volume of $Gd_4Al_2O_9$ obtained at 1000 °C is given as 873 $Å^3$. If this volume expansion is converted to a linear TEC, a value of 6.91 x 10^{-6} K^{-1} is obtained, which is in reasonable agreement with the value measured by dilatometry.

Similarly, the thermal expansion of $Gd_4Al_{2-x}Mg_xO_{9-x/2}$ series also shows shrinkage above 1100 °C during heating and expansion during cooling in the range of 600-900 °C (see Fig. 41). The onset temperatures of the series are shown in Table 10.

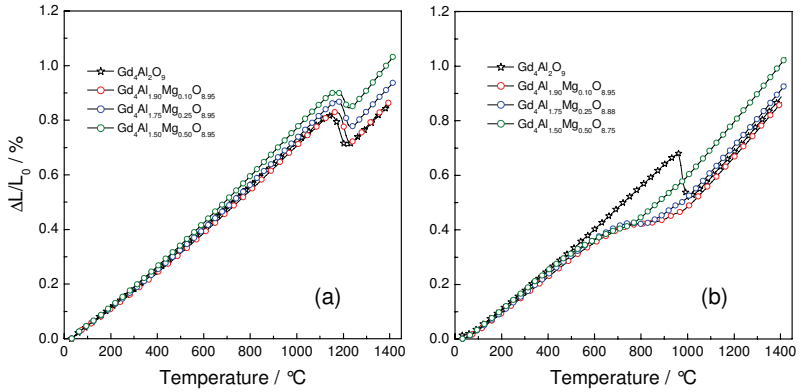

Fig. 41: Linear thermal expansion during (a) heating and (b) cooling for $Gd_4Al_{2-x}Mg_xO_{9-x/2}$ series with x=0, 0.10, 0.25 and 0.50.

The onset temperatures on cooling of the $Gd_4Al_{2-x}Mg_xO_{9-x/2}$ series also shifted significantly from the onset temperature of pure $Gd_4Al_2O_9$ and the difference in length at constant temperatures in the hysteresis regimes are about 0.5% for all samples.

Table 10: Onset temperatures of phase transition and TEC values of $Gd_4Al_{2-x}Mg_xO_{9-x/2}$.

Samples	Onset temperature (°C)		TEC at 1000 °C (x 10^{-6} K^{-1})
	Heating	Cooling	
$Gd_4Al_2O_9$	1142	1002	7.4
$Gd_4Al_2O_9$ [103]	1120	900	8.1 *
$Gd_4Al_2O_9$ [104]	1155	1068	6.5 *
$Gd_4Al_{1.90}Mg_{0.10}O_{8.95}$	1173	772	7.2
$Gd_4Al_{1.75}Mg_{0.25}O_{8.88}$	1173	802	7.6
$Gd_4Al_{1.50}Mg_{0.50}O_{8.75}$	1163	854	7.9

* derived graphically from thermal expansion curves

From the linear expansion curves, TEC of the samples were determined using Eq 13. Fig. 42 shows the TEC curves with respect to temperature.

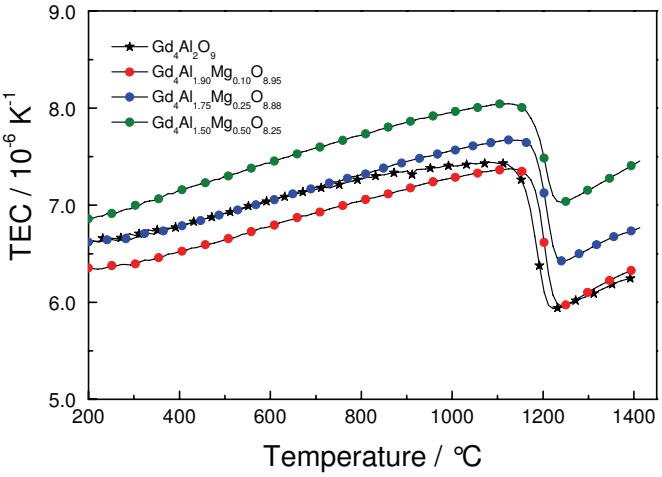

Fig. 42: TEC of $Gd_4Al_{2-x}Mg_xO_{9-x/2}$ series with x=0, 0.10, 0.25 and 0.50 mol Mg.

From Fig. 42 above, the TEC value increases linearly with increasing Mg^{2+} concentration after the onset temperature at 1102 ℃, while below the onset temperature, the TEC seems to be independent of Mg^{2+} concentration. In the series, $Gd_4Al_{1.50}Mg_{0.50}O_{8.75}$ showed the highest TEC value of 8 x 10^{-6} K^{-1} at 1110 ℃. However this value is low compared to the TEC value of 8YSZ, α = 10 x 10^{-6} K^{-1} at 900 ℃ [11]. Since the TEC values of $Gd_4Al_{2-x}Mg_xO_{9-x/2}$ series are relatively low, it also cannot be considered for other applications such as thermal barrier coatings, TBCs which require high TEC values of more than 10 x 10^{-6} K^{-1} values at temperature more than 900 ℃ [124].

4.1.7.2 Dilatometry of $Gd_{4-x}(Ca,Sr)_xAl_2O_{9-x/2}$ series.

Similar to the $Gd_4Al_{2-x}Mg_xO_{9-x/2}$ series, samples of $Gd_{4-x}(Ca,Sr)_xAl_2O_{9-x/2}$ series also showed shrinkage above 1100 ℃ during heating. Fig. 43a shows the heating curves of $Gd_{4-x}(Ca,Sr)_xAl_2O_{9-x/2}$ series. Generally, the onset of phase transition during heating were similar to $Gd_4Al_2O_9$ except the onset temperature of $Gd_{3.75}Sr_{0.25}Al_2O_{8.88}$ sample which shifted to higher temperature of about 1200 ℃ (Fig. 43). This is due to the multiphase character of the samples with high Sr^{2+} concentrations. The onset temperatures during heating for all samples are shown in Table 11.

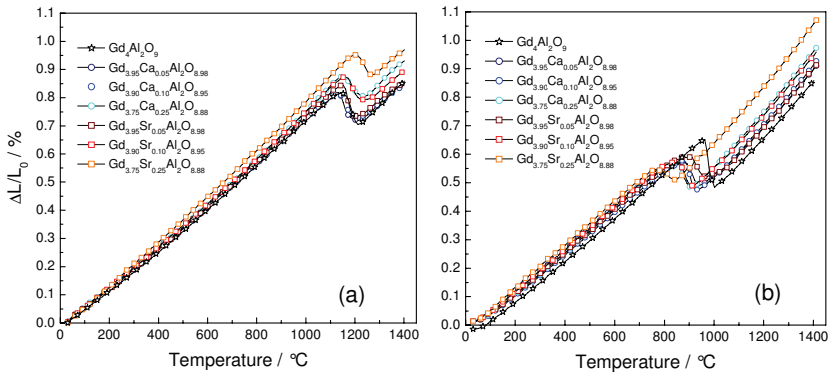

Fig. 43: Linear thermal expansion during (a) heating and (b) cooling for $Gd_{4-x}(Ca,Sr)_xAl_2O_{9-x/2}$ series with x=0, 0.05, 0.10 and 0.25.

During cooling of $Gd_{4-x}(Ca,Sr)_xAl_2O_{9-x/2}$ the expansion was observed in the range of 800 to 1000 °C (Fig. 43b). This expansion indicated the phase transition where the onset temperatures were shifted by 100 and 200 °C compared to the onset of $Gd_4Al_2O_9$ (1000 °C). This phase transition did not seem to be fully reversible leading to a very small remaining shrinkage after cooling down to room temperature.

Table 11: Onset temperatures of phase transition and TEC values of $Gd_{4-x}(Ca,Sr)_xAl_2O_{9-x/2}$ series with x=0.05, 0.10 and 0.25.

Samples	Onset temperature (°C)		TEC at 1000 °C (x 10^{-6} K^{-1})
	Heating	Cooling	
$Gd_{3.95}Ca_{0.05}Al_2O_{8.98}$	1112	942	7.5
$Gd_{3.90}Ca_{0.10}Al_2O_{8.95}$	1132	932	7.5
$Gd_{3.75}Ca_{0.25}Al_2O_{8.88}$	1142	902	7.8
$Gd_{3.95}Sr_{0.05}Al_2O_{8.98}$	1152	972	7.6
$Gd_{3.90}Sr_{0.10}Al_2O_{8.95}$	1142	912	7.8
$Gd_{3.75}Sr_{0.25}Al_2O_{8.88}$	1202	842	8.1

Comparing the TEC of $Gd_4Al_2O_9$ with Ca^{2+} and Sr^{2+} substituted $Gd_4Al_2O_9$, the values remained unchanged considering the experimental error of dilatometry (± 0.2 x 10^{-6} K^{-1}). Fig. 44 shows the TEC values of all $Gd_{4-x}(Ca,Sr)_xAl_2O_{9-x/2}$ samples in the range of 7 to 8 x 10^{-6} K^{-1} and after shrinkage at 1200 °C in between 6 to 7 x 10^{-6} K^{-1}. The TEC values at 1000 °C are shown in Table 11.

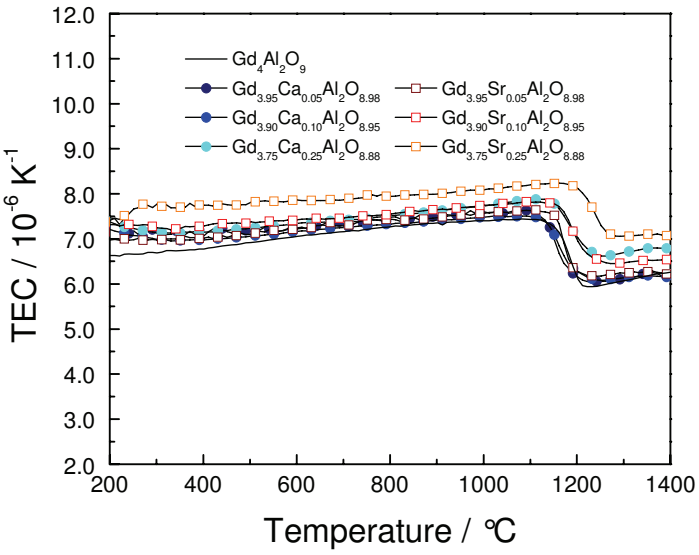

Fig. 44: TEC curves of $Gd_{4-x}(Ca,Sr)_xAl_2O_{9-x/2}$ series with x=0, 0.05, 0.10 and 0.25.

4.1.8 Summary of $Gd_4Al_2O_9$, $Gd_4Al_{2-x}Mg_xO_{9-x/2}$ and $Gd_{4-x}(Ca,Sr)_xAl_2O_{9-x/2}$

The preparation of samples via the citrate complexation route produced homogeneous powders for $Gd_4Al_2O_9$, $Gd_4Al_{2-x}Mg_xO_{9-x/2}$ and $Gd_{4-x}(Ca,Sr)_xAl_2O_{9-x/2}$ compounds. The chemical compositions of the powders were confirmed by ICP-OES techniques and the stoichiometries of all samples were in good agreement within the experimental errors of ICP-OES technique towards the nominal stoichiometry of the powders. The phase stability of the powders was investigated by DTA/TGA measurements and it can be concluded that the powders were stable from room temperatures up to 1400 °C.

The phase characterization of the powders was carried out by XRD analysis. The un-substituted $Gd_4Al_2O_9$ was obtained single phase for as-calcined (900 °C) and as-sintered (1600 °C) samples. Multiphase materials were obtained for all samples with Mg^{2+} substitutions. The additional phases were Gd_2O_3 and MgO and they increased linearly with increase in Mg^{2+} concentration. No solid solution of $Gd_4Al_2O_9$ was found for Mg. However the solid solution limit of oxy-cuspidine $Gd_4Al_2O_9$ at 1600 °C for Ca and Sr is below 0.10 and 0.05 mol/formula unit, respectively. Beyond this concentration, $CaGdAlO_4$ and $SrGd_2Al_2O_7$ were found as additional phases in the two series, respectively. The Raman spectroscopy performed for all samples confirmed the finding of XRD results. Furthermore, the Raman spectra of oxy-cuspidine $Gd_4Al_2O_9$ uniquely belonged to it and up to this work, the Raman assignments of any oxy-cuspidine types has never been reported in literature.

The microstructural analysis by SEM revealed that all sintered samples were dense with relative density of more than 95%. This finding is in good agreement with the density obtained by Archimedes method. All of the additional phases detected in XRD were supported by EDX analysis.

The electrical conductivity of $Gd_4Al_2O_9$ did not change significantly after Mg substitution. However the conductivity of $Gd_4Al_2O_9$ increased by one order of magnitude after the substitution of Ca or Sr. The highest electrical conductivity obtained by $Gd_{3.95}Ca_{0.05}Al_2O_{8.98}$ is 1.4 x 10^{-4} Scm^{-1} at 900 °C. This result is in good agreement with both the measurements of 4-probe DC conductivity and AC impedance spectroscopy. The activation energy of the Gd site substitution is lower (0.8-1.0 eV) than the Al site substitution (1.2-1.5 eV) thus indicating that the substitution on the Gd sites by Ca and Sr induced oxygen vacancies.

The thermal expansion increased linearly upon heating and cooling from room temperature to 1400 °C. A phase transition occurred in the range of 900 to 1300 °C. Phase transition also occurred for the substitution of Mg, Ca and Sr in the range of 600 to 1300 °C. The TEC value of $Gd_4Al_2O_9$ remains nearly unchanged with increasing Mg, Ca and Sr concentration which is about 6.5 to 8 x 10^{-6} K^{-1}.

4.2 Oxy-cupidine $Gd_4Ti_2O_{10}$, $Gd_4Ti_{2-x}Mg_xO_{10}$ and $Gd_{4-x}(Ca,Sr)_xTi_2O_{10}$

As mentioned in chapter 4.1, the substitution of $Gd_4Al_2O_9$ with tetravalent cations such as Ge^{4+} or Ti^{4+} [97-100], ends with $Gd_4Ti_2O_{10}$ or $Gd_4Ge_2O_{10}$ [9] crystallizing in orthorhombic structure. The mentioned approach is aimed at introducing additional oxygen so that oxygen ions are able to move within the interstitial oxygen sites. However the electrical conductivity obtained by this approach was rather low (see Fig. 17, conductivity this decade) as compared to known electrolyte materials such as stabilize zirconia [11] or ceria based materials [59]. In $Gd_4Ti_2O_{10}$ the structure contains polyatomic anion group of $[Ti_2O_8]^{8-}$ in comparison to $[Al_2O_7]^{8-}$ of $Gd_4Al_2O_9$ that can be modified by divalent cations to introduce the oxygen vacancies in the structure.

In this chapter, the similar approach of modifying oxy-cuspidine $Gd_4Al_2O_9$ was applied to the $Gd_4Ti_2O_{10}$ where divalent cations of Mg^{2+}, Ca^{2+} and Sr^{2+} were introduced in the form of $Gd_4Ti_{2-x}Mg_xO_{10}$ and $Gd_{4-x}(Ca,Sr)_xTi_2O_{10}$ compositions. Similar investigations performed on aluminates were applied to the titanates analogues.

4.2.1 Synthesis and chemical analysis

The pure compound $Gd_4Ti_2O_{10}$ and the series of $Gd_4Ti_{2-x}Mg_xO_{9-x/2}$ and $Gd_{4-x}(Ca,Sr)_xAl_2O_{9-x/2}$ were synthesized by citric complexation method as described in section 3.1.1. Chemical analysis by ICP-OES was carried out for powders calcined at 900 °C, in order to confirm the stoichiometry of the compounds. The results of chemical analysis are shown in Table 12.

Table 12: Chemical analysis of $Gd_4Ti_2O_{10}$, $Gd_4Ti_{2-x}Mg_xO_{10}$ and $Gd_{4-x}(Ca,Sr)_xTi_2O_{10-x/2}$

No	Nominal Composition	Experimental Composition
1.	$Gd_4\,Ti_2\,O_{10}$	$Gd_{4.06}\,Ti_{1.94}\,O_{10}$
2.	$Gd_{4.00}\,Ti_{1.95}\,Mg_{0.05}\,O_{9.98}$	$Gd_{3.96}\,Ti_{1.95}\,Mg_{0.09}\,O_{10-\delta}$
3.	$Gd_{4.00}\,Ti_{1.90}\,Mg_{0.10}\,O_{9.95}$	$Gd_{4.05}Ti_{1.85}\,Mg_{0.10}\,O_{10-\delta}$
4.	$Gd_{4.00}\,Ti_{1.80}\,Mg_{0.20}\,O_{9.90}$	$Gd_{4.04}Ti_{1.76}\,Mg_{0.20}\,O_{10-\delta}$
5.	$Gd_{4.00}\,Ti_{1.70}\,Mg_{0.30}\,O_{9.85}$	$Gd_{4.06}Ti_{1.65}\,Mg_{0.29}\,O_{10-\delta}$
6.	$Gd_{4.00}\,Ti_{1.60}\,Mg_{0.40}\,O_{9.80}$	$Gd_{4.01}\,Ti_{1.58}\,Mg_{0.41}\,O_{10-\delta}$
7.	$Gd_{4.00}\,Ti_{1.50}\,Mg_{0.50}\,O_{9.75}$	$Gd_{4.03}Ti_{1.50}\,Mg_{0.47}\,O_{10-\delta}$
8.	$Gd_{3.95}\,Ca_{0.05}\,Ti_2\,O_{9.98}$	$Gd_{4.05}\,Ca_{0.05}\,Ti_{1.90}\,O_{10-\delta}$
9.	$Gd_{3.90}\,Ca_{0.10}\,Ti_2\,O_{9.95}$	$Gd_{3.95}\,Ca_{0.10}Ti_{1.95}\,O_{10-\delta}$
10.	$Gd_{3.80}\,Ca_{0.20}\,Ti_2\,O_{9.90}$	$Gd_{3.83}\,Ca_{0.20}Ti_{1.96}\,O_{10-\delta}$
11.	$Gd_{3.70}\,Ca_{0.30}\,Ti_2\,O_{9.85}$	$Gd_{3.75}\,Ca_{0.29}\,Ti_{1.95}\,O_{10-\delta}$
12.	$Gd_{3.60}\,Ca_{0.40}\,Ti_2\,O_{9.80}$	$Gd_{3.66}\,Ca_{0.37}\,Ti_{1.96}\,O_{10-\delta}$
13.	$Gd_{3.95}\,Sr_{0.05}\,Ti_2\,O_{9.98}$	$Gd_{4.01}\,Sr_{0.05}\,Ti_{1.94}\,O_{10-\delta}$
14.	$Gd_{3.90}\,Sr_{0.10}\,Ti_2\,O_{9.95}$	$Gd_{3.94}\,Sr_{0.10}\,Ti_{1.96}\,O_{10-\delta}$
15.	$Gd_{3.75}\,Sr_{0.20}\,Ti_2\,O_{9.90}$	$Gd_{3.74}\,Sr_{0.23}\,Ti_{2.03}\,O_{10-\delta}$

After taking into consideration the experimental errors of ICP-OES, the stoichiometries of all synthesized powders are in good agreement with nominal stoichiometry.

4.2.2 XRD analysis

4.2.2.1 XRD results of $Gd_4Ti_2O_{10}$

$Gd_4Ti_2O_{10}$ was obtained as pure material after calcination and sintering. Fig. 45 shows the room temperature XRD of as-calcined (900 °C for 8 h) and sintered (1400 °C for 20 h) powders. Both samples crystallized in orthorhombic structure with the space group of *Pnma*. The lattice parameters were obtained by Rietveld refinements and are shown in Fig. 45.

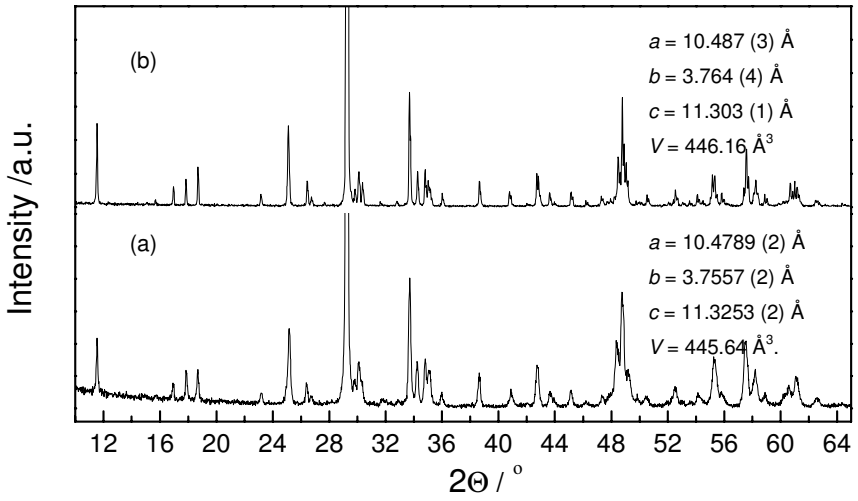

Fig. 45: Room temperature XRD results at (10 < 2Θ < 65 °) for (a) as-calcined powder and (b) sintered powder of $Gd_4Ti_2O_{10}$.

The peaks of as-calcined $Gd_4Ti_2O_{10}$ were broader than those of sintered $Gd_4Ti_2O_{10}$ indicating better crystallization of sintered $Gd_4Ti_2O_{10}$. It was also observed that the unit cell volume decreases from V=446.16 Å3 (as-calcined) to V=445.64 Å3 (sintered). Fig. 46 shows the crystal structure of oxy-cuspidine $Gd_4Ti_2O_{10}$ after structure refinement using the $Eu_4Ti_2O_{10}$ crystal structure information obtained from [125].

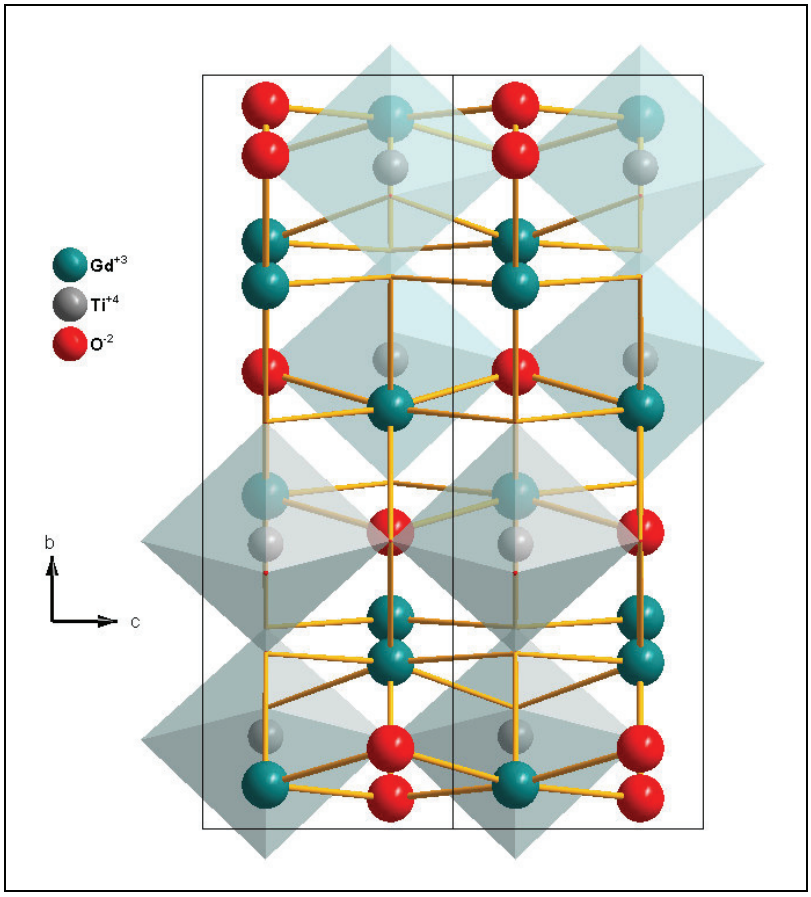

Fig. 46: The refined crystal structure of sintered $Gd_4Ti_2O_{10}$

The refined crystal structure is in good agreement as reported in [125]. From the respective structure, it is clearly observed that the formation of TiO_5 polyhedra exists in corner sharing octahedra forming the long range order of $(Ti\text{-}O\text{-}Ti\text{-}O)_n$ infinite chains.

4.2.2.2 XRD results of $Gd_4Ti_{2-x}Mg_xO_{10-x/2}$ series

The RT-XRD results obtained for $Gd_4Ti_{2-x}Mg_xO_{10-x/2}$ series shows that the main phase of orthorhombic $Gd_4Ti_2O_{10}$ was present for all sintered samples. However an additional phase of Gd_2O_3 was also present. The amount of Gd_2O_3 phase increased as Mg concentration increased. Fig. 47 below shows the RT-XRD pattern of $Gd_4Ti_{2-x}Mg_xO_{10-x/2}$ series.

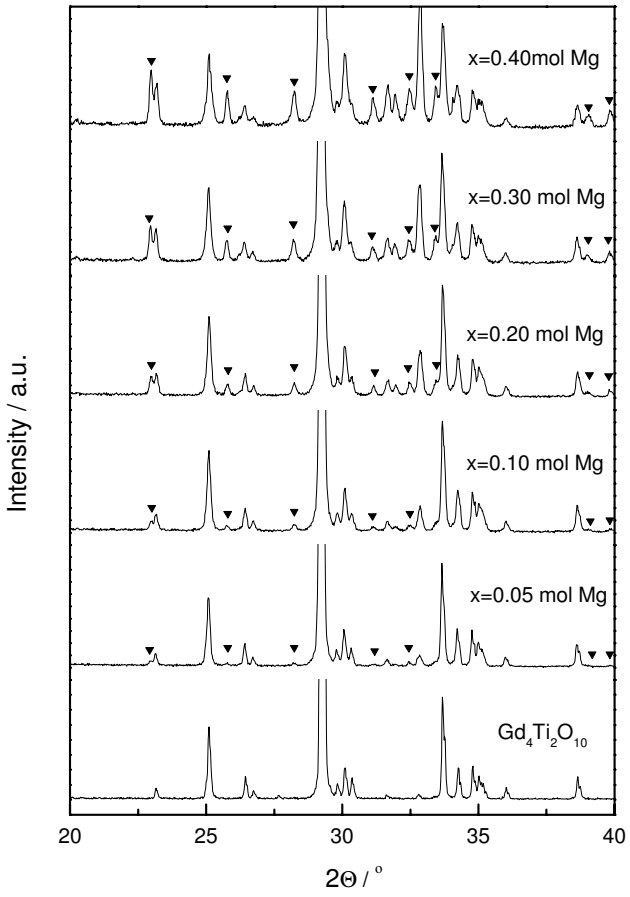

Fig. 47: Room temperature XRD patterns ($20 < 2\Theta < 40°$) of $Gd_4Ti_{2-x}Mg_xO_{10-x/2}$ series with x=0, 0.05, 0.10, 0.20, 0.30 and 0.40 after sintering at 1400 ℃ for 20 h. The un-indexed peaks belong to single phase $Gd_4Ti_2O_{10}$ and the indexed peaks are the monoclinic Gd_2O_3 [117].

The ionic radius of Ti^{4+} and Mg^{2+} at coordination number of 5 is 0.66 and 0.51 Å respectively, clearly indicating small difference in ionic radius. Thus the substitution is feasible as reported from other materials like $Sr_2Ti_{1-x}Mg_xO_{4-x/2}$ [126]. However, the substitution limit for $Sr_2Ti_{1-x}Mg_xO_{4-x/2}$ is very low of about 0.03 mol per formula unit. Similarly, from the results shown in Fig. 41, it was obvious that Mg^{2+} was not able to substitute Ti^{4+} even at very low concentration of Mg. Instead, Gd_2O_3 was formed as additional phase.

4.2.2.3 XRD results of $Gd_{4-x}(Ca,Sr)_xTi_2O_{10-x/2}$ series

The room temperature XRD results of the sintered $Gd_{4-x}Ca_xTi_2O_{10-x/2}$ series revealed single phase materials of orthorhombic $Gd_4Ti_2O_{10}$ up to 0.20 mol Ca per formula unit. Additionally $GdTiO_3$ was observed for $Gd_{3.7}Ca_{0.3}Ti_2O_{9.85}$ and $Gd_{3.6}Ca_{0.4}Ti_2O_{9.80}$. Fig. 48 shows the RT-XRD patterns of $Gd_{4-x}Ca_xTi_2O_{10-x/2}$ series. The observed amount of the additional phase is below 5 %.

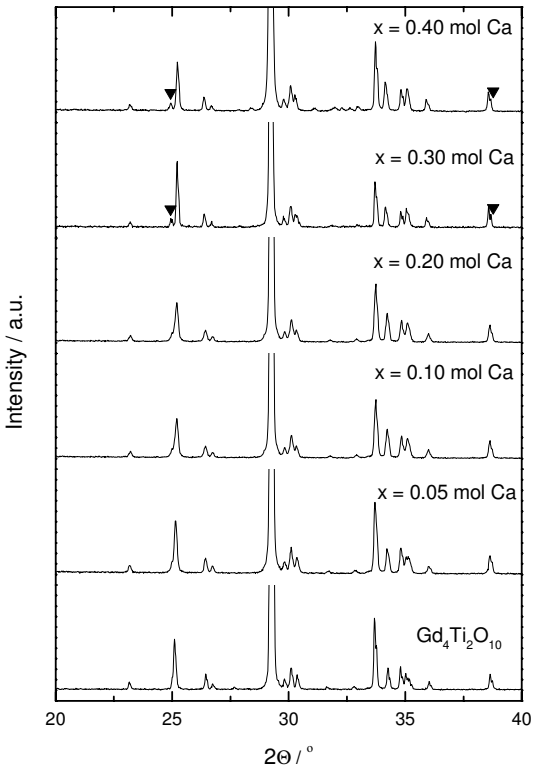

Fig. 48: Room temperature XRD patterns ($20 < 2\Theta < 40$ °) of $Gd_{4-x}Ca_xTi_2O_{10-x/2}$ series with x=0, 0.05, 0.10, 0.20, 0.30 and 0.40 after sintering at 1400 °C for 20 h. The un-indexed peaks belong to $Gd_4Ti_2O_{10}$ and the indexed peaks refer to the orthorhombic $GdTiO_3$ [117].

XRD results of $Gd_{4-x}Sr_xTi_2O_{10-x/2}$ series show that single phase materials are obtained for $Gd_{3.95}Sr_{0.05}Ti_2O_{9.98}$ and a minor additional phase of $SrTiO_3$ is detected for $Gd_{3.90}Sr_{0.10}Ti_2O_{9.95}$ sample. Fig. 49 shows the room temperature XRD patterns for the $Gd_{4-x}Sr_xTi_2O_{10-x/2}$ series.

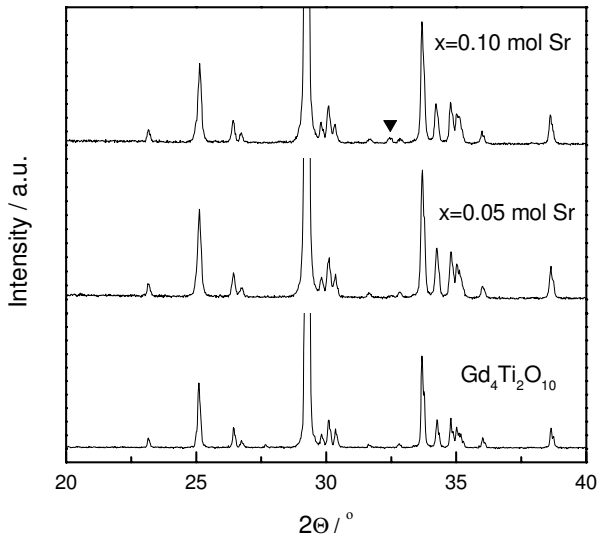

Fig. 49: Room temperature XRD patterns ($20 < 2\Theta < 40$ °) of $Gd_{4-x}Sr_xTi_2O_{10-x/2}$ series with x=0, 0.05 and 0.10 after sintering at 1400 °C for 20 h. The un-indexed peaks belong to single phase $Gd_4Ti_2O_{10}$ and the indexed peaks are due to $SrTiO_3$ [117].

The refined lattice parameters of single phase samples are shown in Table 13 below. The lattice volume does not differ significantly from each other except for the $Gd_{3.90}Sr_{0.10}Ti_2O_{9.95}$ sample where the volume is 446.14 $Å^3$. Nevertheless, the obtained lattice parameter is in good agreement with [106].

Table 13: Lattice parameter for $Gd_4Ti_2O_{10}$ and its substitutions as sintered at 1400 °C for 20 h.

Samples	a/Å	b/Å	c/Å	V/ $(Å)^3$
$Gd_4Ti_2O_{10}$	10.4789(2)	3.7557(2)	11.3253(2)	445.64
$Gd_4Ti_2O_{10}$ [106]	10.482	3.756	11.316	445.52
$Gd_4Ti_2O_{10}$ [117]	10.4788	3.7547	11.3280	445.69
$Gd_{3.90}Ca_{0.10}Ti_2O_{9.95}$	10.4846(3)	3.7585(2)	11.3049(3)	445.49
$Gd_{3.80}Ca_{0.20}Ti_2O_{9.90}$	10.4911(3)	3.7625(1)	11.2851(4)	445.45
$Gd_{3.95}Sr_{0.05}Ti_2O_{9.98}$	10.4815(3)	3.7574(1)	11.3176(3)	445.72
$Gd_{3.90}Sr_{0.10}Ti_2O_{9.95}$	10.4881(3)	3.7600(1)	11.3133(4)	446.14

4.2.3 Raman Spectroscopy

The investigation of Raman spectroscopy of $Gd_4Ti_2O_{10}$ and the series of $Gd_{4-x}(Ca,Sr)_xTi_2O_{10-x/2}$ series with x=0.05 – 0.2 was performed. From the XRD results as reported previously, the substitution limits for Ca^{2+} was in the range of 0.2 and 0.3 mol per formula unit and for Sr^{2+} was between 0.05 and 0.1 mol / formula unit. The pure $Gd_4Ti_2O_{10}$ crystallized into orthorhombic structure of $Gd_4Ti_2O_{10}$ with space group, SG=*Pnma* and with the unit cell (factor) group, UCG= D_{2h}^{16}.

Fig. 50 below shows the Raman spectra of pure $Gd_4Ti_2O_{10}$ and the series of $Gd_{4-x}(Ca,Sr)_xTi_2O_{10-x/2}$. Since it was confirmed from XRD that $Gd_4Ti_2O_{10}$ is a single phase, therefore the bands observed in this spectra uniquely belong to orthorhombic oxy-cuspidine $Gd_4Ti_2O_{10}$. The Raman spectra in the range of 100 – 900 cm^{-1} are composed of strong bands at 837, 799, 704, 660, 594, 560, 507, 461, 427, 380, 336, 260, 248, 228, 191, 176, 164, 146, 129 and 107 cm^{-1}.

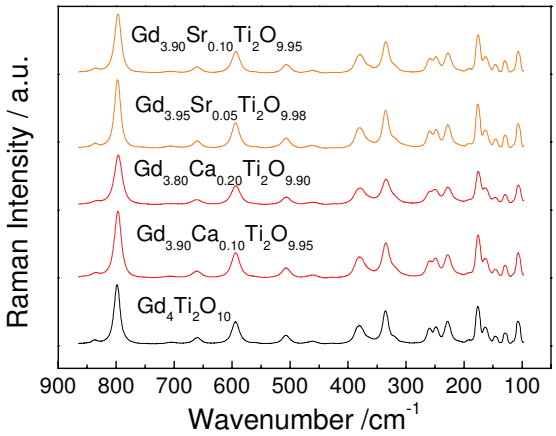

Fig. 50: The Raman spectra of $Gd_4Ti_2O_{10}$ and $Gd_{4-x}(Ca,Sr)_xTi_2O_{10-x/2}$ series sintered at 1400 °C for 20 h. Excitation: 488 nm, 2.6 mW, 50x, 10 cycles/30 seconds.

In Fig. 50 the spectrum of oxy-cuspidine $Gd_4Ti_2O_{10}$ was also observed for the Ca substituted samples. The samples of $Gd_{3.90}Ca_{0.10}Ti_2O_{9.95}$ and $Gd_{3.80}Ca_{0.20}Ti_2O_{9.90}$ were single phase; therefore all the bands observed belong uniquely to oxy-cuspidine $Gd_4Ti_2O_{10}$ structure. However, the influence of the Ca concentration was hardly observed since the spectra was almost identical with pure oxy-cuspidine $Gd_4Ti_2O_{10}$. Similar results were observed for Sr^{2+} substitution. The spectrum of oxy-cuspidine $Gd_4Ti_2O_{10}$ was also

observed for $Gd_{3.90}Sr_{0.05}Ti_2O_{9.98}$ and $Gd_{3.90}Sr_{0.10}Ti_2O_{9.95}$ samples. Interestingly these spectra were almost identical with pure oxy-cuspidine $Gd_4Ti_2O_{10}$. From the XRD results, $Gd_{3.90}Sr_{0.10}Ti_2O_{9.95}$ sample was not a single phase and a small amount of $SrTiO_3$ was detected. However, when looking at the spectra as shown in Fig. 50, no significant bands of $SrTiO_3$ were observed.

The assignment of the vibrational modes for this structure has never been reported in the literature. Therefore, it is not possible to assign which bands correspond to which vibrations without measurements in different polarizations performed on a single crystal.

4.2.4 Microstructural analysis

4.2.4.1 SEM and EDX of $Gd_4Ti_2O_{10}$

The sintered samples of oxy-cuspidine $Gd_4Ti_2O_{10}$ were cut and polished. The cross-sections of the polished samples were investigated by SEM for the microstructural analysis. In Fig. 51a, the back-scattered image of pure $Gd_4Ti_2O_{10}$ is shown. A number of darker spots were observed. With EDX analysis, it was confirmed that the matrix was oxy-cuspidine $Gd_4Ti_2O_{10}$ and the darker spots in that image were grains with an enrichment of Gd.

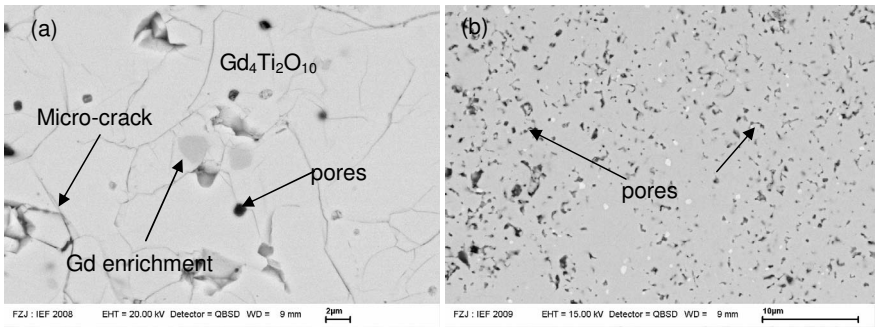

Fig. 51: The SEM (back scattered image) of $Gd_4Ti_2O_{10}$ for (a) as sintered at 1400 °C for 20 h and (b) as sintered at 1300 °C for 10h. The observed white spots were Pt from sputtering.

From that image, $Gd_4Ti_2O_{10}$ seemed to be relatively dense and this was in good agreement with the relative density of 95 % obtained by Archimedes methods. Micro-cracking was also observed in that image and it seemed that the presence of micro-cracks merely affected the relative density of the materials. The reason of this micro-crack was due to the built up of internal stress that took place during the cooling process after sintering at 1400 °C. The width of micro-cracks was in the range of 50 to 100 nm. Later $Gd_4Ti_2O_{10}$ was sintered again at lower temperature of about 1300 °C for 10 h and the results are shown in Fig. 51b. Here the micro-cracks disappeared. The disappearance of micro-cracks was due to the internal stress relaxation due to the higher number of pores. The relative density obtained by Archimedes method was about 90 %.

4.2.4.2 Microstructure of $Gd_{4-x}Ca_xTi_2O_{10-x/2}$ with x=0.10 and 0.20

Similar effects were observed for $Gd_{3.90}Ca_{0.10}Ti_2O_{9.95}$ and $Gd_{3.80}Ca_{0.20}Ti_2O_{9.90}$ samples as shown in Fig. 52a and b. Micro-cracks were observed for both samples. The main phase of both samples was confirmed by EDX analysis as $Gd_4Ti_2O_{10}$. A small number of darker spots were observed in Fig. 52a. From the EDX analysis, the darker spot was an enrichment of Gd in the $Gd_{3.90}Ca_{0.10}Ti_2O_{9.95}$ sample. Darker spots were also observed in Fig. 52b and it was due to Ca enrichment as analyzed by the EDX.

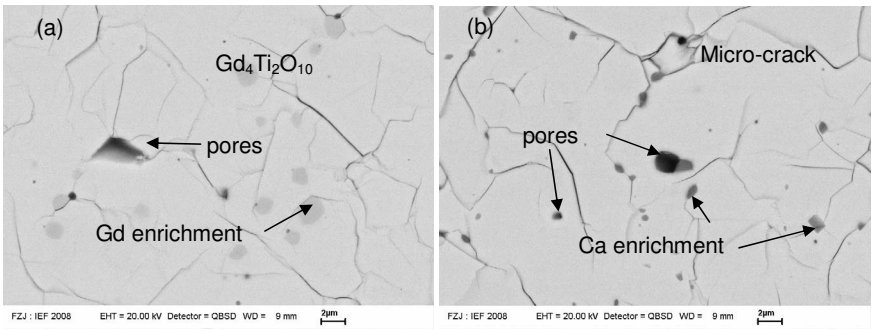

Fig. 52: SEM back-scattered images of (a) $Gd_{3.90}Ca_{0.10}Ti_2O_{9.95}$ and (b) $Gd_{3.80}Ca_{0.20}Ti_2O_{9.90}$ as sintered at 1400 °C for 10 h. The lines observed were micro-cracks.

Both compositions were samples were also sintered at lower temperature of 1300 °C for 10 h. The results are shown in Fig. 53. From Fig. 53a, the micro-cracking of $Gd_{3.90}Ca_{0.10}Ti_2O_{9.95}$ disappeared and instead pores were observed. However, the micro-cracking remained in $Gd_{3.80}Ca_{0.20}Ti_2O_{9.90}$ after sintering at 1300 °C. No sintering effect i.e. nearly no shrinkage was observed at temperature below 1300 °C for $Gd_{3.90}Ca_{0.10}Ti_2O_{9.95}$ and $Gd_{3.80}Ca_{0.20}Ti_2O_{9.90}$ samples (results not shown).

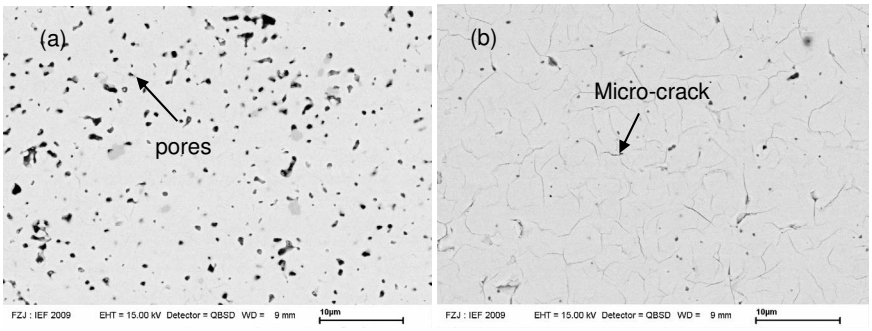

Fig. 53: SEM back-scattering images of (a) $Gd_{3.90}Ca_{0.10}Ti_2O_{9.95}$ and (b) $Gd_{3.80}Ca_{0.20}Ti_2O_{9.90}$ sintered at 1300 °C for 10 h.

4.2.5 Electrical Conductivity

The electrical conductivity measurements were performed on $Gd_4Ti_2O_{10}$, and the Mg, Ca and Sr substituted series. The 4-probes DC measurements were performed for 2 sets of samples, one sintered at 1400 ℃ / 20 h and the other at 1300 ℃ / 10 h. The results were then compared in order to understand the effect of micro-cracking on the electrical conductivity of the samples. A number of samples without micro-cracks were then selected for AC impedance spectroscopy.

4.2.5.1 4-probes DC measurements of samples sintered at 1400 ℃ for 20 h

A series of samples sintered at 1400 ℃ for 20 h were investigated for their electrical conductivity. Table 14 below shows the electrical conductivity and activation energy obtained from the measurements.

Table 14: Electrical conductivity and activation energy of $Gd_4Ti_{2-x}Mg_xO_{10-x/2}$ and $Gd_{4-x}(Ca,Sr)_xTi_2O_{10-x/2}$ series.

Samples	Electrical conductivity at 900 ℃ (Scm^{-1})	Activation energy, E_a (eV), 600 – 900 ℃
$Gd_4Ti_2O_{10}$	1.71×10^{-5}	1.15
$Gd_{4.00}Ti_{1.95}Mg_{0.05}O_{9.98}$	2.53×10^{-5}	1.01
$Gd_{4.00}Ti_{1.90}Mg_{0.10}O_{9.95}$	4.41×10^{-5}	0.96
$Gd_{4.00}Ti_{1.80}Mg_{0.20}O_{9.90}$	3.46×10^{-5}	0.95
$Gd_{4.00}Ti_{1.70}Mg_{0.30}O_{9.85}$	2.96×10^{-5}	0.99
$Gd_{4.00}Ti_{1.60}Mg_{0.40}O_{9.80}$	2.29×10^{-5}	1.25
$Gd_{4.00}Ti_{0.50}Mg_{0.50}O_{9.75}$	2.37×10^{-5}	1.10
$Gd_{3.95}Ca_{0.05}Ti_2O_{9.98}$	5.58×10^{-5}	0.92
$Gd_{3.90}Ca_{0.10}Ti_2O_{9.95}$	7.33×10^{-5}	0.80
$Gd_{3.75}Ca_{0.20}Ti_2O_{9.90}$	1.17×10^{-4}	0.91
$Gd_{3.70}Ca_{0.30}Ti_2O_{9.85}$	5.64×10^{-5}	0.92
$Gd_{3.60}Ca_{0.40}Ti_2O_{9.80}$	1.11×10^{-4}	0.90
$Gd_{3.95}Sr_{0.05}Ti_2O_{9.98}$	6.85×10^{-5}	0.91
$Gd_{3.90}Sr_{0.10}Ti_2O_{9.95}$	1.11×10^{-4}	0.94
$Gd_{3.75}Sr_{0.20}Ti_2O_{9.90}$	9.23×10^{-5}	0.94

Form table 1 above, the electrical conductivity obtained for $Gd_4Ti_2O_{10}$ at 900 ℃ was 1.71×10^{-5} Scm^{-1}. The highest electrical conductivity obtained by Mg, Ca and Sr substitutions at 900 ℃ was 4.41×10^{-5}, 1.17×10^{-4} and 1.11×10^{-4} Scm^{-1} for $Gd_{4.00}Ti_{1.90}Mg_{0.10}O_{9.95}$,

$Gd_{3.75}Ca_{0.20}Ti_2O_{9.90}$ and $Gd_{3.90}Sr_{0.10}Ti_2O_{9.95}$, respectively. From XRD result reported previously, it is known that Ca and Sr substitution below 0.2 and 0.05 mol per formula unit respectively leads to single phase materials which means that the oxygen vacancies was successfully created in the lattice. These oxygen vacancies provided an oxygen ion pathway to move in the lattice thus contributing to electrical conductivity.

The activation energy of $Gd_4Ti_{1.90}Mg_{0.10}O_{9.95}$ series was determined from the slopes of Arrhenius plot as shown in Fig. 54. Mg substitution did not significantly increase the electrical conductivity. One of the reasons was that the material was not a single phase, therefore no oxygen vacancies were created by Mg substitution, thus limiting the oxygen ion mobility.

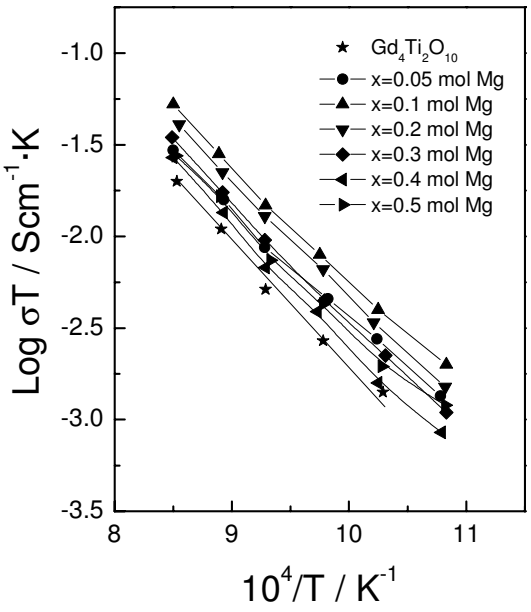

Fig. 54: Arrhenius plot of $Gd_4Ti_{2-x}Mg_xO_{10-x/2}$ with x=(0 to 0.50) as sintered at 1400 °C.

The substitution on the Gd site with Ca^{2+} and Sr^{2+} revealed better electrical conductivity results as the Mg^{2+} substitutions on Ti^{4+} sites. The electrical conductivity of $Gd_4Ti_2O_{10}$ increased about 2 orders of magnitude with Ca and Sr substitution, as shown in Fig. 55. Unfortunately, these results were doubtful due to the micro-cracking observed after sintering at 1400 °C for 20 h. These measurements were repeated for the samples sintered at 1300 °C so the micro-cracking could be avoided.

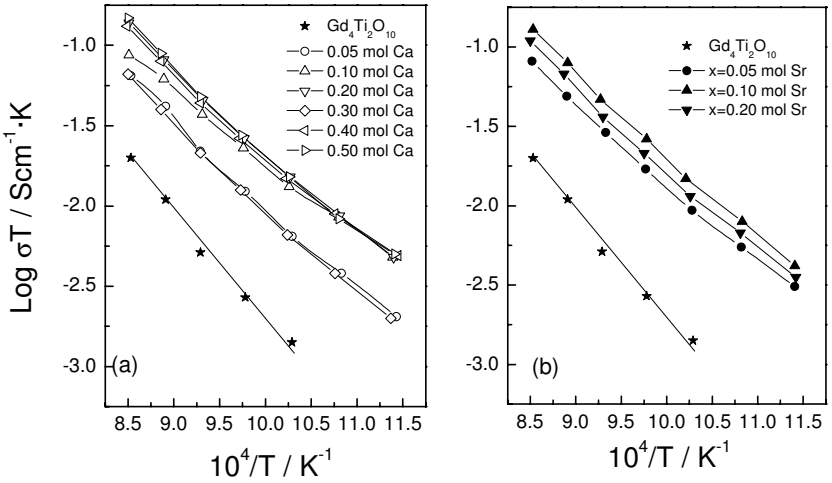

Fig. 55: The Arrhenius plot of (b) $Gd_{4-x}Ca_xTi_2O_{10-x/2}$ and (c) $Gd_{4-x}Sr_xTi_2O_{10-x/2}$ series as sintered at 1400 °C for 20 h.

4.2.5.2 4-probes DC measurements of samples sintered at 1300 °C for 10 h

The electrical conductivity results for $Gd_{4-x}(Ca,Sr)_xTi_2O_{10-x/2}$ series sintered at 1300 °C for 10 h are shown in Table 15 below.

Table 15: Effective electrical conductivity and activation energy of $Gd_{4-x}(Ca,Sr)_xTi_2O_{10-x/2}$ series as sintered at 1300 °C for 10 h.

Samples	Electrical conductivity at 900 °C (Scm^{-1})	Activation energy, E_a (eV), 650 – 900 °C
$Gd_4Ti_2O_{10}$	3.10×10^{-5}	1.35
$Gd_{3.95}Ca_{0.05}Ti_2O_{9.98}$	1.10×10^{-4}	1.05
$Gd_{3.90}Ca_{0.10}Ti_2O_{9.95}$	2.20×10^{-4}	1.16
$Gd_{3.80}Ca_{0.20}Ti_2O_{9.90}$	2.50×10^{-4}	1.06
$Gd_{3.70}Ca_{0.30}Ti_2O_{9.85}$	2.35×10^{-4}	1.11
$Gd_{3.95}Sr_{0.05}Ti_2O_{9.98}$	1.10×10^{-4}	1.11
$Gd_{3.90}Sr_{0.10}Ti_2O_{9.95}$	7.00×10^{-5}	0.90
$Gd_{3.80}Sr_{0.20}Ti_2O_{9.90}$	1.25×10^{-4}	1.25

From Table 15 above, the obtained electrical conductivity of the samples sintered at 1300 ℃ for 10 h was higher than those samples sintered at 1400 ℃ for 20 h by almost 1 order of magnitude. $Gd_{3.80}Ca_{0.20}Ti_2O_{9.90}$ revealed the highest electrical conductivity of 2.50 x 10^{-4} Scm^{-1} at 900 ℃. The activation energies obtained for these sintered samples were in the range of 0.90 to 1.35 eV. Fig. 56 below shows the Arrhenius plot of $Gd_{4-x}(Ca,Sr)_xTi_2O_{10-x/2}$ series.

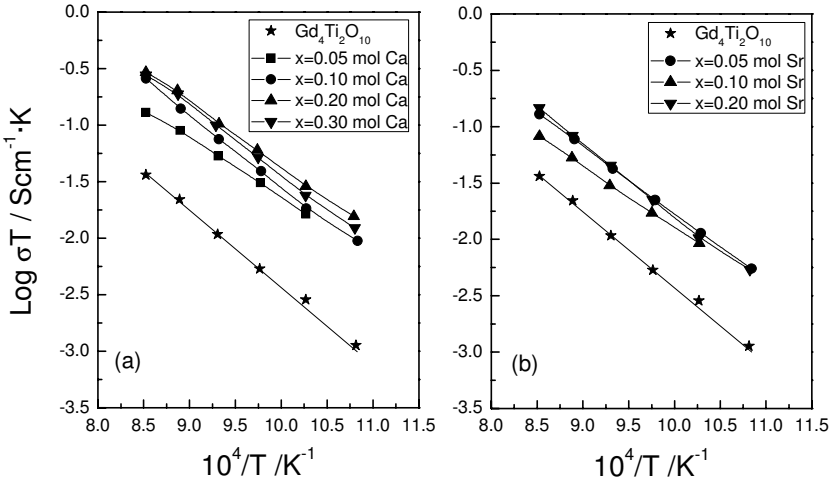

Fig. 56: The Arrhenius plot of conductivity of (a) $Gd_{4-x}Ca_xTi_2O_{10-x/2}$ and (b) $Gd_{4-x}Sr_xTi_2O_{10-x/2}$ series sintered at 1300 ℃ for 10 h.

4.2.5.3 Comparison of DC electrical conductivity

The electrical conductivity at 900 °C of all samples is compared as shown in Fig. 57. It was clearly showed that the electrical conductivity of micro-cracks sample (solid symbols) which were sintered at 1400 °C and 90% dense samples (open symbols) which were sintered at 1300 °C differed significantly. The electrical conductivity of all samples sintered at 1300 °C increased about half orders of magnitude than the sintered samples at 1400 °C. A typical effective conductivity of $Gd_4Ti_2O_{10}$ samples is 1.69 x 10^{-5} Scm^{-1} and 3.18 x 10^{-5} Scm^{-1} for as sintered samples at 1400 and 1300 °C, respectively. While for $Gd_{3.9}Ca_{0.1}Ti_2O_{9.55}$ samples the conductivity was 1.14 x 10^{-4} Scm^{-1} and 2.2 x 10^{-4} Scm^{-1} for as sintered at 1400 °C and 1300 °C, respectively. This improvement of electrical conductivity is caused by the vanishing of micro-cracks sintered at lower temperature.

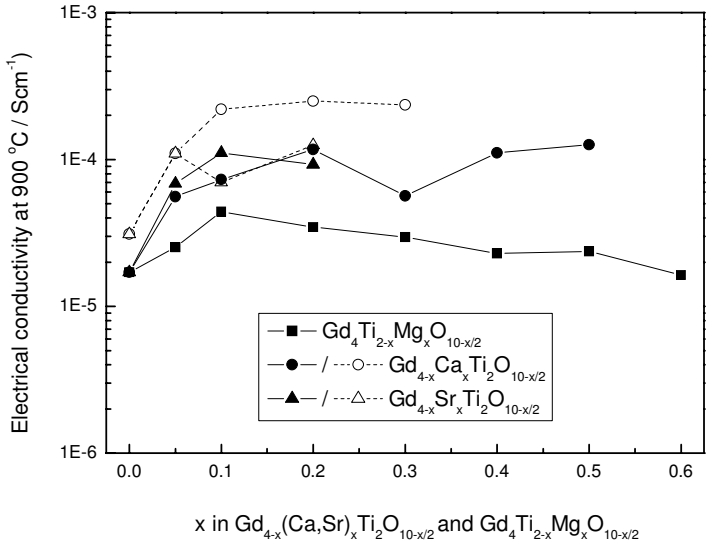

Fig. 57: The effective electrical conductivity at 900 C. The closed and open symbols are as-sintered sample of 1400 °C for 20 h and samples of 1300 °C for 10 h, respectively.

From Fig. 57, the Ca and Sr substitution showed better conductivity as compared to Mg. The reason for this result was due to the oxygen vacancies created by Ca and Sr. It was also clearly observed that the substitution limit of Ca and Sr was below 0.1 mol and 0.05 mol, respectively which also is very good agreement with XRD results mentioned previously.

4.2.5.4 AC impedance spectroscopy of $Gd_{4-x}(Ca,Sr)_xTi_2O_{10-x/2}$

A similar set up of AC impedance measurements as reported previously with oxy-cuspidine $Gd_4Al_2O_9$ was used for $Gd_4Ti_2O_{10}$ sintered at 1300 °C. The measurements revealed that impedance spectra of $Gd_4Ti_2O_{10}$ at 800 °C consisted of two semicircles in the typical complex impedance plane (see Fig. 58a). These semicircles were analyzed by fitting two components of resistance (R) and constant phase element (CPE) in a parallel circuit (R|CPE).

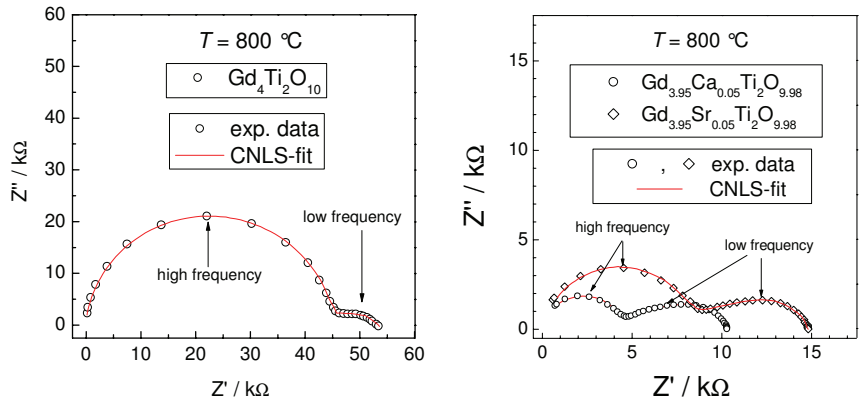

Fig. 58: Impedance spectra for (a) $Gd_4Ti_2O_{10}$ and (b) $Gd_{3.95}M_{0.05}Ti_2O_{10}$ (M=Ca, Sr). The red line is a CNLS fitting.

Looking in Fig. 58a, the high frequency semicircle can be attributed to the bulk, whereas the low frequency semicircle seemed to correspond to the electrode response which might overlap with the grain boundary contribution. Hence, the grain boundary resistivities could not be extracted from the AC measurements.

The impedance spectra of $Gd_{3.95}Ca_{0.05}Ti_2O_{9.98}$ and $Gd_{3.95}Sr_{0.05}Ti_2O_{9.98}$ were composed of three semicircles (see Fig. 58b) corresponding to the bulk, grain boundary and electrode response, which could be separated by fitting three R|CPE circuits (see Fig. 59) to the experimental data.

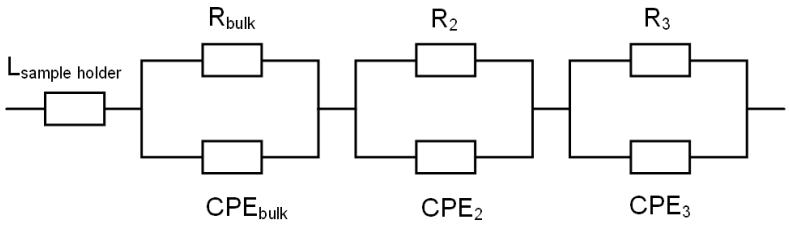

Fig. 59: Typical equivalent circuits of impedance spectra of $Gd_{3.95}M_{0.05}Ti_2O_{10}$ (M=Ca, Sr). L is the inductance of sample, R_2 and R_3 is the resistance of grain boundary and electrode, respectively.

All of the observed pertinent capacitance values were almost independent of temperature. The typical bulk capacitance values of 29.5 pF were observed for all measured samples (Fig. 60). The average electrode capacitance of $Gd_4Ti_2O_{10}$ was 59 nF while the average grain boundary (GB) capacitance was 0.18 and 0.39 µF for $Gd_{3.95}Ca_{0.05}Ti_2O_{9.98}$ and $Gd_{3.95}Sr_{0.05}Ti_2O_{9.98,}$ respectively.

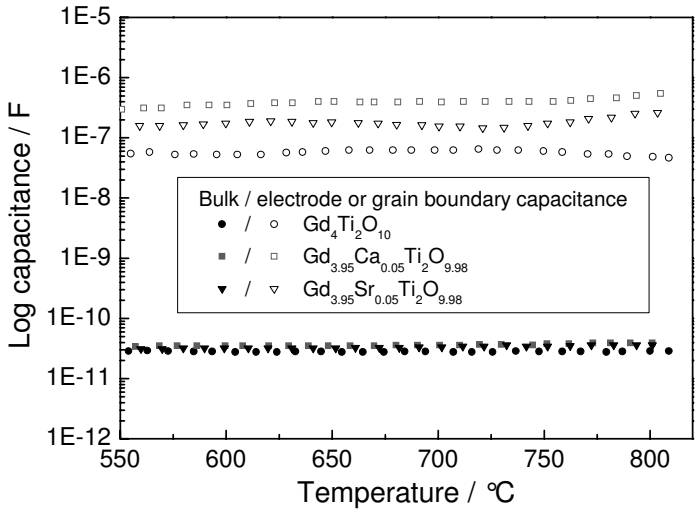

Fig. 60: The capacitance of pure $Gd_4Ti_2O_{10}$ and $Gd_{3.95}M_{0.05}Ti_2O_{9.98}$ (M=Ca,Sr).

4.2.5.5 Comparison of DC and AC conductivity measurements

The DC and AC electrical conductivity values for pure $Gd_4Ti_2O_{10}$ shows a good agreement as indicated in Fig. 61. The DC conductivity value of pure $Gd_4Ti_2O_{10}$ was 9.32 x 10^{-6} Scm^{-1} at 800 °C and the value of AC conductivity was 8.12 x 10^{-6} Scm^{-1} at the same temperature. A good agreement of DC and AC bulk conductivity was also obtained with $Gd_{3.95}Sr_{0.05}Ti_2O_{9.98}$ where the conductivity value at 800 °C was 5.31 and 3.89 x 10^{-5} Scm^{-1}, respectively. The DC and AC bulk conductivity of $Gd_{3.95}Ca_{0.05}Ti_2O_{9.98}$ at 800 °C was 5 and 12.1 x 10^{-5} Scm^{-1}, respectively. However, the magnitude of conductivity obtained by both measurements was rather low which was 10^{-5} Scm^{-1} that yielded similar conductivity values leading to satisfactory agreement.

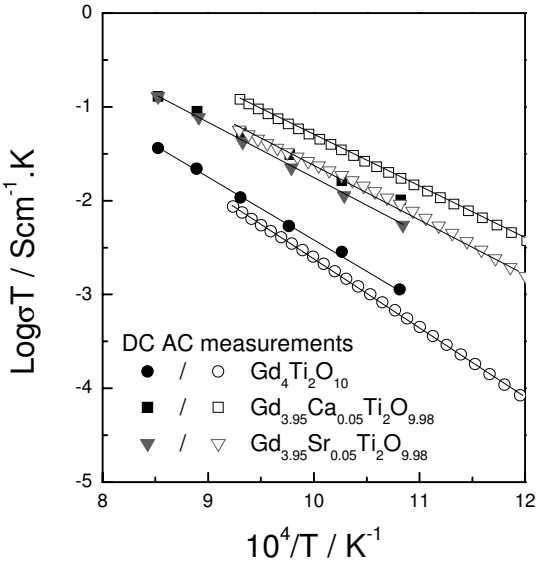

Fig. 61: Effective electrical conductivity of $Gd_4Ti_2O_{10}$ and $Gd_{3.95}M_{0.05}Ti_2O_{10}$ (M = Ca, Sr)

Overall, both measurements show that the conductivities of $Gd_{3.95}Ca_{0.05}Ti_2O_{9.98}$ and $Gd_{3.95}Sr_{0.05}Ti_2O_{9.98}$ increased considerably in comparison to the unsubstituted $Gd_4Ti_2O_{10}$ (see Fig. 61). The activation energy calculated from the Arrhenius curves in Fig. 4 shows good agreement between both measurements (see Table 16). The activation energy for $Gd_4Ti_2O_{10}$ is 1.35 and 1.45 eV for DC and AC measurements, respectively. For the substituted compounds, the activation energy for $Gd_{3.95}Ca_{0.05}Ti_2O_{9.98}$ was 1.05 and 1.20 eV for AC and DC conductivity measurements, respectively. The activation energy of the substituted compounds decreased significantly indicating that the oxygen vacancies

created in the lattice of the substituted compounds permitted the oxygen ions to move faster as compared to the unsubstituted $Gd_4Ti_2O_{10}$. Since no oxygen vacancies were created with oxy-cuspidine $Gd_4Ti_2O_{10}$, the oxygen ions had to move via the oxygen interstitial site that led to high activation energy which was similar to the pseudo orthorhombic $Gd_4Al_{0.8}Ge_{1.2}O_{9.6}$ (1.4 eV) [9] and orthorhombic $La_4Ti_2O_{10}$ (1.6 eV [98] and 1.51 eV [127]). Both reported oxy-cuspidine compounds are known to have no oxygen vacancies.

Table 16: Electrical conductivity and activation energy, *Ea* for both AC and DC measurements.

	Electrical conductivity at 800 °C / Scm^{-1}		Activation energy, E_a / eV	
	DC	AC	DC(550-800°C)	AC (650-900 °C)
$Gd_4Ti_2O_{10}$	9.32×10^{-6}	8.12×10^{-6}	1.35	1.45
$Gd_{3.95}Ca_{0.05}Ti_2O_{9.98}$	5.00×10^{-5}	1.21×10^{-4}	1.05	1.20
$Gd_{3.95}Sr_{0.05}Ti_2O_{9.98}$	5.31×10^{-5}	3.89×10^{-5}	1.11	1.13

4.2.6 Thermal expansion

The reported work regarding thermal expansion of $Gd_4Ti_2O_{10}$ or $RE_4Ti_2O_{10}$ is very limited. However recently, few researches have been interested in using $RE_4Ti_2O_{10}$ as part of nuclear application [106, 128, 129]. Interestingly, they used high temperature XRD measurements to study the $RE_4Ti_2O_{10}$ expansions behavior. In this work, the high temperature XRD was investigated and compared with the dilatometry measurements. The results are discussed accordingly.

4.2.6.1 Thermal expansion of $Gd_4Ti_2O_{10}$ with high temperature XRD

The as-sintered (1400 °C for 20) $Gd_4Ti_2O_{10}$ pellet was powdered before the high temperature XRD measurements. Fig. 62 below shows the high temperature XRD result of $Gd_4Ti_2O_{10}$ stacked in temperature (25 → 1000 → 25 °C).

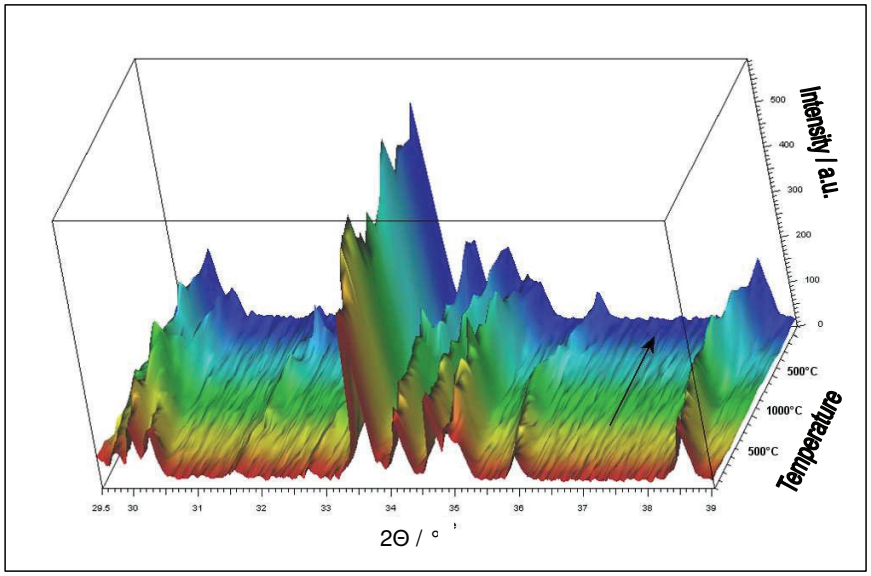

Fig. 62: High temperature XRD results (20 < 2Θ < 40 °) of $Gd_4Ti_2O_{10}$ stacked in temperature.

Obviously, the intensity of the main peaks changed as temperature changed, indicating that the occupancy of atomic positions was slightly changed during heating and cooling. However, no phase transition was observed. The change of peak position was also observed during heating and cooling due to the lattice expansion and shrinkage. The changes of the lattice constants are shown in Fig. 63.

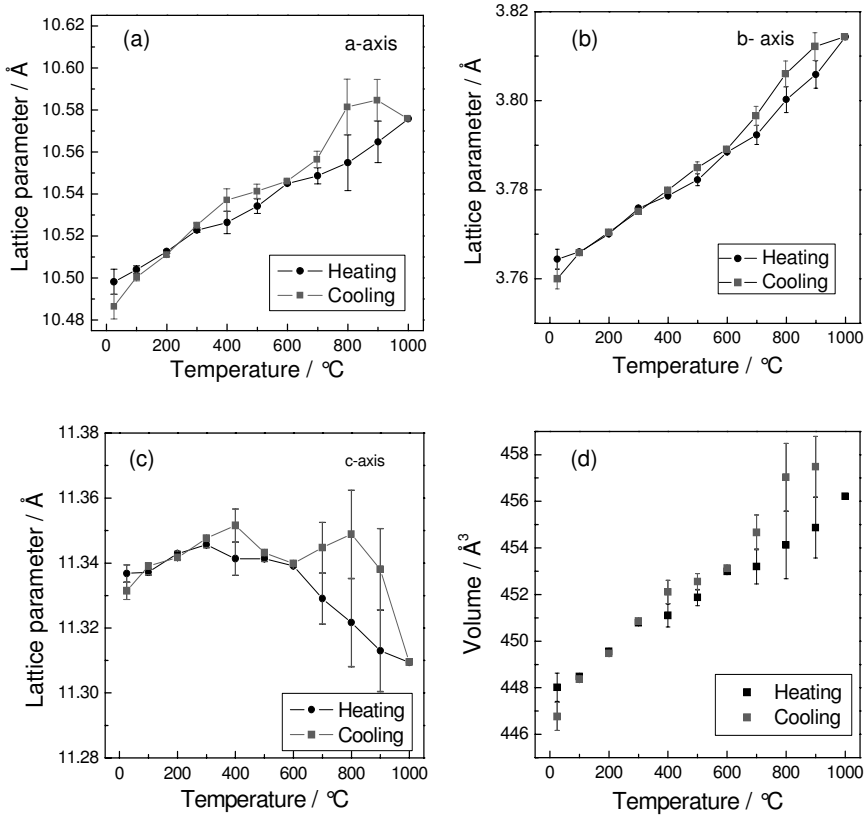

Fig. 63: The lattice parameters and cell volume of $Gd_4Ti_2O_{10}$ powder sintered at 1400 ℃ for 20 h during heating and cooling cycle.

Lattice parameters on *a* and *b* increased as the temperature increased. However, the difference of lattice parameter values during heating and cooling were mainly because of the experimental limitation of the device. However the trends of the lattices changes were satisfactory in term of temperature dependent by average error between maximum and minimum values. In general, we can conclude that both lattice increased and decreased progressively upon heating and cooling.

The lattice parameter on *c* a remained constant until 600 ℃ then decreased until 1000 ℃. Similar values were obtained during cooling after considering the average errors. In general, the lattice parameter *c* differed strongly as compared to those reported in [106,

128]. The cell volume of $Gd_4Ti_2O_{10}$ shown in Fig. 63d increased linearly upon heating. The lattice parameters plotted in Fig. 63 is shown in Table 17.

The linear thermal expansion (%TE) and its coefficient (TEC) of $Gd_4Ti_2O_{10}$ from HT-XRD were obtained by equations below;

$$\%TE = \left(\frac{a_T - a_{298}}{a_{298}} \right) \times 100 \qquad \text{Eq. 19}$$

and

$$TEC = \left(\frac{1}{a_{298}} \right) \times \left(\frac{a_T - a_{298}}{T - 298} \right) \qquad \text{Eq. 20}$$

Where a_T is a lattice parameter at temperature T, and a_{298} is the respective value at 298 K. The calculated values are then also shown in Table 17.

Table 17: The lattice parameters, percentage thermal expansion and linear thermal expansion coefficient of $Gd_4Ti_2O_{10}$ obtained from high temperature XRD.

T (K)	Lattice parameter (Å)				Thermal expansion (%)				TEC (10^{-6} K^{-1})				
	a	b	c	V	a	b	c	V	α_a	α_b	α_c	α_V	$\bar{\alpha}$
298	10.4981	3.7644	11.3367	448.02	0.00	0.00	0.00	0.00	-	-	-	-	-
373	10.5040	3.7660	11.3372	448.48	0.06	0.04	0.00	0.10	7.49	5.67	0.59	13.75	4.58
473	10.5125	3.7701	11.3429	449.56	0.14	0.15	0.05	0.34	7.84	8.65	3.13	19.62	6.54
573	10.5228	3.7758	11.3456	450.78	0.24	0.30	0.08	0.62	8.56	11.01	2.85	22.42	7.47
673	10.5264	3.7786	11.3413	451.10	0.27	0.38	0.04	0.69	7.19	10.06	1.08	18.33	6.11
773	10.5342	3.7822	11.3413	451.87	0.34	0.47	0.04	0.86	7.24	9.95	0.85	18.05	6.02
873	10.5449	3.7885	11.3391	452.99	0.45	0.64	0.02	1.11	7.75	11.13	0.37	19.26	6.42
973	10.5486	3.7923	11.3290	453.20	0.48	0.74	-0.07	1.16	7.13	10.98	-1.01	17.10	5.70
1073	10.5548	3.8002	11.3216	454.11	0.54	0.95	-0.13	1.36	6.97	12.27	-1.72	17.52	5.84
1173	10.5647	3.8059	11.3129	454.87	0.63	1.10	-0.21	1.53	7.25	12.60	-2.40	17.45	5.82
1273	10.5758	3.8143	11.3094	456.21	0.74	1.33	-0.24	1.83	7.59	13.60	-2.47	18.72	6.24

The calculated values of %TE and TEC (α) then are displayed in charts as shown in Fig. 64a and b, respectively. The thermal expansions of $Gd_4Ti_2O_{10}$ on *c* was in negative expansion which again, strongly differed from [106, 128]. The reason for this result is explained in the next section. However, the average TEC of $Gd_4Ti_2O_{10}$, $\overline{\alpha}$ was 6.1 (±0.2) x 10^{-6} K^{-1} which is in satisfactory agreement with TECs reported in [106, 128].

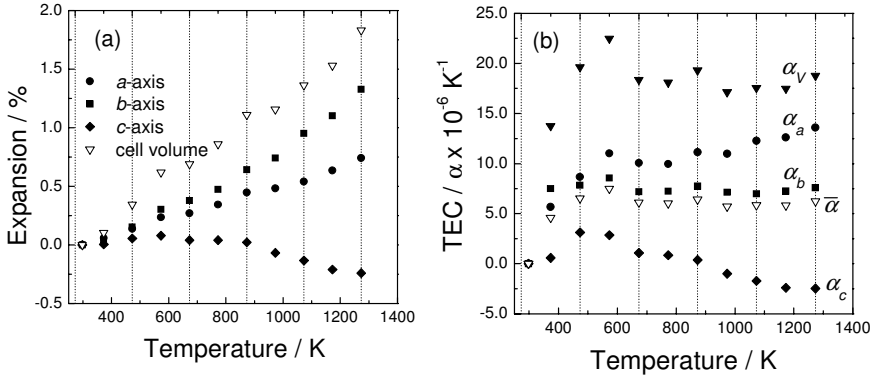

Fig. 64: (a) The percentage thermal expansion of $Gd_4Ti_2O_{10}$ along the *a*, *b* and *c* axes during heating as well as volume expansion, (b) shows the TEC values of $Gd_4Ti_2O_{10}$.

4.2.6.2 Dilatometry of $Gd_{4-x}(Ca,Sr)_xTi_2O_{10-x/2}$ series

Fig. 65 below shows the result of heating and cooling curves for un-substituted $Gd_4Ti_2O_{10}$, $Gd_{4-x}Ca_xTi_2O_{10-x/2}$ (x=0.10 and 0.20) and $Gd_{4-x}Sr_xTi_2O_{10-x/2}$ (x=0.05 and 0.10) which were sintered at 1400 °C for 20 h. Looking at Fig. 65a, the expansion of $Gd_4Ti_2O_{10}$ was constant in the range of 600 to 1000 °C and then linearly expanded beyond this temperature. Similar behavior was observed for $Gd_{3.95}Sr_{0.05}Ti_2O_{9.98}$ and $Gd_{3.90}Sr_{0.10}Ti_2O_{9.95}$ samples. However, unusual behavior was observed for $Gd_{3.90}Ca_{0.10}Ti_2O_{9.95}$ and $Gd_{3.90}Ca_{0.20}Ti_2O_{9.90}$ samples which showed almost no expansion below 900 °C and then linearly expanded at higher temperature.

Fig. 65b, shows the cooling curves of the same materials. $Gd_4Ti_2O_{10}$ shrank linearly from 1400 to 800 °C and then expanded again until room temperature. Similar shrinkage was observed for Ca and Sr substituted samples but the expansion points began at 650 °C.

This unusual behavior was also observed in high temperature XRD measurement of $Gd_4Ti_2O_{10}$ previously. The unusual expansion was clearly observed on *c*, where it shows a negative expansion (see Fig. 64a). This crystallographic negative expansion as observed in high temperature XRD can explain the unusual expansion as measured by dilatometry.

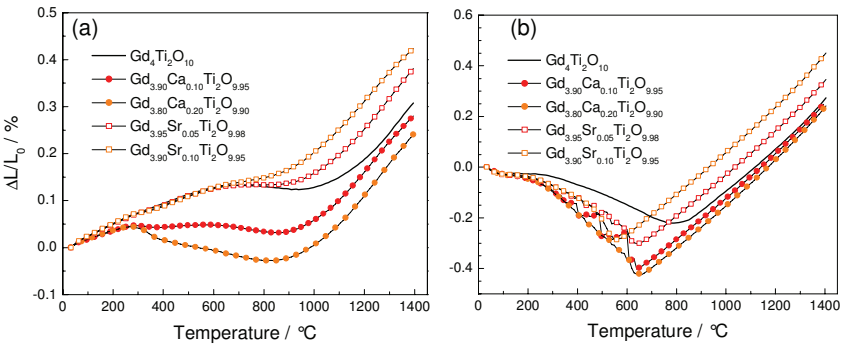

Fig. 65: Expansion and shrinkage during (a) heating and (b) cooling of samples sintered at 1400 °C for 20 h.

From microstructure investigations, all samples sintered at 1400 °C showed micro-craking effects. At this point, it was pre-concluded that the unusual expansion behaviors were due to the micro-cracking effects after several samples sintered at 1300 °C were free form micro-cracking.

The dilatometric measurements were repeated with the samples sintered at 1300 °C. The thermal expansion of $Gd_4Ti_2O_{10}$ expanded linearly up to 1100 °C as shown in Fig. 66a. Similar behavior was observed for $Gd_{3.95}Ca_{0.05}Ti_2O_{9.98}$ and $Gd_{3.95}Sr_{0.05}Ti_2O_{9.98}$ samples. However, $Gd_{3.95}Ca_{0.10}Ti_2O_{9.95}$ showed a slight shift of linear curve at 600 °C. Overall, the unusual expansion due to the micro-cracking disappeared instantly and confirmed the pre-conclusion made previously. Also, the cooling curves did not show any unusual temperature dependence.

It was clear that the micro-cracking effects were retarding the material expansions during heating cycle. Before the materials began to expand linearly (between 700 to 1100 °C), the initial thermal expansions were closing off the gaps between the micro-cracks until these open spaces came together at certain temperature (after 1100 °C).

The TECs of the samples remained almost constant from 200 to 1000 °C. The TEC for $Gd_4Ti_2O_{10}$ was about 7.6 x 10^{-6} K^{-1} while TEC for $Gd_{3.95}Ca_{0.05}Ti_2O_{9.98}$ and $Gd_{3.95}Sr_{0.05}Ti_2O_{9.98}$ was about 6.6 and 7.2 x 10^{-6} K^{-1}. The TEC value of $Gd_{3.90}Ca_{0.10}Ti_2O_{9.95}$ slightly fluctuated with an average of 6.7 x 10^{-6} K^{-1}.

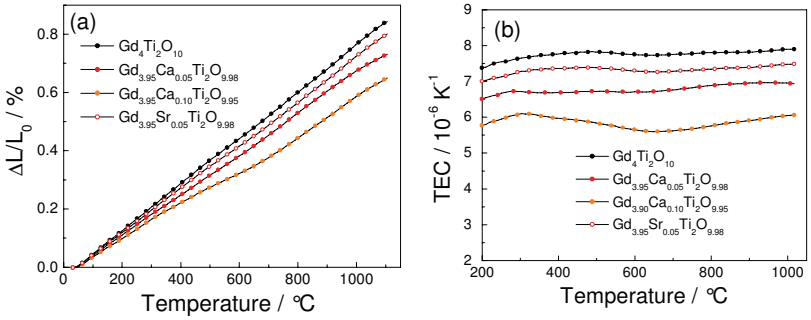

Fig. 66: (a) Linear expansion and (b) TEC curves vs temperature of samples sintered at 1300 °C for 10 h.

4.2.6.3 Comparison of TECs between high temperature XRD and dilatometer

The comparisons of the TECs values between both measurements are shown in Fig. 67. A satisfactory agreement of TEC values was obtained between $Eu_4Ti_2O_{10}$ [128], $(Gd,Dy)_4Ti_2O_{10}$ [106] and $Gd_4Ti_2O_{10}$ [this work] as measured by high temperature XRD. The values are shown in Table 18.

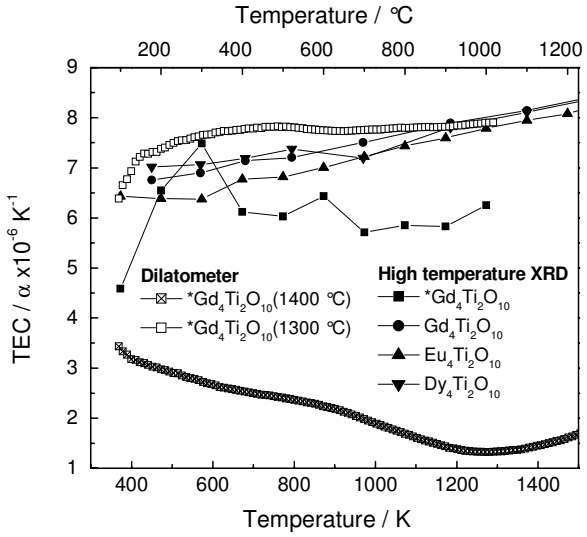

Fig. 67: TECs (α) curves of materials as measured by high temperature XRD (closed symbols) and dilatometer (open symbols – sintered bars). $*Gd_4Ti_2O_{10}$ is this work, $Eu_4Ti_2O_{10}$ [128] and $(Gd,Dy)_4Ti_2O_{10}$ [106].

Dilatometer TEC value of $Gd_4Ti_2O_{10}$ as sintered at 1300 °C is in a very good agreement with the TECs of high temperature XRD reported in [106, 128]. However, a significant difference of TECs value was observed between high temperature XRD and dilatometer of $Gd_4Ti_2O_{10,}$ respectively. The reason for this difference is because that the powder of $Gd_4Ti_2O_{10}$ was sintered at 1400 °C and the bar of $Gd_4Ti_2O_{10}$ for dilatometer was sintered at 1300 °C. While the bar of $Gd_4Ti_2O_{10}$ as sintered at 1400 °C that have micro-cracking effects shows unusual and low TEC values. TEC values at 1000 °C were almost similar accept for the micro-cracking sample. The $\alpha_{1000\ °C}$ values are shown in Table 18 below.

Table 18: The average TECs ($\overline{\alpha}$) and TECs (α) at 1000 °C.

Samples	Average TEC ($\overline{\alpha}$ x 10^{-6} K^{-1})	TEC at 1000 °C α x10^{-6} K^{-1}
**$Gd_4Ti_2O_{10}$ (1400 °C)	2.13	1.32
**$Gd_4Ti_2O_{10}$ (1300 °C)	7.36	7.90
$Gd_4Ti_2O_{10}$ [this work]	6.09	6.26
$Gd_4Ti_2O_{10}$ [106]	6.67	7.99
$Eu_4Ti_2O_{10}$ [128]	6.73	7.78
$Dy_4Ti_2O_{10}$ [106]	6.69	7.92

** - sintered bars with dilatometric measurements.

4.2.7 Summary of oxy-cuspidines $Gd_4Ti_2O_{10}$, $Gd_4Ti_{2-x}Mg_xO_{10}$ and $Gd_{4-x}(Ca,Sr)_xTi_2O_{10}$

The synthesis of oxy-cuspidine $Gd_4Ti_2O_{10}$, $Gd_4Ti_{2-x}Mg_xO_{10}$ and $Gd_{4-x}(Ca,Sr)_xTi_2O_{10}$ was successfully prepared by citric complexation method. Chemical analysis confirmed all of the synthesized powders are in good agreement with nominal stoichiometries.

Single phase materials were obtained for the un-substituted $Gd_4Ti_2O_{10}$. No single phase material was obtained for $Gd_4Ti_{2-x}Mg_xO_{10}$ series. An additional phase of Gd_2O_3 was present, thus no solid solution was observed for Mg substituting for Ti sites. However, single phase materials were obtained for $Gd_{4-x}(Ca,Sr)_xTi_2O_{10}$. The substitution limit for $Gd_{4-x}Ca_xTi_2O_{10}$ and $Gd_{4-x}Sr_xTi_2O_{10}$ were below 0.30 and 0.10 mol for Ca and Sr, respectively. Additional phases of $GdTiO_3$ and $SrTiO_3$ in each series were present beyond the substitution limits, respectively.

Microstructural analysis revealed micro-crack formation for the sintered samples at 1400 °C for 20 h. The micro-cracks mostly occurred along the grain and grain boundaries and had a width of about 1-2nm. Absence of micro-cracks was observed for the samples sintered at 1300 °C for 10 h. Small amount of pores were observed. However the relative density was about 90%. Raman spectrum of oxy-cuspidine $Gd_4Ti_2O_{10}$ was obtained for the first time. The Ca and Sr substituted samples showed almost identical spectra as that of $Gd_4Ti_2O_{10}$. No significant band could be assigned to the additional phases.

The electrical conductivity of all samples is summarized in the Fig. 57. A significant increase was observed for the samples sintered at 1300 °C for 10 h. $Gd_{3.80}Ca_{0.20}Ti_2O_{9.90}$ gave the highest electrical conductivity of 2.50 x 10^{-4} Scm^{-1} at 900 °C.

The unusual thermal expansion of the samples sintered at 1400 °C for 20 h was due to micro-crack formation. The unusual expansion disappeared for the samples sintered at 1300 °C for 10 h. The highest dilatometric TEC for these samples had $Gd_4Ti_2O_{10}$ with α = 7.5 (±0.2) x 10^{-6} K^{-1}. The expansion of $Gd_4Ti_2O_{10}$ as sintered at 1400 °C for 20 h then measured by HT-XRD revealed a linear expansion and the α = 6.1 (±0.2) x 10^{-6} K^{-1}.

4.3 SnP_2O_7 and $Sn_{1-x}Fe_xP_2O_{7-x/2}$

The electrical conductivity of oxy-cuspidine $Gd_4Al_2O_9$ and $Gd_4Ti_2O_{10}$ increased 1 order of magnitude with substitution of Ca and Sr. However, despite this increase the value of conductivity was still relatively low for an application as ionic conductor in SOFC. The investigated oxy-cuspidine structure revealed that the number of oxygen vacancies introduced in the structure was rather small, thus limiting the oxygen ion mobility [106]. Therefore a different type of material was investigated, a pyrophosphate based on SnP_2O_7 with polyatomic anions of $[P_2O_7]^{4-}$ were modified with trivalent cations such as In [10] [10] and Sc [113] to introduced oxygen vacancies in the lattice.

The electrical conductivity of SnP_2O_7 and In-substituted compositions showed significant conductivity of 1-2 x 10^{-1} Scm^{-1} [109] in the range of 150 to 300 °C. However, the conductivity at high temperature (600 – 900 °C) was low, about 0.1-7.0 x 10^{-6} Scm^{-1} [10, 113]. Similar results were obtained for $Sn_{1-x}Sc_xP_2O_{7-x/2}$ [10, 113]. Comparing the ionic radius of Sn^{4+} (0.69 Å) with In^{3+} (0.80 Å) and Sc^{3+} (0.74 Å) of coordination number (CN) = 6, both candidates were ideal with a difference in ionic radius of about 20 %. Another candidate, Fe^{3+} with ionic radius of 0.65 Å of CN = 6 showed smaller difference as compared to the reported candidates [116].

Based on the ionic radius comparison, a series of $Sn_{1-x}Fe_xP_2O_{7-x/2}$ was synthesized via solid state reaction to evaluate the electrical conductivity with 4-probes DC conductivity measurements.

4.3.1 Synthesis of SnP_2O_7 and $Sn_{1-x}Fe_xP_2O_{7-x/2}$

The series $Sn_{1-x}Fe_xP_2O_{7-x/2}$ was synthesized via solid state reaction. The starting materials were SnO_2, $NH_4H_2PO_4$ and Fe_2O_3. The detailed synthesis process is described in the experimental section. The heated mixture of the series at 400 °C for 2 h showed sintered-like appearance and the mixture was very hard but porous. This mixture was crushed, grinded and pre-calcined and then calcined at 650 °C for 2 h and 900 °C for 8 h, respectively. White powders were obtained for all samples. The powders were sintered at 1250 °C for 8 h after pressing into bars.

The sintered bars are shown in Fig. 68. They appeared to be cracked and bloated. The color of the sintered bars was totally differed as compared to the $Sn_{1-x}In_xP_2O_{7-x/2}$ series which were white in color [10]. Furthermore, the bars were also brittle and difficult to

handle. From these results, the sintering temperature at 1250 °C was already too high indicating that the materials were over sintered.

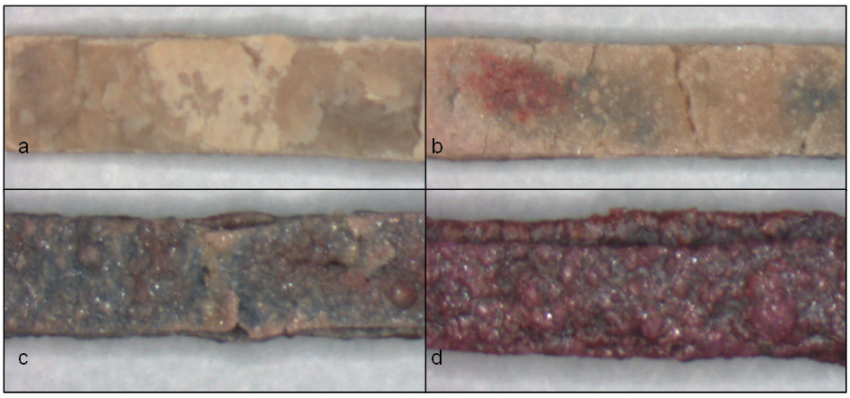

Fig. 68: The sintered bars of $Sn_{1-x}Fe_xP_2O_{7-x/2}$ with (a) 0.05, (b) 0.10, (c) 0.20 and (d) 0.30 mol Fe per formula unit.

From Fig. 68, the gradual change of color from cream to reddish corresponds to the increase of Fe concentration. The change of morphology from cracked to bloated was also observed with increasing in Fe concentration. Due to this result, the calcined powders were investigated by DTA / TG in order to understand the reaction that had taken place during sintering of the bars. Phase analysis of as-calcined and sintered powders was carried out by XRD.

4.3.2 DTA/TGA of $Sn_{1-x}Fe_xP_2O_{7-x/2}$

The DTA/TGA measurements were performed in the range of 25 – 1400 °C without holding time. The heating rate used for these measurements was 5 K / min. Fig. 69 shows the DTA/TGA results of $Sn_{0.95}Fe_{0.05}P_2O_7$ and $Sn_{0.90}Fe_{0.10}P_2O_7$.

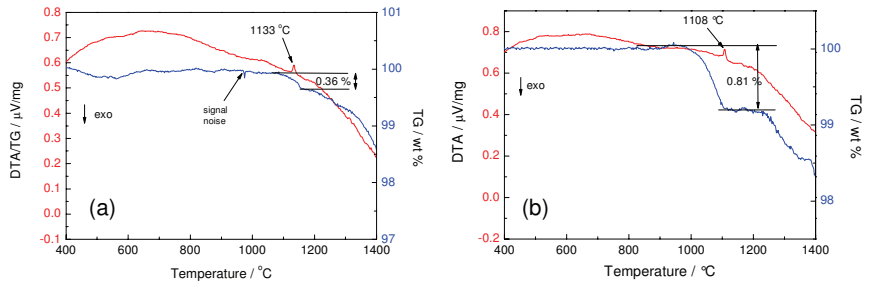

Fig. 69: DTA/TGA for (a) $Sn_{0.95}Fe_{0.05}P_2O_7$ and (b) $Sn_{0.90}Fe_{0.10}P_2O_7$ for as-calcined powders at 900 °C for 8 h.

An endothermic reaction was observed at 1133 °C accompanied with weight loss of about 0.36 %. After this reaction, the $Sn_{0.95}Fe_{0.05}P_2O_7$ compound was stable up to 1200 °C. Since the compound was pre-calcined at 650 °C for 2 h and calcined at 900 °C for 8 h, no reaction was observed below 900 °C in DTA/TGA. However, the formation of cubic SnP_2O_7 phase occurred between 600 and 900 °C [10].

The surface of the sintered bar as shown in Fig. 68a was not homogenous and different tones of colors were observed. In relation with DTA/TGA result in, it is assumed that the cubic SnP_2O_7 decomposed to several phases at 1133 °C. The assumed decomposed phase such as SnO_2 could be present as an additional phase which reacted again with SnP_2O_7 to form other phases. This reaction may explain the effects of the sintered bar as shown in Fig. 68a. A similar result was obtained for $Sn_{0.90}Fe_{0.10}P_2O_7$ as compared to $Sn_{0.95}Fe_{0.05}P_2O_7$. The DTA/TGA result in Fig. 69b showed the endothermic reaction at 1108 °C after a 0.81 % weight loss. With this result, the same explanation of $Sn_{0.95}Fe_{0.05}P_2O_7$ is valid as for $Sn_{0.90}Fe_{0.10}P_2O_7$.

4.3.3 XRD Results of SnP_2O_7 and $Sn_{1-x}Fe_xP_2O_{7-x/2}$

The room temperature XRD results of all samples revealed cubic SnP_2O_7 as a main phase with space group of $Pa\bar{3}$. However, SnO_2 was always present as an additional phase for all samples. Fig. 70 shows the room temperature XRD pattern of un-substituted SnP_2O_7 powders as-calcined and sintered. From Fig. 70a, cubic SnO_2 phase was present in small amount for sample calcined at 650 °C for 2 h. When sintered at 1250 °C for 8 h, the additional phase of SnO_2 was present. Interestingly, the cubic SnP_2O_7 was transformed into cubic (3 x 3 x 3) superstructure. This result is in good agreement with [10]. The plausible reason for the presence of additional phase of SnO_2 could be that the $NH_4H_2PO_4$ decomposed into H_3PO_4 acid and then this acid evaporated during calcination that led to the un-reacted SnO_2. This finding confirmed the assumption made in DTA/TGA experiments.

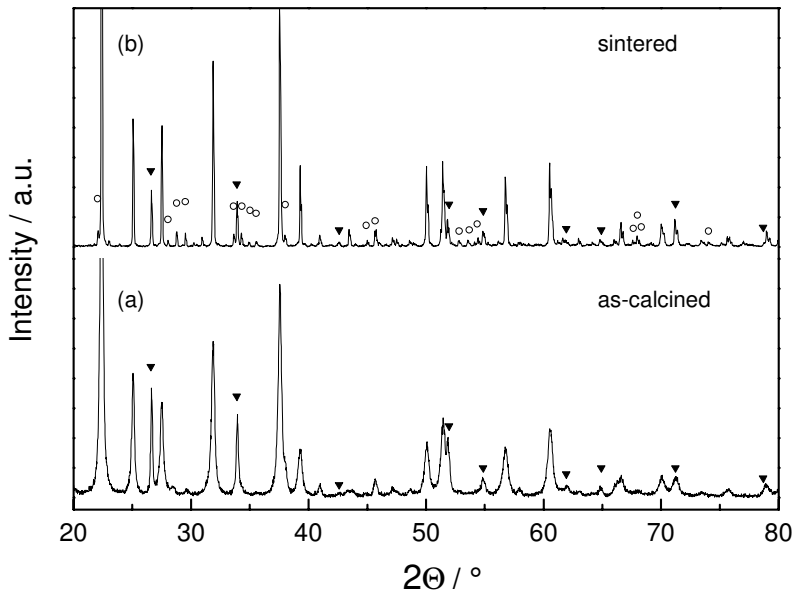

Fig. 70: Room temperature XRD pattern of SnP_2O_7 (a) as-calcined at 650 °C for 2 h and (b) sintered 1250 °C for 8 h. Unmarked peaks and closed symbols is belong to SnP_2O_7 and SnO_2 [117], respectively. The marked peaks with open circle belong to superstructure (3 x 3 x 3) of SnP_2O_7 [117].

The room temperature XRD results of $Sn_{1-x}Fe_xP_2O_{7-x/2}$ series are shown in Fig. 71. The as-calcined series at 900 °C for 8 h revealed a main phase of cubic SnP_2O_7. However, SnO_2 appeared as an additional phase. At higher Fe concentration, monoclinic $Fe(PO_3)_3$ was also present as an additional phase. Both phases were also present in $Sn_{0.80}Fe_{0.20}P_2O_7$ and $Sn_{0.70}Fe_{0.30}P_2O_7$ as shown in Fig. 71a. Consequently, similar results were obtained for sintered samples as shown in Fig. 71b. However the secondary phase of monoclinic $Fe(PO_3)_3$ transformed into hexagonal $FePO_4$. The small peaks observed in the XRD patterns were the peaks of SnP_2O_7 superstructure as already shown in Fig. 70b.

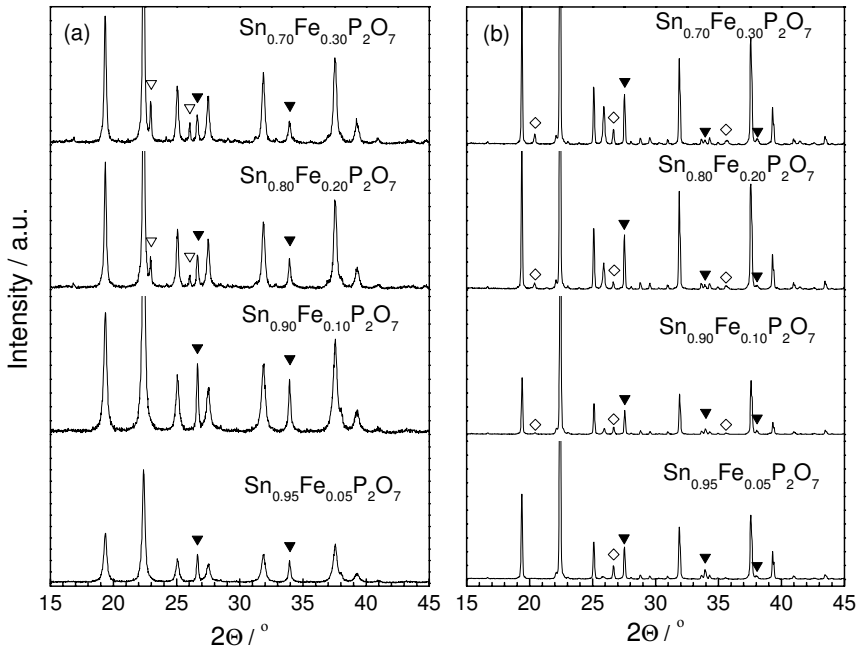

Fig. 71: Room temperature XRD pattern ($15 < 2\Theta < 45$ °) of $Sn_{1-x}Fe_xP_2O_{7-x/2}$ with x=0.05, 0.10, 0.20 and 0.30 mol per formula unit after (a) calcination at 900 °C for 8 h and (b) sintering at 1250 °C for 8 h. The unmarked peaks belong to cubic SnP_2O_7 and closed triangles to tetragonal SnO_2 [117] while open triangles and diamonds were monoclinic $Fe(PO_3)_3$ and hexagonal $Fe(PO)_4$ respectively [117].

The presence of SnO_2 phase at lower concentration of Fe could be due to the fact that the starting material, $NH_4H_2PO_4$ evaporated during the calcination which led to excess of un-reacted SnO_2. The solid state reaction method seems to be an improper method of producing single phase cubic SnP_2O_7 which is contrary to the approach reported in [109].

4.3.4 Microstructural analysis

The cross section of $Sn_{0.95}Fe_{0.05}P_2O_7$ and $Sn_{0.90}Fe_{0.10}P_2O_7$ samples sintered at 1250 °C for 8 h were studied to observe the phase distribution of the samples. Fig. 72 below shows the back-scattered image of $Sn_{0.95}Fe_{0.05}P_2O_7$ and $Sn_{0.90}Fe_{0.10}P_2O_7$. From both images, the matrix of cubic SnP_2O_7 was visible in light grey region while the darker grey region was $FePO_4$. The white colored spots belonged to the un-reacted SnO_2. All of the phases observed in the back-scattered image were deduced from EDX analysis of the elements present. Similar results were obtained for samples containing higher Fe concentration.

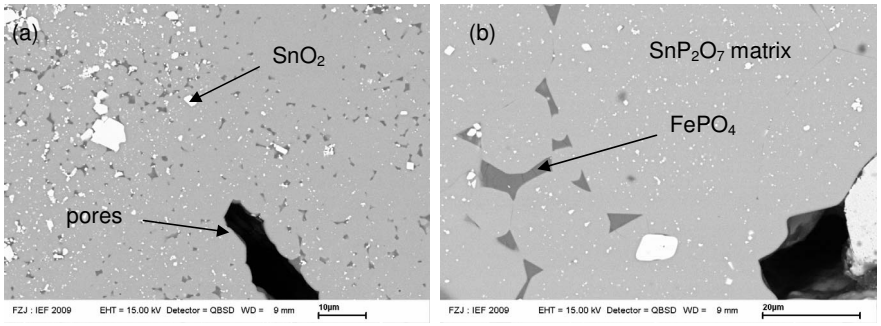

Fig. 72: Back scattered image of (a) $Sn_{0.95}Fe_{0.05}P_2O_7$ and (b) $Sn_{0.90}Fe_{0.10}P_2O_7$ sintered at 1250 °C for 8 h.

4.3.5 Electrical conductivity of SnP_2O_7 and $Sn_{1-x}Fe_xP_2O_{7-x/2}$

The electrical conductivity of the $Sn_{1-x}Fe_xP_2O_{7-x/2}$ series with x=0, 0.05, 0.08, 0.10 and 0.12 sintered at 1000 °C for 8 h was measured by 4-probes DC technique. The morphology of sample after sintering at 1000 °C for 8 h was better than that sintered at 1250 °C for 10 h. White colored bulk samples without cracking and bloating were obtained. The relative density of the samples was rather low of about 80 %; however this is in good agreement with [10]. Table 19 below shows the values of electrical conductivity at 900 °C and activation energy of the series $Sn_{1-x}Fe_xP_2O_{7-x/2}$. The values of $Sn_{0.95}In_{0.10}P_2O_7$ [10] and $Sn_{0.95}Sc_{0.10}P_2O_7$ [113] are also shown in Table 19.

Table 19: Electrical conductivity as measured in air and activation energy of $Sn_{1-x}In_xP_2O_{7-x/2}$ series.

Samples	Electrical conductivity at 900 °C (Scm^{-1})	Activation energy, E_a (eV), 400 – 900 °C
SnP_2O_7	3.78×10^{-6}	0.82
SnP_2O_7 [10]	*2.57×10^{-6}	1.09
$Sn_{0.95}Fe_{0.05}P_2O_7$	1.02×10^{-5}	0.89
$Sn_{0.90}Fe_{0.10}P_2O_7$	8.01×10^{-5}	0.91
$Sn_{0.92}In_{0.08}P_2O_7$ [10]	*6.87×10^{-6}	1.00
$Sn_{0.90}Sc_{0.10}P_2O_7$ [113]	*2.48×10^{-6}	0.98
$Sn_{0.88}Fe_{0.12}P_2O_7$	3.46×10^{-5}	0.93

*Electrical conductivity at 850 °C.

From Table 19, the highest electrical conductivity was obtained by $Sn_{0.88}Fe_{0.12}P_2O_7$ of about 3.46×10^{-5} Scm^{-1} at 900 °C. The electrical conductivity at high temperature of SnP_2O_7 substituted with Fe did not differ much from materials substituted with In and Sc [10, 113]. This indicated that the oxygen ion mobility in the polyatomic anions of $[P_2O_7]^{4-}$ structure was rather poor due to the limited oxygen vacancy concentration. The electrical conductivity in dependence of temperature is plotted in Arrhenius diagram as shown Fig. 73. From the plot, the activation energy for all samples was calculated and shown in Table 19. It is clear that the In, Sc and Fe substitutions in SnP_2O_7 did not elevate the ionic conductivity so as to be applied in intermediate or high temperature SOFCs. The activation energy of $Sn_{1-x}Fe_xP_2O_7$ series are in satisfactory agreement with [10, 113]. The basis of this bending is due to the contribution of additional phases present in the series. This is in agreement with the work reported in [10]. Tao obtained a single phase SnP_2O_7

as well as with substituted In and Sc up to some certain limit of solid solution. Linear curves were obtained from the Arrhenius plot as shown in Fig. 73 below.

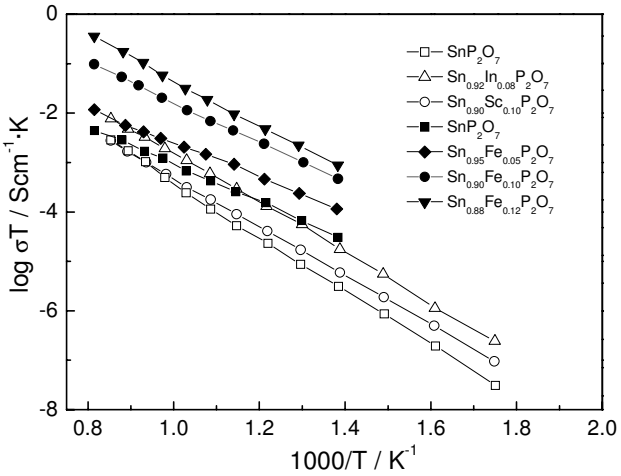

Fig. 73: Arrhenius plot of electrical conductivity of SnP_2O_7 as sintered at 1000 °C for 8 h substituted by Fe (this work, closed symbol). In and Sc substituted SnP_2O_7 (open symbols) were taken from the reported work in [10, 113].

4.3.6 Summary of SnP_2O_7 and $Sn_{1-x}Fe_xP_2O_{7-x/2}$

The synthesis of SnP_2O_7 and $Sn_{1-x}Fe_xP_2O_{7-x/2}$ series via solid state reaction was not successful to produce a single phase SnP_2O_7. Based on ionic radius analysis, Fe^{3+} has better capability of substituting Sn^{4+} than In or Sc. The room temperature XRD results confirmed that the main phase of SnP_2O_7 was detected in all samples. A superstructure of (3 x 3 x 3) of SnP_2O_7 was obtained for all samples sintered at 1250 °C for 8 h. However, additional SnO_2 were present for the entire series along with $FePO_4$ for Fe-substituted samples. The electrical conductivity of SnP_2O_7 at 900 °C was 3.78 x 10^{-6} Scm^{-1} and the highest electrical conductivity of 3.46 x 10^{-5} Scm^{-1} was obtained by $Sn_{0.88}Fe_{0.12}P_2O_7$ at 900 °C presumably due to induced electronic conductivity of mixed valent of Fe^{3+} or Fe^{4+}. Overall, the obtained electrical conductivity was rather low to be considered as ionic conductor for SOFCs, even in the case of a single phase material.

5 Conclusions

As summarized previously, materials with polyatomic anions of $[Al_2O_7]^{-8}$, $[Ti_2O_8]^{-8}$ and $[P_2O_7]^{-4}$ in the oxy-cuspidine family of $Gd_4Al_2O_9$ and $Gd_4Ti_2O_{10}$ as well as in pyrophosphate SnP_2O_7 do not show an interesting ionic conductivity that is practical for SOFC application.

However as overall conclusion, the oxy-cuspidines of monoclinic $Gd_4Al_2O_9$ and orthorhombic $Gd_4Ti_2O_{10}$ proved that the substitution of divalent cations on the Gd sites is possible and the total conductivity of both structures is similar and in-fact is often better than tetravalent substitution on the Al or Ti. Fig. 74 shows a summary of the total conductivity as plotted previously in Fig. 17, was including the data of this work.

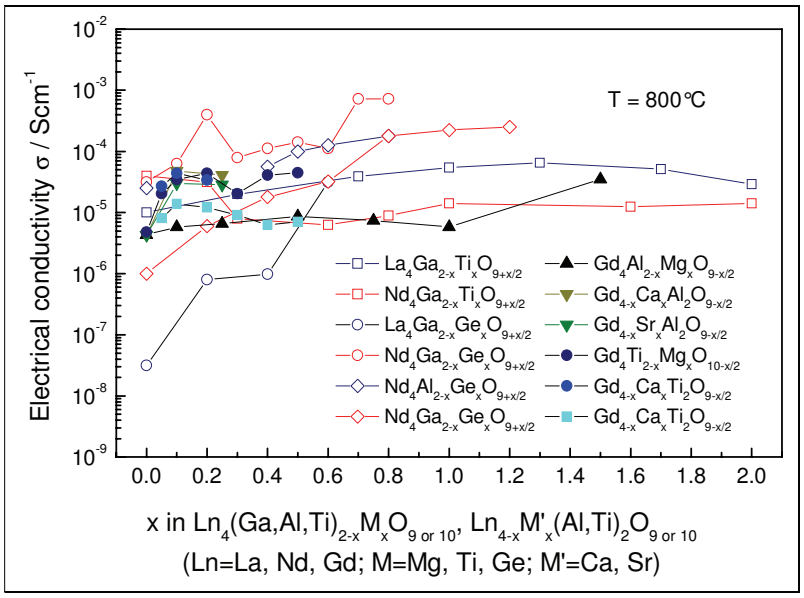

Fig. 74: Summarized total conductivity of oxy-cuspidines.

Pure pyrophosphate of SnP_2O_7 and $Sn_{1-x}Fe_xP_2O_{7-x/2}$ with x=0.05, 0.10, 0.20 and 0.30 were successfully synthesized via solid state reaction. XRD confirms that the main phase is SnP_2O_7 with space group of $Pa\bar{3}$ and is present in all samples. Additional phases of SnO_2 and $FePO_4$ were observed. The highest electrical conductivity is 3.5 $x10^{-5}$ Scm^{-1} at 900 °C for $Sn_{0.88}Fe_{0.12}P_2O_7$. The obtained results are in good agreement with work reported previously.

6 References

[1] N. Q. Minh and T. Takahashi, Science and Technology of Ceramic Fuel Cells. Amsterdam: Elsevier, 1995.

[2] "Climate Change 2007 - The Physical Science Basis Contribution of Working Group I to the Fourth Assessment Report of the IPCC (ISBN 978 0521 88009-1 Hardback; 978 0521 70596-7 Paperback)," 2007.

[3] "Climate Change 2007 - Impacts, Adaptation and Vulnerability Contribution of Working Group II to the Fourth Assessment Report of the IPCC (978 0521 88010-7 Hardback; 978 0521 70597-4 Paperback)," 2007.

[4] "Climate Change 2007 - Mitigation of Climate Change Contribution of Working Group III to the Fourth Assessment Report of the IPCC (978 0521 88011-4 Hardback; 978 0521 70598-1 Paperback)," 2007.

[5] "Center for Global Development (2007, November 15). Carbon Dioxide Emissions From Power Plants Rated Worldwide. ScienceDaily. Retrieved September 30, 2009, from http://www.sciencedaily.com /releases/2007/11/071114163448.htm," 2007.

[6] J. Beer and J. C. Cutler, "Fossil fuel power plant. In: Encyclopedia of Earth. Eds. Cutler J. Cleveland (Washington, D.C.: Environmental Information Coalition, National Council for Science and the Environment). [First published in the Encyclopedia of Earth August 30, 2006; Last revised August 21, 2008; Retrieved September 29, 2009]. <http://www.eoearth.org/article/Fossil_fuel_power_plant>," 2008.

[7] S. C. Whitfield, E. A. Rosa, A. Dan, and T. Dietz, "The Future of Nuclear Power: Value Orientations and Risk Perception," Risk Analysis, vol. 29, pp. 425-437, 2009.

[8] M. Zerta, P. R. Schmidt, C. Stiller, and H. Landinger, "Alternative World Energy Outlook (AWEO) and the role of hydrogen in a changing energy landscape," in 2nd World Congress of Young Scientists on Hydrogen Energy Systems, 2008, pp. 3021-3025.

[9] M. C. Martín-Sedeño, D. Marrero-López, E. R. Losilla, S. Bruque, P. Núñez, and M. A. G. Aranda, "Stability and oxide ion conductivity in rare-earth aluminium cuspidines," Journal of Solid State Chemistry, vol. 179, pp. 3445-3455, 2006.

[10] S. Tao, "Conductivity of SnP_2O_7 and In-doped SnP_2O_7 prepared by an aqueous solution method," Solid State Ionics, vol. 180, pp. 148-153, 2009.

[11] M. Mori, T. Abe, H. Itoh, O. Yamamoto, Y. Takeda, and T. Kawahara, "Cubic-stabilized zirconia and alumina composites as electrolytes in planar type solid oxide fuel cells," Solid State Ionics, vol. 74, pp. 157-164, 1994.

[12] W. R. Grove, Philos. Mag. (III), p. 417, 1842.

[13] W. Nernst, Z. Electrochem., vol. 6, 1899.

[14] E. Baur and Z. H. Preis, Z. Electrochem., p. 727, 1937.

[15] B. Y. S. Lin, D. W. Kirk, and S. J. Thorpe, "Performance of alkaline fuel cells: A possible future energy system?," Journal of Power Sources, vol. 161, pp. 474-483, 2006.

[16] T. E. Lipman, J. L. Edwards, and D. M. Kammen, "Fuel cell system economics: comparing the costs of generating power with stationary and motor vehicle PEM fuel cell systems," Energy Policy, vol. 32, pp. 101-125, 2004.

[17] J. M. Feret, "Westinghouse air-cooled PAFC technology," Journal of Power Sources, vol. 29, pp. 59-69, 1990.

[18] R. Rashidi, P. Berg, and I. Dincer, "Performance investigation of a combined MCFC system," International Journal of Hydrogen Energy 2nd World Hydrogen Technologies Convention, vol. 34, pp. 4395-4405, 2009.

[19] S. C. Singhal and K. Kendall (Eds.), High Temperature Solid Oxide Fuel Cells: Fundamentals, Design and Applications. Oxford, UK: Elsevier, 2003.

[20] W. Vielstich, A. Lamm, and H. A. Gasteiger (Eds.), Handbook of Fuel Cells: Fundamentals, Technology and Applications. Chichester, U.K.: John Wiley & Sons, 2003.

[21] M. C. Williams, J. P. Strakey, W. A. Surdoval, and L. C. Wilson, "Solid oxide fuel cell technology development in the U.S.," Solid State Ionics 15, vol. 177, pp. 2039-2044, 2006.

[22] L. Carrette, K. A. Friedrich, and U. Stimming, "Fuel Cells - Fundamentals and Applications," Fuel Cells, vol. 1, pp. 5-39, 2001.

[23] L. S. Langston, A year of turbulence, Am. Soc. Mechanical Eng., Power & Energy, 1 [No.2], 2004.

[24] W. Winkler, "Thermodynamics," in High Temperature Solid Oxide Fuel Cells:Fundamentals, Design and Applications, S. C. Singhal and K. Kendall (Eds.), Eds. Oxford, U.K.: Elsevier, 2003, pp. 53-82.

[25] T. Lipman and D. Sperling, in Handbook of Fuel Cells: Fundamentals, Technology and Applications. vol. 4, W. Vielstich, A. Lamm, and H. A. Gasteiger (Eds.), Eds. Chichester, U.K.: John Wiley & Sons, 2003, pp. 1318-1328.

[26] D. Stöver, H.-P. Buchkremer, and J. P. P. Huijsmans, "Handbook of Fuel Cells: Fundamentals, Technology and Applications." vol. 4, W. Vielstich, A. Lamm, and H. A. Gasteiger (Eds.), Eds. Chichester, U.K: John Wiley & Sons, 2003, pp. 1015-1031.

[27] S. C. Singhal, in Proc. 4th Int. Symp. Solid Oxide Fuel Cells (SOFC IV), Pennington, NJ, PV95-1, 1995, pp. 195-207.

[28] "Siemen Power Generation: http://www.powergeneration.siemens.com/en/fuelcells/demonstrations/index.cfm."

[29] N. Q. Minh, "Ceramic Fuel Cell," Journal of American Ceramic Society, vol. 76, pp. 563-588, 1993.

[30] K. Kendall, in Proc. 3rd Int. Symp. Solid Oxide Fuel Cells (SOFC III), Pennington, NJ, PV93-4, 1993, pp. 813-821.

[31] J. Malzbender, E. Wessel, R. W. Steinbrech, and L. Singheiser, "Reduction and re-oxidation of anodes for Solid Oxide Fuel Cells (SOFC)," in Ceram. Eng. & Sci. Proc, 2004, pp. 387-392.

[32] M. Brandner, "Herstellung einer Metall/Keramik-Verbundstruktur für Hochtemperatur-Brennstoffzellen in mobilen Anwendungen,," Bochum. Germany: Ruhr-Universität Bochum, Berichte des Forschungszentrum Jülich, 2006, p. 132.

[33] D. Simwonis, "Optimierung von Anoden der Hochtemperatur-Brennstoffzelle durch Korrelation von Herstellungsverfahren, Gefüge und Eigenschaften," Bochum, Germany: Ruhr-Universität Bochum, Berichte des Forchungszentrum Jülich, Jül-3678), 1999.

[34] F. Wiener, "Entwicklung eines Dichtungskonzepts mit elastischer Komponente für die oxidkeramische Brennstoffzelle (SOFC),," Bochum, Germany: Ruhr-Universität Bochum, Berichte des Forchungszentrum Jülich, Jül-4244, 2006, p. 121.

[35] J. Mizusaki, H. Tagawa, T. Saito, T. Yamamura, K. Kamitani, K. Hirano, S. Ehara, T. Takagi, T. Hikita, M. Ippommatsu, S. Nakagawa, and K. Hashimoto, "Kinetic studies of the reaction at the nickel pattern electrode on YSZ in H_2-H_2O atmospheres," Solid State Ionics, vol. 70-71, pp. 52-58, 1994.

[36] N. Nakagawa, H. Yoshioka, C. Kuroda, and M. Ishida, "Electrode performance of a thin-film YSZ cell set on a porous ceramic substrate by rf sputtering technique," Solid State Ionics, vol. 35, pp. 249-255, 1989.

[37] W. Huebner, D. M. Reed, and H. U. Anderson, "Solid Oxide Fuel Cell Performance Studies Anode Development.," Proceedings of the Sixth International Symposium of Solid Oxide Fuel Cells. Pennington, NJ: The Electrochemical Society, INC., 1999.

[38] E. Ivers-Tiffée, W. Wersing, M. Schießl, and H. Greiner, "Ceramic and Metallic Components for a Planar SOFC," in Ber. Bunsen-Ges. Phys. Chem, 1990, p. 978.

[39] D. W. Dees, T. D. Claar, T. E. Easler, D. C. Fee, and F. C. Mrazek, "Conductivity of Porous Ni/ZrO_2-Y_2O_3 Cermets," Journal of The Electrochemical Society, vol. 134, pp. 2141-2146, 1987.

[40] M. Suzuki, "Electrodes Materials for High Temperature Solid Electrolyte Fuel Cells," Proceedings of the Second International Symposium on Solid Oxide Fuel Cells, 1991.

[41] H. Uchida, N. Mochizuki, and M. Watanabe, "High-Performance Electrode for Medium-Temperature Operating Solid Oxide Fuel Cells," Journal of The Electrochemical Society, vol. 143, pp. 1700-1704, 1996.

[42] C. Wang, W. L. Worrell, S. Park, J. M. Vohs, and R. J. Gorte, "Fabrication and Performance of Thin-Film YSZ Solid Oxide Fuel Cells," Journal of The Electrochemical Society, vol. 148, pp. A864-A868, 2001.

[43] T. Takahashi, H. Iwahara, and Y. Suzuki, "Electrode Materials for High-Temperature Solid Electrolyte Fuel Cells," Proceedings of the Third International Symposium on Fuel Cells. Presses Académiques Européennes, Brussels , Belgium, p. 113, 1969.

[44] J. Tedmon, C. S., H. S. Spacil, and S. P. Mitoff, "Cathode Materials and Performance in High-Temperature Zirconia Electrolyte Fuel Cells," Journal of The Electrochemical Society, vol. 116, pp. 1170-1175, 1969.

[45] S. Srilomsak, D. P. Schilling, and H. U. Anderson, "Thermal Expansion Studies on Cathode and Interconnect Oxides.," Proceedings of the First International Symposium on Solid Oxide Fuel Cells., vol. The Electrochemical Society, 1989.

[46] S. T. Aruna, M. Muthuraman, and K. C. Patil, "Studies on combustion synthesized $LaMnO_3$-$LaCoO_3$ solid solutions," Materials Research Bulletin, vol. 35, pp. 289-296, 2000.

[47] M. Hrovat, S. Bernik, D. Kuscer, J. Holc, and D. Kolar, "Evaluation of the Characteristics of $La(Co_{1-x}Al_x)O_3$ as Possible SOFC Cathodes," Journal of Materials Science Letters, vol. 17, pp. 1957-1959, 1998.

[48] Z. M. Li, L. Behruzi, and D. Stover, "Proceedings of the Third International Symposium on Solid Oxide Fuel Cells.," The Electrochemical Society, 1993.

[49] J. A. Labrincha, J. R. Frade, and F. M. B. Marques, "$La_2Zr_2O_7$ formed at ceramic electrode/YSZ contacts," Journal of Materials Science, vol. 28, pp. 3809-3815, 1993.

[50] J. A. M. Van Roosmalen and E. H. P. Cordfunke, "The Defect Chemistry of $LaMnO_{3\pm d}$: 3. The Density of $(La,A)MnO_{3+d}$ (A = Ca, Sr, Ba)," Journal of Solid State Chemistry, vol. 110, pp. 106-108, 1994.

[51] T. Kenjo and M. Nishiya, "$LaMnO_3$ air cathodes containing ZrO_2 electrolyte for high temperature solid oxide fuel cells," Solid State Ionics, vol. 57, pp. 295-302, 1992.

[52] O. Yamamoto, Y. Takeda, R. Kanno, and M. Noda, "Perovskite-type oxides as oxygen electrodes for high temperature oxide fuel cells," Solid State Ionics, vol. 22, pp. 241-246, 1987.

[53] L. S. Wang, E. S. Thiele, and S. A. Barnett, "Sputter deposition of yttria-stabilized zirconia and silver cermet electrodes for SOFC applications," Solid State Ionics, vol. 52, pp. 261-267, 1992.

[54] B. C. H. Steele, "Interfacial reactions associated with ceramic ion transport membranes," Solid State Ionics: Interfaces in Ionic Materials, vol. 75, pp. 157-165, 1995.

[55] L. S. Wang and S. A. Barnett, "Ag-perovskite cermets for thin film solid oxide fuel cell air-electrode applications," Solid State Ionics, vol. 76, pp. 103-113, 1995.

[56] S. P. S. Badwal and K. Foger, "Solid oxide electrolyte fuel cell review," Ceramics International, vol. 22, pp. 257-265, 1996.

[57] J. A. Kimpton, "Conductivity and microstructural characterisation of doped zirconia-ceria and lanthanum gallate electrolytes for the intermediate-temperature solid oxide fuel cells," in School of Engineering and Science. vol. Doctor of Philosophy, Melbourne, Australia: Swinburne University of Technology, 2002, pp. 11-18.

[58] P. Kofstad, Nonstoichiometry, Diffusion and Electrical Conductivity in Binary Metal Oxides.: John Wiley & Sons, Inc., New York, 1972.

[59] J. A. Kilner, "Fast oxygen transport in acceptor doped oxides," Solid State Ionics, vol. 129, pp. 13-23, 2000.

[60] F. A. Kröger and H. J. Vink, "Relations between the Concentrations of Imperfections in Crystalline Solids Solid State Physics," in Advances in Research and Applications, Volume 3 ed, F. Seitz and D. Turnbull, Eds.: Academic Press, 1956, pp. 307-435.

[61] J. A. Kilner and C. D. Waters, "The effects of dopant cation-oxygen vacancy complexes on the anion transport properties of non-stoichiometric fluorite oxides," Solid State Ionics, vol. 6, pp. 253-259, 1982.

[62] D. Y. Wang, D. S. Park, J. Griffith, and A. S. Nowick, "Oxygen-ion conductivity and defect interactions in yttria-doped ceria," Solid State Ionics, vol. 2, pp. 95-105, 1981.

[63] J. A. Kilner and B. C. H. Steele, Non-stoichiometric Oxides: Academic Press, New York, 1981.

[64] S. P. S. Badwal, "Zirconia-based solid electrolytes: microstructure, stability and ionic conductivity," Solid State Ionics, vol. 52, pp. 23-32, 1992.

[65] V. V. Kharton, F. M. B. Marques, and A. Atkinson, "Transport properties of solid oxide electrolyte ceramics: a brief review," Solid State Ionics Dokiya Memorial Special Issue, vol. 174, pp. 135-149, 2004.

[66] V. V. Kharton, F. M. Figueiredo, L. Navarro, E. N. Naumovich, A. V. Kovalevsky, A. A. Yaremchenko, A. P. Viskup, A. Carneiro, F. M. B. Marques, and J. R. Frade, "Ceria-based materials for solid oxide fuel cells," Journal of Materials Science, vol. 36, pp. 1105-1117, 2001.

[67] H. Yahiro, K. Eguchi, and H. Arai, "Electrical properties and reducibilities of ceria-rare earth oxide systems and their application to solid oxide fuel cell," Solid State Ionics, vol. 36, pp. 71-75, 1989.

[68] N. M. Sammes, G. A. Tompsett, H. Näfe, and F. Aldinger, "Bismuth based oxide electrolytes-Structure and ionic conductivity," Journal of the European Ceramic Society, vol. 19, pp. 1801-1826, 1999.

[69] N. Jiang, E. D. Wachsman, and S.-H. Jung, "A higher conductivity Bi_2O_3 based electrolyte," Solid State Ionics, vol. 150, pp. 347-353, 2002.

[70] K. R. Kendall, J. K. Thomas, and H.-C. zur Loye, "Oxygen ion conductivity in a new class of layered bismuth oxides," Solid State Ionics, vol. 70-71, pp. 221-224, 1994.

[71] P. Lacorre, F. Goutenoire, O. Bohnke, R. Retoux, and Y. Laligant, "Designing fast oxide-ion conductors based on $La_2Mo_2O_9$," vol. 404, pp. 856-858, 2000.

[72] F. Goutenoire, O. Isnard, and R. Retoux, "Crystal Structure of $La_2Mo_2O_9$, A New Fast Oxides Ion Conductor," Chemistry of Materials, vol. 12, pp. 2575-2580, 2000.

[73] X. C. Wang and M. Y. Lui, "An arbitrary waveform control system for a precise spot-welding power source," Journal of Materials Processing Technology, vol. 122, pp. 185-188, 2002.

[74] J. B. Goodenough, "Ceramic technology: Oxide-ion conductors by design," vol. 404, pp. 821-823, 2000.

[75] J. B. Goodenough, J. E. Ruiz-Diaz, and Y. S. Zhen, "Oxide-ion conduction in $Ba_2In_2O_5$ and $Ba_3In_2MO_8$ (M=Ce, Hf, or Zr)," Solid State Ionics, vol. 44, pp. 21-31, 1990.

[76] S. Nakayama, T. Kageyama, H. Aono, and Y. Sadaoka, "Ionic conductivity of lanthanoid silicates, $Ln_{10}(SiO_4)_6O_3$ (Ln = La, Nd, Sm, Gd, Dy, Y, Ho, Er and Yb)," Journal of Materials Chemistry, vol. 5, pp. 1801-1805, 1995.

[77] S. Nakayama and M. Sakamoto, "Electrical properties of new type high oxide ionic conductor $RE_{10}Si_6O_{27}$ (RE = La, Pr, Nd, Sm, Gd, Dy)," Journal of the European Ceramic Society, vol. 18, pp. 1413-1418, 1998.

[78] S. A. Kramer and H. L. Tuller, "A novel titanate-based oxygen ion conductor: $Gd_2Ti_2O_7$," Solid State Ionics, vol. 82, pp. 15-23, 1995.

[79] F. Tietz, "Thermal expansion of SOFC materials," Ionics, vol. 5, pp. 129-139, 1999.

[80] M. Mogensen, T. Lindegaard, U. R. Hansen, and G. Mogensen, "Physical Properties of Mixed Conductor Solid Oxide Fuel Cell Anodes of Doped CeO_2," Journal of The Electrochemical Society, vol. 141, pp. 2122-2128, 1994.

[81] I. Yasuda, Y. Matsuzaki, T. Yamakawa, and T. Koyama, "Electrical conductivity and mechanical properties of alumina-dispersed doped lanthanum gallates," Solid State Ionics, vol. 135, pp. 381-388, 2000.

[82] J. W. Stevenson, T. R. Armstrong, L. R. Pederson, J. Li, C. A. Lewinsohn, and S. Baskaran, "Effect of A-site cation nonstoichiometry on the properties of doped lanthanum gallate," Solid State Ionics, vol. 113-115, pp. 571-583, 1998.

[83] J. W. Stevenson, K. Hasinska, N. L. Canfield, and T. R. Armstrong, "Influence of Cobalt and Iron Additions on the Electrical and Thermal Properties of $(La,Sr)(Ga,Mg)O_{3-d}$," Journal of The Electrochemical Society, vol. 147, pp. 3213-3218, 2000.

[84] A. A. Yaremchenko, V. V. Kharton, E. N. Naumovich, A. A. Tonoyan, and V. V. Samokhval, "Oxygen ionic transport in Bi_2O_3 based oxides: II. The Bi_2O_3-ZrO_2-Y_2O_3 and Bi_2O_3-Nb_2O_5-Ho_2O_3 solid solutions," Journal of Solid State Electrochemistry, vol. 2, pp. 308-314, 1998.

[85] A. L. Shaula, V. V. Kharton, J. C. Waerenborgh, D. P. Rojas, E. V. Tsipis, N. P. Vyshatko, M. V. Patrakeev, and F. M. B. Marques, "Transport properties and Mössbauer spectra of Fe-substituted $La_{10-x}(Si,Al)_6O_{26}$ apatites," Materials Research Bulletin, vol. 39, pp. 763-773, 2004.

[86] V. V. Kharton, A. L. Shaula, M. V. Patrakeev, J. C. Waerenborgh, D. P. Rojas, N. P. Vyshatko, E. V. Tsipis, A. A. Yaremchenko, and F. M. B. Marques, "Oxygen Ionic and Electronic Transport in Apatite-Type Solid Electrolytes," Journal of The Electrochemical Society, vol. 151, pp. A1236-A1246, 2004.

[87] M. Mori, G. M. Tompsett, N. M. Sammes, E. Suda, and Y. Takeda, "Compatibility of $Gd_xTi_2O_7$ pyrochlores (1.72<=x<=2.0) as electrolytes in high-temperature solid oxide fuel cells," Solid State Ionics, vol. 158, pp. 79-90, 2003.

[88] S. Merlino and N. Perchiazzi, "Modular mineralogy in the cuspidine group of minerals," Canadian Mineralogist, vol. 26, pp. 933-943, 1988.

[89] S. Saburi, A. Kawahara, C. Henmi, I. Kusachi, and K. Kihara, "The Refinement of The Structure of Cuspidine," in MINERAL J. vol. 8, 1977, p. 286.

[90] K. Mamedov and N. V. Belov, Geochem., p. 1056, 1964.

[91] V. Venkatakrishnan and M. J. Buerger, Z. Krist, vol. 135, p. 321, 1972.

[92] P. B. Moore and T. Araki, Amer. MIneral, vol. 59, p. 985, 1974.

[93] E. F. Bertaud, Acta Crystallographica, vol. 3, p. 473, 1950.

[94] E. F. Bertaud and M. Guillen, vol. 72, p. 57, 1966.

[95] W. G. Mumme and A. D. Wadsley, "Structure of Orthorhombic Y_2TiO_5 an Example of Mixed 7- and Fivefold Coordination," Acta Crystallographica Section B-Structural Crystallography and Crystal Chemistry, vol. B 24, pp. 1327-&, 1968.

[96] H. Muller-Buschbaum and K. Scheunemann, "Zur Kenntnis von Nd_2TiO_5," Journal of Inorganic Nuclear Chemistry, vol. 35, p. 1091, 1973.

[97] O. Joubert, A. Magrez, A. Chesnaud, M. T. Caldes, V. Jayaraman, Y. Piffard, and L. Brohan, "Structural and transport properties of a new class of oxide ion conductors: $Nd_4[Ga_{2(1-x)}M_{2x}O_7]O_2$ (M = Ti, Ge)," Solid State Sciences, vol. 4, pp. 1413-1418, 2002.

[98] M. C. Martín-Sedeño, D. Marrero-López, E. R. Losilla, L. Leon-Reina, S. Bruque, P. Núñez, and M. A. G. Aranda, "Structural and Electrical Investigation of Oxide Ion and Proton Conducting Titanium Cuspidines," Chemistry of Materials, vol. 17, pp. 5989-5998, 2005.

[99] A. Chesnaud, O. Joubert, M. T. Caldes, S. Ghosh, Y. Piffard, and L. Brohan, "Cuspidine-like compounds $Ln_4[Ga_{2(1-x)}Ge_{2x}O_7]O_2$ (Ln=La, Nd, Gd; x <= 0.4)," Chemistry of Materials, vol. 16, pp. 5372-5379, 2004.

[100] M. C. Martín-Sedeño, E. R. Losilla, L. Leon-Reina, S. Bruque, D. Marrero-López, P. Núñez, and M. A. G. Aranda, "Enhancement of oxide ion conductivity in cuspidine-type materials," Chemistry of Materials, vol. 16, pp. 4960-4968, 2004.

[101] H. Yamane, K. Ogawara, M. Omori, and T. Hirai, "Phase Transition of Rare-Earth Aluminates ($RE_4Al_2O_9$) and Rare-Earth Gallates ($RE_4Ga_2O_9$)," Journal of the American Ceramic Society, vol. 78, pp. 2385-2390, 1995.

[102] A. Sinha, B. P. Sharma, and P. Gopalan, "Development of novel perovskite based oxide ion conductor," Electrochimica Acta, vol. 51, pp. 1184-1193, 2006.

[103] M. Shimada, H. Yamane, H. Takizawa, and T. Endo, "Phase Transformation of $Gd_4Al_2O_9$ at High Temperature," Key Engineering Materials, vol. 132, p. 647, 1997.

[104] M. Gervais and A. Douy, "Solid phase transformation and melting of the compounds $Ln_4Al_2O_9$ (Ln=Gd, Dy, Y)," Materials Science and Engineering B-Solid State Materials for Advanced Technology, vol. 38, pp. 118-121, 1996.

[105] S. Chaudhury, S. C. Parida, K. T. Pillai, and K. D. S. Mudher, "High-temperature X-ray diffraction and specific heat studies on $GdAlO_3$, $Gd_3Al_5O_{12}$ and $Gd_4Al_2O_9$," Journal of Solid State Chemistry, vol. 180, pp. 2393-2399, 2007.

[106] G. Panneerselvam, R. Venkata Krishnan, M. P. Antony, K. Nagarajan, T. Vasudevan, and P. R. Vasudeva Rao, "Thermophysical measurements on dysprosium and gadolinium titanates," Journal of Nuclear Materials, vol. 327, pp. 220-225, 2004.

[107] M. A. Petrova, A. S. Novikova, and R. G. Grebenshchikov, "Phase Relations in the Pseudobinary Systems La_2TiO_5-Lu_2TiO_5 and Gd_2TiO_5-Tb_2TiO_5," Inorganic Materials, vol. 39, pp. 509-513, 2003.

[108] K. Kwon, M. Yano, H. Sun, and Park, "J.U.S. Pat. Appl. Publ. US 2005221143 A1 20051006," 2005.

[109] M. Nagao, A. Takeuchi, P. Heo, T. Hibino, M. Sano, and A. Tomitab, "A proton-conducting In^{3+} doped SnP_2O_7 electrolyte for intermediate-temperature fuel cells," Electrochemical and Solid State Letters, vol. 9, pp. A105-A109, 2006.

[110] P. Heo, H. Shibata, M. Nagao, T. Hibino, and M. Sano, "Performance of an Intermediate-Temperature Fuel Cell Using a Proton-Conducting $Sn_{0.9}In_{0.1}P_2O_7$ Electrolyte," Journal of The Electrochemical Society, vol. 153, pp. A897-A901, 2006.

[111] V. Nalini, T. Norby, and A. M. Anuradha, "Proc 10th Asian Conf Solid State Ionics," in Kandy, Sri Lanka, 2006, pp. 321–328.

[112] T. Norby, R. Haugsrud, and N. Vajeeston, in Proc. 9th Int. Conf. Inorganic Membranes, Lillehammer, Norway, 2006, pp. 260-267.

[113] R. Lan and S. Tao, "Conductivity of a new pyrophosphate $Sn_{0.9}Sc_{0.1}(P_2O_7)_{1-d}$ prepared by an aqueous solution method," Journal of Alloys and Compounds, vol. In Press, Corrected Proof, 2009.

[114] F. Tietz, I. Arul Raj, W. Jungen, and D. Stöver, "High-temperature superconductor materials for contact layers in solid oxide fuel cells: I. Sintering behavior and physical properties at operating temperatures," Acta Materialia, vol. 49, pp. 803-810, 2001.

[115] B. Raue, H.-J. r. Brauch, and F. H. Frimmel, "Determination of sulphate in natural waters by ICP/OES: comparative studies with ion chromatography," Fresenius' Journal of Analytical Chemistry, vol. 340, pp. 395-398, 1991.

[116] R. D. Shannon, "Revised Effective Ionic-Radii and Systematic Studies of Interatomic Distances in Halides and Chalcogenides," Acta Crystallographica Section A, vol. 32, pp. 751-767, 1976.

[117] "International Center for Diffraction Data (ICDD), PDF: No. 00-046-0396 ($Gd_4Al_2O_9$), No. 00-046-0395 ($GdAlO_3$), No. 00-024-0192 ($CaGaAlO_4$), No. 01-076-0095 ($SrGd_2Al_2O_7$), No. 01-088-0107 (Al_2O_3), No. 00-046-0395 (MgO), No. 00-043-1015 (Gd_2O_3), No. 00-042-1465 (Gd_2O_3), No. 00-021-0842 ($Gd_4Ti_2O_{10}$), No. 00-029-0614 ($GdTiO_3$), No. 01-073-7752 ($SrTiO_3$), No. 00-029-1352 (SnP_2O_7), No. 01-077-0447 (SnO_2), No. 01-089-8524 ($Fe(PO_3)_3$), No. 01-084-0876 ($Fe(PO)_4$), No. 99-000-0014 (3 x 3 x 3 SnP_2O_7)," N.S, PA, U.S.A.

[118] C. D. Brandle and Steinfin.H, "Crystal Structure of $Eu_4Al_2O_9$," Inorganic Chemistry, vol. 8, p. 1320, 1969.

[119] T. Ishihara, H. Matsuda, and Y. Takita, "Doped $LaGaO_3$ Perovskite Type Oxide as a New Oxide Ionic Conductor," Journal of the American Chemical Society, vol. 116, pp. 3801-3803, 1994.

[120] D. Lybye, F. W. Poulsen, and M. Mogensen, "Conductivity of A- and B-site doped $LaAlO_3$, $LaGaO_3$, $LaScO_3$ and $LaInO_3$ perovskites," Solid State Ionics, vol. 128, pp. 91-103, 2000.

[121] D. Simwonis, F. Tietz, and D. Stover, "Nickel coarsening in annealed Ni/8YSZ anode substrates for solid oxide fuel cells - In memoriam to Professor H. Tagawa," Solid State Ionics, vol. 132, pp. 241-251, 2000.

[122] V. V. Kharton, E. N. Naumovich, and A. A. Vecher, "Research on the electrochemistry of oxygen ion conductors in the former Soviet Union. I. ZrO_2 based ceramic materials," Journal of Solid State Electrochemistry, vol. 3, pp. 61-81, 1999.

[123] O. H. Hassan, F. Tietz, and D. Stover, "Electrical conductivity and thermal expansion of the oxy-cuspidine $Gd_4Al_2O_9$ substituted with Ca and Sr.," Solid State Ionics, vol. 180, pp. 831-834, 2009.

[124] R. Vassen, M. Dietrich, H. Lehmann, X. Cao, G. Pracht, F. Tietz, D. Pitzer, and D. Stover, "Development of oxide ceramics for an application as TBC," Materialwissenschaft Und Werkstofftechnik, vol. 32, pp. 673-677, 2001.

[125] H. Muller-Buschbaum and J. P. Wepner, "Zur Kenntnis von Eu_2TiO_5," Journal of Alloys and Compounds, vol. 206, pp. L11-L13, 1994.

[126] T. Shimura, K. Suzuki, and H. Iwahara, "Conduction properties of Mg-, Fe- or Co-substituted Sr_2TiO_4 at elevated temperatures," Solid State Ionics, vol. 125, pp. 313-318, 1999.

[127] E. Kendrick, M. Russ, and P. R. Slater, "A computational study of oxide ion migration and water incorporation in the cuspidine system, $La_4(Ti_2O_8)O_2$," Solid State Ionics 16, vol. 179, pp. 819-822, 2008.

[128] K. V. Syamala, G. Panneerselvam, G. G. S. Subramanian, and M. P. Antony, "Synthesis, characterization and thermal expansion studies on europium titanate (Eu_2TiO_5)," Thermochimica Acta, vol. 475, pp. 76-79, 2008.

[129] D. Gulamova and Z. Turdiev, "Properties of oxide compounds, obtained by molten phase synthesis via action of concentrated solar radiation," Applied Solar Energy, vol. 45, pp. 38-44, 2009.

Acknowledgements

In the Name of God the Most Merciful and Most Gracious, thank you for His blessing and merci in the completion of my PhD studies.

There are some people who made my research life became smooth and rewarding. They always there in giving support and encouragement prior to my PhD studies in Germany. Foremost, I would like to express my sincere gratitude to Prof. Detlev Stöver for his kindness and willingness to accept me as his PhD student in the Institute for Energy Research, IEF-1.

My utmost gratitude goes to my supervisor, Dr. Frank Tietz for his valuable supervisions, continuous support, patience, motivation, enthusiasm, and immense knowledge that take me to this success today and specifically for his persistent and meticulous attitude. He is really my great gurus.

For my PhD defends, my sincere thanks goes to Prof. Dr. Robert Vassen as my co-examiner and Prof Dr. Martin Mönnigmann as the chairman for my session. I am indebted to Frau Brigit Treu, for her kind assistance and helping hands during the preparation for the viva. In general, I would like to thank the Faculty of Mechanical Engineering, University of Ruhr Bochum.

I am grateful to Dr. Peter Buchkremer for his supports and advise regarding the SOFCs technology, Mr. Bader for his effortless assistance with the sintering work of my materials and Mr. Cönen for the assistance with CIP and HIP preparation. Not to forget Frau Marie Theres for her kind assistance with thermal analysis and thermal expansion experiments, Frau Michaela Andreas for the chemicals supply, Frau Andreas Hilger for the particle size analysis measurements and Frau Hiltrud Moitrux for the photo and graphics work.

Many people become involved when the work was scaled-up. Among these were those in the materials characterization group, Dr. Fischer, the late Mr. Lersch and Mr. Zuigner for their kind assistance with XRD work and also Dr. Sebold and Mr. Kappertz for their kind assistance with SEM analysis and samples preparation.

I also thank Prof W. Sitte from Uni Leoben, Austria for his kind assistance with my AC impedance measurements.

It would not have been possible without the moral and spiritual support through my up and down during my study from Kamran Karim, Maria Ophelia, Feng Han, Qingxi Fu, Qian Li Ma and Rrohini Wandekar.

To all my former and present PhD colleagues in IEF-1, I owe my deepest gratitude for their spirits of collegiality and congeniality; Thomas Kiefer, Jean-Bernard Bouche, Xabier Montero, Florian Wiener, Alexander Stuke, George van der Donk, Alexander Stuke, Herwig Schiefer, Robert Mücke, Alessandro Casu, Marco Brandner, Natividad Jordán Escalona, Manuel Köhl, Wolfgang Schaffbauer, Holger Kassner, Michael Betz, Felix Hauler, Katarina Brands, Rafael Berhane, Ana Paula Cysne Barbosa, Andreas Hospach, Anita Neumann, Falk Schülze-Küppers, Meng Li, Alexander, Ye Xing, Hyo Jeong Moon, Alexander Guignard….

Above all, I thank my wife, Mazyan Yahaya and my kids, Hazimah, Naqibah, Yahaya and Hakimah who stood beside me and never failed to inspire me. I really owe them a millions and it would take another thesis to express my deepest love and gratitude. As every man success, there are stories behind and it goes for me too. Special and exceptional thanks to my beloved parent, Mrs. Normawati Desa and Mr. Hassan Ismail, my brothers and sisters, Hasnor, Hasri, Maheran and Hanim for their endless encouragement, moral and spiritual support.

Finally I am grateful to Malaysia Higher Education Ministry and Universiti Teknologi MARA for the award of PhD scholarship, especially to the Faculty of Arts and Design.

Curriculum-vitae (Lebenslauf and bildungsgang)

Personal Information

Name	:	Oskar Hasdinor Hassan
Date of Birth	:	20th April 1976
Place of Birth	:	Kuching-Sarawak, Malaysia.
Age	:	33
Citizen	:	Malaysia
Status	:	Married

Occupation (permanent)

Position	:	Teaching and researching
Address	:	Ceramics Department, Faculty of Art & Design, Universiti Teknologi MARA (UiTM), 40450 SHAH ALAM, Selangor, Malaysia
Contact	:	603 55444001 (Phone) 603 55444011 (Fax) oskar@salam.uitm.edu.my o.h.hassan@fz-juelich.de (present corresponding email)

Qualification / Studies

1994 to 1996	:	A-Level (Matriculation) from Universiti Sains Malaysia.
1996 to 1999	:	Bachelor of Engineering (Materials Engineering) with Honours - BEng. Hons. from Universiti Sains Malaysia.
1999 to 2000	:	Master of Science (Materials Engineering) – MSc from Universiti Sains Malaysia.

Working Experience

1998 (6 months)	:	Industrial training at Shin Etsu Malaysia (semiconductor factory) – R & D section.
2000 to present	:	UiTM permanent teaching and research staff; Responsible for conventional ceramics (Clay Based / alumina - silicate groups), raw materials processing, fabrication process and application.
2006 to present	:	Stipend from UiTM as PhD student in Institute für Energieforschung (IEF-1), Jülich Forshcungzentrum, Jülich, Germany.

1. **Einsatz von multispektralen Satellitenbilddaten in der Wasserhaushalts- und Stoffstrommodellierung – dargestellt am Beispiel des Rureinzugsgebietes**
   von C. Montzka (2008), XX, 238 Seiten
   ISBN: 978-3-89336-508-1

2. **Ozone Production in the Atmosphere Simulation Chamber SAPHIR**
   by C. A. Richter (2008), XIV, 147 pages
   ISBN: 978-3-89336-513-5

3. **Entwicklung neuer Schutz- und Kontaktierungsschichten für Hochtemperatur-Brennstoffzellen**
   von T. Kiefer (2008), 138 Seiten
   ISBN: 978-3-89336-514-2

4. **Optimierung der Reflektivität keramischer Wärmedämmschichten aus Yttrium-teilstabilisiertem Zirkoniumdioxid für den Einsatz auf metallischen Komponenten in Gasturbinen**
   von A. Stuke (2008), X, 201 Seiten
   ISBN: 978-3-89336-515-9

5. **Lichtstreuende Oberflächen, Schichten und Schichtsysteme zur Verbesserung der Lichteinkopplung in Silizium-Dünnschichtsolarzellen**
   von M. Berginski (2008), XV, 171 Seiten
   ISBN: 978-3-89336-516-6

6. **Politikszenarien für den Klimaschutz IV – Szenarien bis 2030**
   hrsg.von P. Markewitz, F. Chr. Matthes (2008), 376 Seiten
   ISBN 978-3-89336-518-0

7. **Untersuchungen zum Verschmutzungsverhalten rheinischer Braunkohlen in Kohledampferzeugern**
   von A. Schlüter (2008), 164 Seiten
   ISBN 978-3-89336-524-1

8. **Inorganic Microporous Membranes for Gas Separation in Fossil Fuel Power Plants**
   by G. van der Donk (2008), VI, 120 pages
   ISBN: 978-3-89336-525-8

9. **Sinterung von Zirkoniumdioxid-Elektrolyten im Mehrlagenverbund der oxidkeramischen Brennstoffzelle (SOFC)**
   von R. Mücke (2008), VI, 165 Seiten
   ISBN: 978-3-89336-529-6

10. **Safety Considerations on Liquid Hydrogen**
    by K. Verfondern (2008), VIII, 167 pages
    ISBN: 978-3-89336-530-2

11. **Kerosinreformierung für Luftfahrtanwendungen**
    von R. C. Samsun (2008), VII, 218 Seiten
    ISBN: 978-3-89336-531-9

12. **Der 4. Deutsche Wasserstoff Congress 2008 – Tagungsband**
    hrsg. von D. Stolten, B. Emonts, Th. Grube (2008), 269 Seiten
    ISBN: 978-3-89336-533-3

13. **Organic matter in Late Devonian sediments as an indicator for environmental changes**
    by M. Kloppisch (2008), XII, 188 pages
    ISBN: 978-3-89336-534-0

14. **Entschwefelung von Mitteldestillaten für die Anwendung in mobilen Brennstoffzellen-Systemen**
    von J. Latz (2008), XII, 215 Seiten
    ISBN: 978-3-89336-535-7

15. **RED-IMPACT**
    Impact of Partitioning, Transmutation and Waste Reduction Technologies on the Final Nuclear Waste Disposal
    SYNTHESIS REPORT
    ed. by W. von Lensa, R. Nabbi, M. Rossbach (2008), 178 pages
    ISBN 978-3-89336-538-8

16. **Ferritic Steel Interconnectors and their Interactions with Ni Base Anodes in Solid Oxide Fuel Cells (SOFC)**
    by J. H. Froitzheim (2008), 169 pages
    ISBN: 978-3-89336-540-1

17. **Integrated Modelling of Nutrients in Selected River Basins of Turkey**
    Results of a bilateral German-Turkish Research Project
    project coord. M. Karpuzcu, F. Wendland (2008), XVI, 183 pages
    ISBN: 978-3-89336-541-8

18. **Isotopengeochemische Studien zur klimatischen Ausprägung der Jüngeren Dryas in terrestrischen Archiven Eurasiens**
    von J. Parplies (2008), XI, 155 Seiten, Anh.
    ISBN: 978-3-89336-542-5

19. **Untersuchungen zur Klimavariabilität auf dem Tibetischen Plateau - Ein Beitrag auf der Basis stabiler Kohlenstoff- und Sauerstoffisotope in Jahrringen von Bäumen waldgrenznaher Standorte**
    von J. Griessinger (2008), XIII, 172 Seiten
    ISBN: 978-3-89336-544-9

20. **Neutron-Irradiation + Helium Hardening & Embrittlement Modeling of 9%Cr-Steels in an Engineering Perspective (HELENA)**
by R. Chaouadi (2008), VIII, 139 pages
ISBN: 978-3-89336-545-6

21. **in Bearbeitung**

22. **Verbundvorhaben APAWAGS (AOEV und Wassergenerierung) – Teilprojekt: Brennstoffreformierung – Schlussbericht**
von R. Peters, R. C. Samsun, J. Pasel, Z. Porš, D. Stolten (2008), VI, 106 Seiten
ISBN: 978-3-89336-547-0

23. **FREEVAL**
Evaluation of a Fire Radiative Power Product derived from Meteosat 8/9 and Identification of Operational User Needs
Final Report
project coord. M. Schultz, M. Wooster (2008), 139 pages
ISBN: 978-3-89336-549-4

24. **Untersuchungen zum Alkaliverhalten unter Oxycoal-Bedingungen**
von C. Weber (2008), VII, 143, XII Seiten
ISBN: 978-3-89336-551-7

25. **Grundlegende Untersuchungen zur Freisetzung von Spurstoffen, Heißgaschemie, Korrosionsbeständigkeit keramischer Werkstoffe und Alkalirückhaltung in der Druckkohlenstaubfeuerung**
von M. Müller (2008), 207 Seiten
ISBN: 978-3-89336-552-4

26. **Analytik von ozoninduzierten phenolischen Sekundärmetaboliten in *Nicotiana tabacum* L. cv Bel W3 mittels LC-MS**
von I. Koch (2008), III, V, 153 Seiten
ISBN 978-3-89336-553-1

27. **IEF-3 Report 2009. Grundlagenforschung für die Anwendung**
(2009), ca. 230 Seiten
ISBN: 978-3-89336-554-8

28. **Influence of Composition and Processing in the Oxidation Behavior of MCrAlY-Coatings for TBC Applications**
by J. Toscano (2009), 168 pages
ISBN: 978-3-89336-556-2

29. **Modellgestützte Analyse signifikanter Phosphorbelastungen in hessischen Oberflächengewässern aus diffusen und punktuellen Quellen**
von B. Tetzlaff (2009), 149 Seiten
ISBN: 978-3-89336-557-9

30. **Nickelreaktivlot / Oxidkeramik – Fügungen als elektrisch isolierende Dichtungskonzepte für Hochtemperatur-Brennstoffzellen-Stacks**
von S. Zügner (2009), 136 Seiten
ISBN: 978-3-89336-558-6

31. **Langzeitbeobachtung der Dosisbelastung der Bevölkerung in radioaktiv kontaminierten Gebieten Weißrusslands – Korma-Studie**
von H. Dederichs, J. Pillath, B. Heuel-Fabianek, P. Hill, R. Lennartz (2009), Getr. Pag.
ISBN: 978-3-89336-532-3

32. **Herstellung von Hochtemperatur-Brennstoffzellen über physikalische Gasphasenabscheidung**
von N. Jordán Escalona (2009), 148 Seiten
ISBN: 978-3-89336-532-3

33. **Real-time Digital Control of Plasma Position and Shape on the TEXTOR Tokamak**
by M. Mitri (2009), IV, 128 pages
ISBN: 978-3-89336-567-8

34. **Freisetzung und Einbindung von Alkalimetallverbindungen in kohlebefeuerten Kombikraftwerken**
von M. Müller (2009), 155 Seiten
ISBN: 978-3-89336-568-5

35. **Kosten von Brennstoffzellensystemen auf Massenbasis in Abhängigkeit von der Absatzmenge**
von J. Werhahn (2009), 242 Seiten
ISBN: 978-3-89336-569-2

36. **Einfluss von Reoxidationszyklen auf die Betriebsfestigkeit von anodengestützten Festoxid-Brennstoffzellen**
von M. Ettler (2009), 138 Seiten
ISBN: 978-3-89336-570-8

37. **Großflächige Plasmaabscheidung von mikrokristallinem Silizium für mikromorphe Dünnschichtsolarmodule**
von T. Kilper (2009), XVII, 154 Seiten
ISBN: 978-3-89336-572-2

38. **Generalized detailed balance theory of solar cells**
by T. Kirchartz (2009), IV, 198 pages
ISBN: 978-3-89336-573-9

39. **The Influence of the Dynamic Ergodic Divertor on the Radial Electric Field at the Tokamak TEXTOR**
von J. W. Coenen (2009), xii, 122, XXVI pages
ISBN: 978-3-89336-574-6

40. **Sicherheitstechnik im Wandel Nuklearer Systeme**
von K. Nünighoff (2009), viii, 215 Seiten
ISBN: 978-3-89336-578-4

41. **Pulvermetallurgie hochporöser NiTi-Legierungen für Implanat- und Dämpfungsanwendungen**
von M. Köhl (2009), XVII, 199 Seiten
ISBN: 978-3-89336-580-7

42. **Einfluss der Bondcoatzusammensetzung und Herstellungsparameter auf die Lebensdauer von Wärmedämmschichten bei zyklischer Temperaturbelastung**
von M. Subanovic (2009), 188, VI Seiten
ISBN: 978-3-89336-582-1

43. **Oxygen Permeation and Thermo-Chemical Stability of Oxygen Permeation Membrane Materials for the Oxyfuel Process**
by A. J. Ellett (2009), 176 pages
ISBN: 978-3-89336-581-4

44. **Korrosion von polykristallinem Aluminiumoxid (PCA) durch Metalljodidschmelzen sowie deren Benetzungseigenschaften**
von S. C. Fischer (2009), 148 Seiten
ISBN: 978-3-89336-584-5

45. **IEF-3 Report 2009. Basic Research for Applications**
(2009), 217 Seiten
ISBN: 978-3-89336-585-2

46. **Verbundvorhaben ELBASYS (Elektrische Basissysteme in einem CFK-Rumpf) - Teilprojekt: Brennstoffzellenabgase zur Tankinertisierung - Schlussbericht**
von R. Peters, J. Latz, J. Pasel, R. C. Samsun, D. Stolten
(2009), xi, 202 Seiten
ISBN: 978-3-89336-587-6

47. **Aging of ^{14}C-labeled Atrazine Residues in Soil: Location, Characterization and Biological Accessibility**
by N. D. Jablonowski (2009), IX, 104 pages
ISBN: 978-3-89336-588-3

48. **Entwicklung eines energetischen Sanierungsmodells für den europäischen Wohngebäudesektor unter dem Aspekt der Erstellung von Szenarien für Energie- und CO_2 - Einsparpotenziale bis 2030**
von P. Hansen (2009), XXII, 281 Seiten
ISBN: 978-3-89336-590-6

49. **Reduktion der Chromfreisetzung aus metallischen Interkonnektoren für Hochtemperaturbrennstofzellen durch Schutzschichtsysteme**
von R. Trebbels (2009), iii, 135 Seiten
ISBN: 978-3-89336-591-3

50. **Bruchmechanische Untersuchung von Metall / Keramik-Verbundsystemen für die Anwendung in der Hochtemperaturbrennstoffzelle**
von B. Kuhn (2009), 118 Seiten
ISBN: 978-3-89336-592-0

51. **Wasserstoff-Emissionen und ihre Auswirkungen auf den arktischen Ozonverlust**
Risikoanalyse einer globalen Wasserstoffwirtschaft
von T. Feck (2009), 180 Seiten
ISBN: 978-3-89336-593-7

52. **Development of a new Online Method for Compound Specific Measurements of Organic Aerosols**
by T. Hohaus (2009), 156 pages
ISBN: 978-3-89336-596-8

53. **Entwicklung einer FPGA basierten Ansteuerungselektronik für Justageeinheiten im Michelson Interferometer**
von H. Nöldgen (2009), 121 Seiten
ISBN: 978-3-89336-599-9

54. **Observation – and model – based study of the extratropical UT/LS**
by A. Kunz (2010), xii, 120, xii pages
ISBN: 978-3-89336-603-3

55. **Herstellung polykristalliner Szintillatoren für die Positronen-Emissions-Tomographie (PET)**
von S. K. Karim (2010), VIII, 154 Seiten
ISBN: 978-3-89336-610-1

56. **Kombination eines Gebäudekondensators mit H2-Rekombinatorelementen in Leichwasserreaktoren**
von S. Kelm (2010), vii, 119 Seiten
ISBN: 978-3-89336-611-8

57. **Plant Leaf Motion Estimation Using A 5D Affine Optical Flow Model**
by T. Schuchert (2010), X, 143 pages
ISBN: 978-3-89336-613-2

58. **Tracer-tracer relations as a tool for research on polar ozone loss**
by R. Müller (2010), 116 pages
ISBN: 978-3-89336-614-9

59. **Sorption of polycyclic aromatic hydrocarbon (PAH) to Yangtze River sediments and their components**
by J. Zhang (2010), X, 109 pages
ISBN: 978-3-89336-616-3

60. **Weltweite Innovationen bei der Entwicklung von CCS-Technologien und Möglichkeiten der Nutzung und des Recyclings von CO_2**
Studie im Auftrag des BMWi
von W. Kuckshinrichs et al. (2010), X, 139 Seiten
ISBN: 978-3-89336-617-0

61. **Herstellung und Charakterisierung von sauerstoffionenleitenden Dünnschichtmembranstrukturen**
von M. Betz (2010), XII, 112 Seiten
ISBN: 978-3-89336-618-7

62. **Politikszenarien für den Klimaschutz V – auf dem Weg zum Strukturwandel, Treibhausgas-Emissionsszenarien bis zum Jahr 2030**
hrsg. von P. Hansen, F. Chr. Matthes (2010), 276 Seiten
ISBN: 978-3-89336-619-4

63. **Charakterisierung Biogener Sekundärer Organischer Aerosole mit Statistischen Methoden**
von C. Spindler (2010), iv, 163 Seiten
ISBN: 978-3-89336-622-4

64. **Stabile Algorithmen für die Magnetotomographie an Brennstoffzellen**
von M. Wannert (2010), ix, 119 Seiten
ISBN: 978-3-89336-623-1

65. **Sauerstofftransport und Degradationsverhalten von Hochtemperatur-membranen für CO2-freie Kraftwerke**
von D. Schlehuber (2010), VII, 139 Seiten
ISBN: 978-3-89336-630-9

66. **Entwicklung und Herstellung von foliengegossenen, anodengestützten Festoxidbrennstoffzellen**
von W. Schafbauer (2010), VI, 164 Seiten
ISBN: 978-3-89336-631-6

67. **Disposal strategy of proton irradiated mercury from high power spallation sources**
by S. Chiriki (2010), xiv, 124 pages
ISBN: 978-3-89336-632-3

68. **Oxides with polyatomic anions considered as new electrolyte materials for solid oxide fuel cells (SOFCs)**
by O. H. Bin Hassan (2010), vii, 121 pages
ISBN: 978-3-89336-633-0

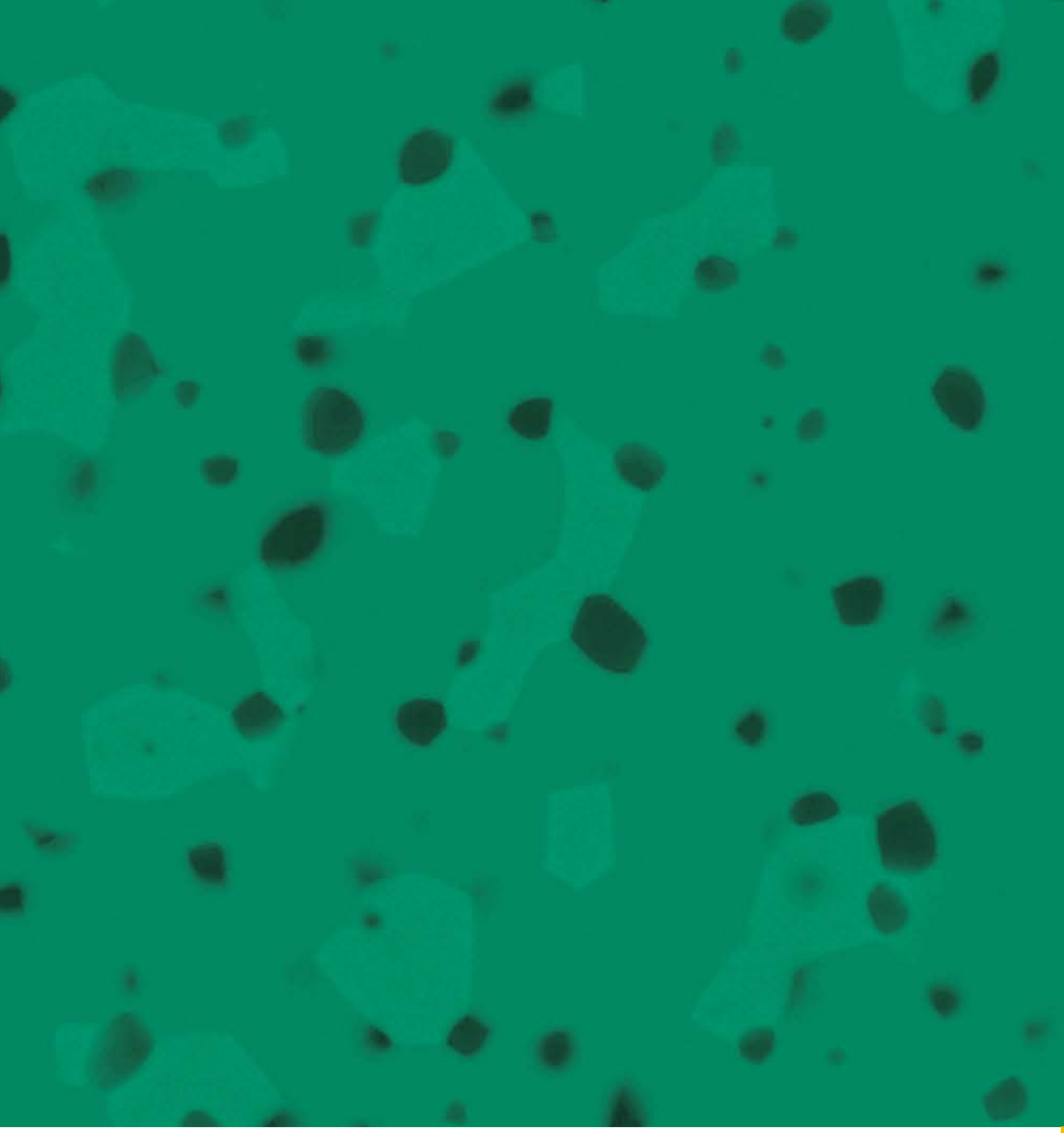

Energie & Umwelt / Energy & Environment
Band / Volume 68
ISBN 978-3-89336-633-0

JÜLICH
FORSCHUNGSZENTRUM